공학박사학위논문

저온 박막 고체산화물 연료전지를 위한 멀티스케일 구조 금속 지지체 제작

Multiscale Structured Metal Support for Low-Temperature Thin Film Solid Oxide Fuel Cells

2023 년 2 월

서울대학교 대학원

기계공학부

정 원 엽

저온 박막 고체산화물 연료전지를 위한 멀티스케일 구조 금속 지지체 제작

Multiscale Structured Metal Support for Low-Temperature Thin Film Solid Oxide Fuel Cells

지도교수 차 석 원

이 논문을 박사 학위논문으로 제출함
2022년 10월

서울대학교 대학원
기계공학부
정 원 엽

정원엽의 공학박사 학위논문을 인준함
2022년 12월

위 원 장 _____ 안 성 훈 _____ (인)

부위원장 _____ 차 석 원 _____ (인)

위 원 _____ 이 윤 석 _____ (인)

위 원 _____ 박 태 현 _____ (인)

위 원 _____ 조 구 영 _____ (인)

Abstract

Multiscale Structured Metal Support for Low-Temperature Thin Film Solid Oxide Fuel Cells

Despite decades of global efforts to combat global warming, the global average temperature continues to rise. In order to limit the continuously increasing carbon dioxide emissions, it is essential to develop alternative clean energy, and fuel cell technology is drawing attention as a candidate. Among various fuel cells with their unique characteristics, solid oxide fuel cells (SOFC) are in the spotlight as the most attractive candidate to replace fossil fuels due to their high efficiency and utility. SOFC is not only highly efficient but also has the characteristics of being able to use various fuels and catalysts. However, due to the high working temperature, the system is easily degraded, and there is a limitation in material selection. Due to these problems, there have been many obstacles in the commercialization of SOFCs. Therefore, to increase the technological level of SOFCs, developing a fuel cell with superior electrochemical performance is necessary even in a low-temperature (< 500 °C) region. Both ohmic loss and polarization resistance increase at low-temperature operating conditions compared to operating at high temperatures. Reducing these losses is the only way to achieve the required performance at low temperatures. There is a technique for lowering the ohmic loss that involves thinning an electrolyte in order to decrease the ion conduction length. Unlike the high-temperature sintering process, which is manufactured to a thickness of 10 micrometers, thin-film electrodes and electrolytes can be manufactured through PVD and CVD, which significantly reduces ohmic resistance. However, to apply the thin film process, the porous substrate must have appropriate pores of several

microns, and the surface must also be uniform. Due to these limitations, the thin film process could not be applied to metal support advantageous for commercialization. Therefore, this research developed a low-temperature manufacturing process to control the pore structure of the porous supporting metal to apply a thin film process and minimize the oxidation of the base material of support during the SOFC production processes.

An easy and simple process was used to control the surface of the metal support. A vacuum filtration process was used to reduce the pores of the metal support. Nickel powders of different sizes were sequentially filled into the pores of the metal support, and finally, surface pores and roughness were reduced by using ceramic GDC powder. After the vacuum filtration process, a rigid nickel network was formed without deterioration of the metal support by sintering in a hydrogen environment at 700 ℃. Through this, a surface with pores of several tens of nanometers was produced, and it was verified that the thin film process could be applied. For durability verification, it was confirmed that the surface structure did not change even after 12 hours of operation at 500 ℃.

The size of the pores of the developed metal support is small enough, but the pores are randomly distributed, so it is important to secure OCV through dense electrolyte preparation. In the case of manufacturing an electrolyte through a sputtering process, pinholes generated from the characteristics of the process may act as defects in the electrolyte. Therefore, a method capable of reducing such defects and increasing the ionic conductivity of the electrolyte has been developed. The grain size and grain boundary density of the electrolyte was controlled by adjusting temperature conditions during the sputtering, and characteristic changes were observed. Since the grain boundary has ion conductivity 1 to 2 times lower than that of the grain core, the grain size may be increased through high-temperature

deposition to reduce the density of the grain boundary. A high-temperature deposition process was applied to the manufacture of YSZ and GDC electrolytes to reduce losses incurred during ion conduction in the electrolyte. Finally, YSZ/GDC bilayer electrolyte was applied to metal support to ensure the electrochemical performance of 699 mW/cm^2 at 500 °C.

In order to analyze additional elements of the developed metal-supported TF-SOFC, various composition ratios of the anode were fabricated and investigated. For the consistency of the process, all elements were manufactured by the sputtering process, and in the case of the anode, NiO-GDC electrodes were manufactured through reactive co-sputtering. Electrodes of various volume ratios were manufactured by controlling the applied power, and their performance was compared. Finally, the anode with a volume ratio of about 1:1 showed the highest electrochemical performance, and a thermal cycle experiment was conducted to verify the thermal durability of the developed TF-SOFC. As a result, it was confirmed that the performance was maintained even after 5 thermal cycles.

Keyword : Multiscale structured metal support, Thin-film solid oxide fuel cells (TF-SOFCs), Surface control method, Sputtering, Electrolyte morphology, Optimum anode configuration

Student Number : 2017-25576

Table of Contents

List of Figures

List of Tables

Chapter 1. Introduction

1.1. Motivation

Despite global efforts to slow global warming, global CO_2 emissions are still rising. As a result, the global average temperature rose without interruption (33.3 metric gigatons of global energy-related CO_2 emissions in 2019) [1]. The temperature rise is causing abnormal climates, and the damage caused by climate change is also increasing. In response to this climate crisis, many countries are implementing stricter carbon emission regulations, spurring the development of renewable energy that could replace existing fossil fuels. Wind power, solar cell, and fuel cells were widely known as renewable energy sources. Among them, fuel cells, unlike other alternative energy sources, are less affected by the operating environment, so they can continuously produce energy. In addition, fuel cells have superior gravimetric energy density among various electronic devices, as described in Figure 1. Therefore, fuel cells with high utility as an energy device that can replace fossil fuel is in the spotlight.

The fuel cell has high efficiency because it generates electrical energy directly from chemical energy without mechanically moving parts. The electrochemical reaction that produces electricity occurs in spatially separated anodes and cathodes based on the electrolyte. A hydrogen oxidation reaction (HOR) takes place at an anode, an oxygen reduction reaction (ORR) takes place at a cathode, and electrons move due to the potential difference between the two electrodes [2]. Ions are conducted through an electrolyte, electrons move through an external conducting wire, and the flow of these electrons may be used for an external device.

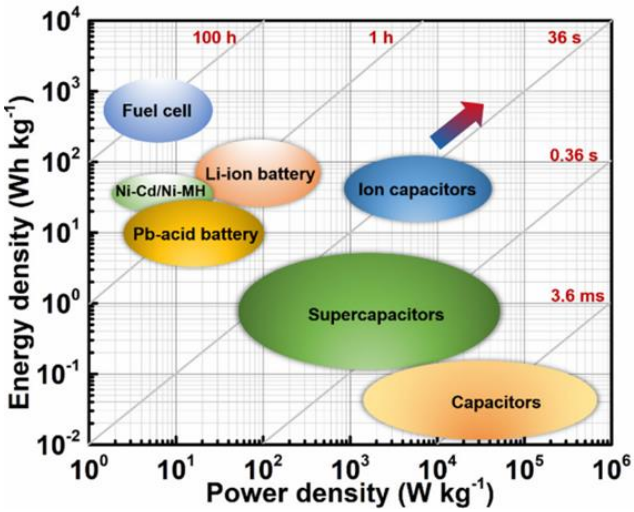

Figure 1. Ragone plot for energy density comparison of various electronic devices [3]

Various types of fuel cells are classified according to the electrolyte, and the operating temperature is determined according to the characteristics of the electrolyte. Representatively, there are alkaline fuel cells (AFCs), Phosphoric acid fuel cells (PAFCs), polymer electrolyte membrane fuel cells (PEMFCs), molten carbonate fuel cells (MCFCs), and solid oxide fuel cells (SOFCs), and their characteristics are summarized in Table 1. In the case of a fuel cell operating in a low-temperature area (60-220 °C), Pt, a precious metal, is mainly used as a catalyst, which causes a high cost for the stack. On the other hand, in the case of fuel cells operating at a high temperature (> 600 °C), Ni and perovskite materials could be used as catalysts so that they would have price competitiveness. In addition, fuel cells operating at a high temperature have the characteristic of fuel flexibility in that they can work with fuels other than hydrogen. In particular, SOFC, which has a high operating temperature, has the highest efficiency among fuel cell types.

	PEMFC	PAFC	AFC	MCFC	SOFC
Electrolyte	Polymer membrane	Liquid H3PO4 (immobilized)	Liquid KOH (immobilized)	Molten carbonate	Ceramic
Charge Carrier	H^+	H^+	OH^-	CO_3^{2-}	O^{2-}
Operating Temperature	80 ℃	200 ℃	60-220 ℃	650 ℃	600-1000 ℃
Catalyst	Pt	Pt	Pt	Ni	Perovskite (Ceramic)
Cell Components	Carbon based	Carbon based	Carbon based	Stainless based	Ceramic based
Fuel Compatibility	H_2, methanol	H_2	H_2	H_2, CH_4	H_2, CH_4, CO

Table 1. Characteristics classification of various fuel cells [2]

A typical H_2-O_2 operating SOFC structure is illustrated in Figure 2. In SOFCs, the supplied H_2 and O_2 react at the anode and cathode, respectively. And, the reactions that occur in the electrodes are as follows.

$$\text{Anode}: H_2 + O^{2-} \rightarrow H_2O + 2e^-$$

$$\text{Cathode}: \frac{1}{2}O_2 + 2e^- \rightarrow O^{2-}$$

SOFCs using a solid-state ceramic electrolyte have ion conductivity in a high-temperature environment. Examples of widely used electrolytes include a ZrO_2-based electrolyte and a Ceria-based electrolyte. A typical ZrO_2-based electrolyte is yttria-stabilized zirconia (YSZ). YSZ has excellent oxygen ion conductivity and chemically stable characteristics at high temperatures [4,5]. In addition, manufacturing costs are low compared to other electrolyte materials. Because of these advantages, it is still used as an electrolyte in commercially available SOFCs [6,7]. For the CeO_2-based electrolyte, the ionic conductivity is 1-2 orders higher than

that of the YSZ. Therefore, when GDC is applied to a low-temperature SOFC, the loss due to a decrease in conductivity can be reduced. However, in the case of the Ceria-based electrolyte, Ce^{4+} is reduced to Ce^{3+} to have electrical conductivity when exposed to a reducing environment. The anode should be a stable material even in a high-temperature reduction environment, and a mixture of Ni and ceramic is mainly used. Using a nickel catalyst and a ceramic electrolyte together makes it possible to increase the reaction area of an anode. Cathode must be resistant to high-temperature oxidation environments, and perovskite materials are used. Lanthanum-strontium cobaltite (LSC), strontium-doped lanthanum manganite (LSM), and lanthanum-strontium cobaltite ferrite (LSCF) are example of perovskite materials.

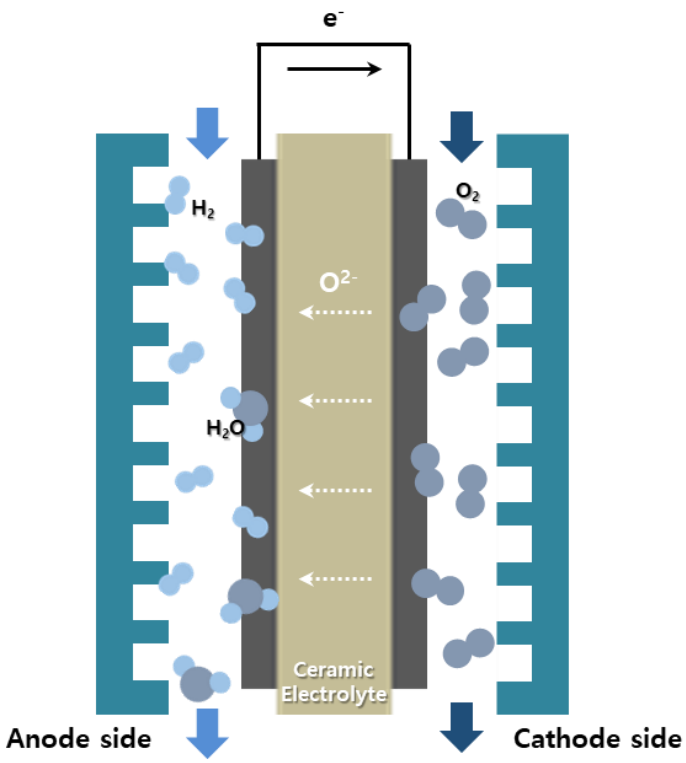

Figure 2. Schematic of typical H_2-O_2 solid oxide fuel cell

As mentioned earlier, various substances applicable to SOFC have been reported, but the commercialization of SOFCs is still facing considerable challenges. The high operating temperature of SOFCs brings many benefits but also causes fatal drawbacks. The high operating temperature quickly degrades the fuel cell stack structure, resulting in limited usable materials. Materials suitable for high-temperature environments increase the price of cells and become an obstacle to commercialization [8]. Therefore, in order to commercialize SOFCs, research to lower operating temperature and manufacturing cost should be preceded. Metal support-based thin film solid oxide fuel cells (TF-SOFCs) are promising candidates for improving the aforementioned problems. By applying the thin film electrolyte to porous metal substrate which can be manufactured inexpensively, a SOFC capable of operating at a low temperature can be manufactured. However, porous metal supports are vulnerable to high temperatures (> 1000 ℃) and oxidation environments required for the manufacture of electrodes and electrolytes deposited on the supports [9]. In addition, it is challenging to manufacture metal support having pores of a size capable of depositing a thin film. Therefore, low-temperature manufacturing procedures of the functional layer (electrodes and electrolytes) and a pore modification are crucial for the metal support-based thin film SOFC.

1.2. Thin Film - Solid Oxide Fuel Cells (TF-SOFCs)

The ionic conductivity of the ceramic electrolyte and the activity of the catalyst

diminish as the SOFC's operating temperature is decreased. As a result, the electrode's electrochemical reaction rate slows down, and ohmic loss from ion conductivity rises. Therefore, it is required to compensate for the loss brought on by the low temperature in other areas in order to lower the operating temperature while preserving the performance of the SOFC. There are two main ways to mitigate ohmic loss in terms of lowered ionic conductivity. The ohmic loss is expressed as follows.

$$\eta_{ohmic} = \mathrm{j}\frac{L}{\sigma}$$

The first is the use of an electrolyte that has a high ion conductivity. The most common electrolytes used nowadays are CeO_2-based electrolytes with good ion conductivity at low temperatures. Second, there is a technique for thinning the electrolyte. Since ohmic loss is related to electrolyte thickness, ohmic loss can be significantly decreased by thinning the electrolyte to less than a micrometer. However, a thin film electrolyte is produced using PVD and CVD procedures since it is difficult to fabricate a nano-thick electrolyte using the conventional manufacturing process.

.

1.2.1. Thin Film Deposition Process

The physical vapor deposition (PVD) and the chemical vapor deposition (CVD) are representative processes for manufacturing thin films. Physical vapor deposition methods include sputtering, thermal evaporation, and pulsed laser deposition (PLD). The PVD process typically results in individual atoms or small atomic clusters being separated from solid or liquid sources and diffused within the vacuum chamber and

attached to the surface of specimen to form a thin film. The sputtering and PLD processes are briefly described in Figure 3. An inert gas (typically argon) is ionized in a vacuum chamber to perform sputtering. The sputter gun (target) acts as a cathode, and when a power is applied to the gun, Ar loses electrons due to the collision between electrons and argon and becomes Ar^+, a cation. At this time, Ar^+ collides with the target due to the attraction with the cathode due to the electric field. The atom is ejected from the solid target if the cation has sufficient kinetic energy to break the target's atomic bond. The separated atom is called a sputtering atom, and the process of forming a film by adhesion to another surface is called sputtering deposition. The sputtering process has the advantage of being easily applied to most materials that can be made into solid targets such as metals, ceramics, and composites. In addition, it is easy to control deposition variables such as chamber pressure, applied power, and deposition temperature, so a film having required characteristics can be manufactured through sputtering. Pulsed laser deposition is a photon-induced deposition process that generally uses ultraviolet excimer lasers such as KrF lasers. The majority of light pulses are absorbed by the target's surface, which causes the target material to vaporize and be ablated. Since the material is ablated while preserving the composition ratio of the target, it is effective in manufacturing a film having a composite composition including many elements. However, in the case of the PLD process, large-area deposition is difficult due to laser source constraints, so it is used in the early stages of material development and application.

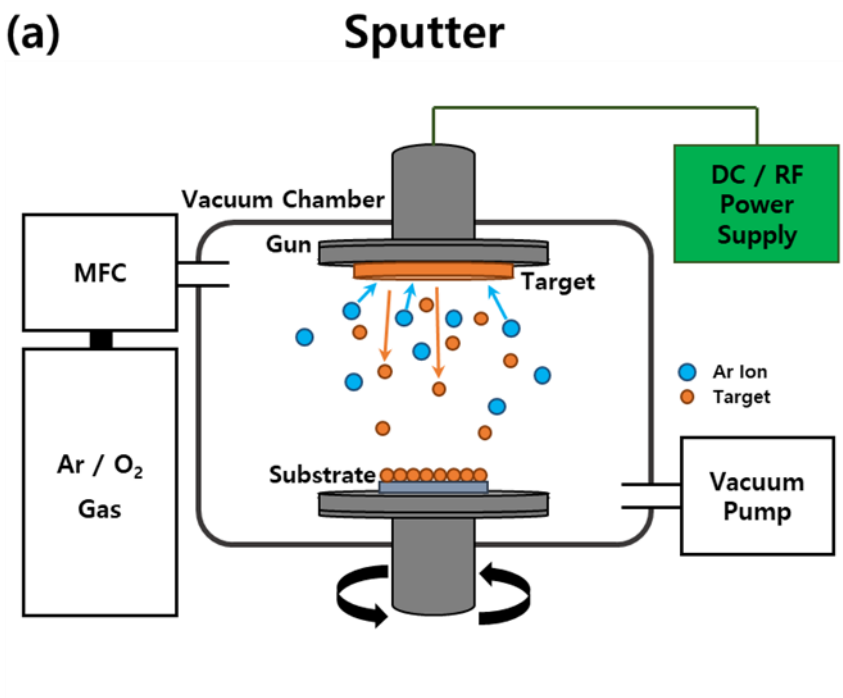

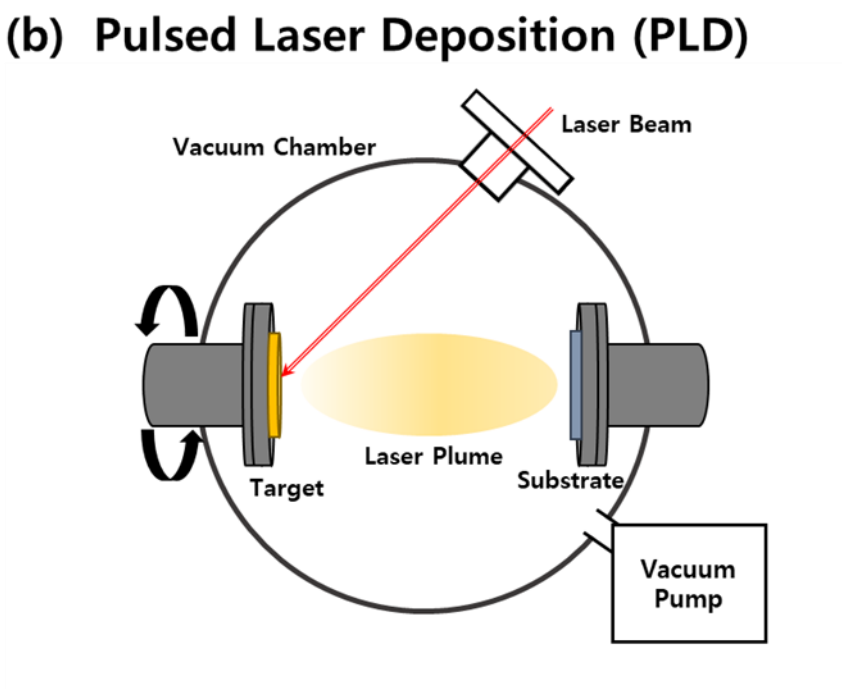

Figure 3. Schematics of (a) sputter and (b) pulsed laser deposition

There is an atomic layer deposition (ALD) technique that is categorized under CVD that can be used to fabricate nano-thick films. ALD is generally constructed based on a unit cycle of four stages, each of which is depicted in Figure 4. Precursor pulsing is a process of supplying a precursor of the material to be deposited. The precursor is supplied either directly by vapor pressure or with an inert carrier gas (e.g. Ar). Purge is a process of removing the precursor remaining undeposited on the substrate by using an inert gas. The reactant pulsing process supplies a gas necessary for the reaction, such as oxygen, to remove the ligand of the precursor through a chemical reaction. Depending on the method of supplying energy necessary for a chemical reaction, there are thermal ALD and plasma-enhanced ALD (PEALD). By-products of a chemical reaction are removed during the final purge step, and contaminants are eliminated by the flow of an inert gas. An angstrom-scale film may be manufactured through four cycle steps, and a thin film of a desired thickness may be manufactured by repeating the cycle. ALD can produce high-quality thin films and has excellent step coverage even on surfaces with complex structures. However, since the thickness deposited per cycle is very thin (angstrom or nano scale), deposition time and cost are high.

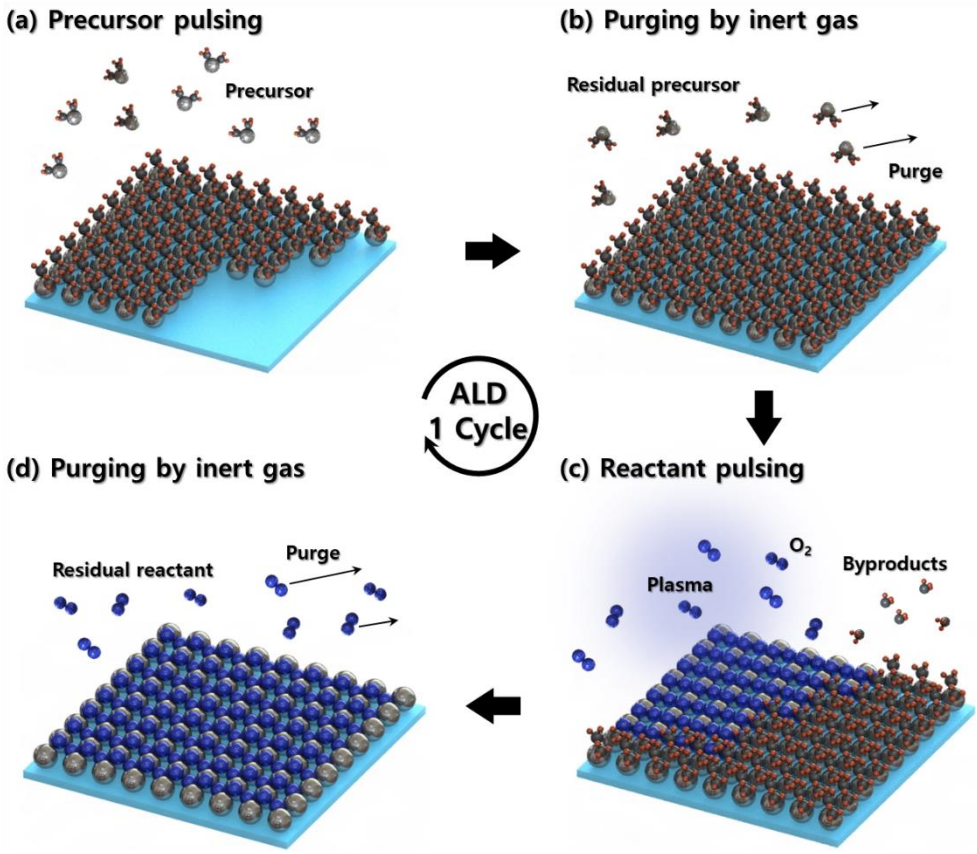

Figure 4. Schematic procedure of plasma enhanced atomic layer deposition (PEALD) unit cycle

1.2.2. Thin Film Solid Oxide Fuel Cells: Types

Because the ion conduction path is short, applying a 1 micrometer level thin film can reduce ohmic loss. However, due to the ultrathin thickness, the mechanical strength is not sufficient, and if there are some internal defects, it may cause structural destruction or fuel penetration. Therefore, high density and defect-freeness are essential in the case of thin film electrolytes. In order to deposit an electrode and

a dense thin film electrolyte through the PVD process, it is essential that the deposited surface has an appropriate pore size and roughness. Figure 5 shows the configurations of the representative TF-SOFCs. The nano-sized holes on the AAO substrate, as depicted in Fig. 5(b), are highly aligned, making it appropriate for thin film deposition. Therefore, many studies on AAO-based TF-SOFC have been reported [10–21]. An outstanding study of TF-SOFCs using a nanoporous AAO substrate was reported in Cha's research group. A thin film electrode and an electrolyte were deposited using both PVD and CVD processes, and the total cell thickness was less than 1 μm. A several nanometer thick YSZ electrolyte was applied to a Pt cathode using an ALD process with good step coverage, thereby preventing Pt agglomeration at a high temperature and increasing ORR activity by 2.5 times. This study is the first reported study on a method of improving durability and catalytic activity by coating electrodes [12]. In addition, research has been reported to improve the current collecting resistance of the electrode made of sputtering. The columnar structure of the electrode was modified by adjusting the sputtering conditions such as a target-substrate angle and the substrate rotational rate and based on this, the performance was improved by about 50%, thereby obtaining an electrochemical performance of 477 mW/cm^2 at 500 °C [13]. Other research groups are also actively studying AAO-based TF-SFOCs. Lee et al. reported producing TF-SOFC only by the sputtering method. On AAO, every component (anode, electrolyte, and cathode) was sputtered in turn and tested at 600 °C and 650 °C. A fuel cell manufactured using low-cost and scalable processes exhibited excellent electrochemical performance of 1.7 W/cm2 at 600 °C [17].

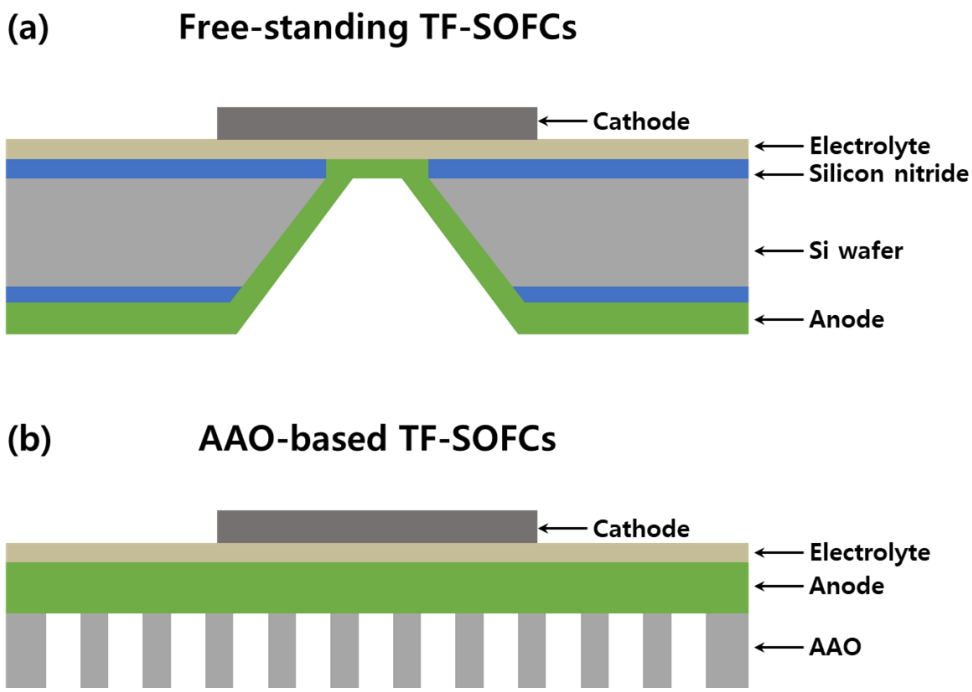

Figure 5. Schematics of (a) Free-standing and (b) AAO-based TF-SOFCs

As illustrated in Fig. 5(a), free-standing refers to SOFC without a structure that supports electrodes and electrolytes in the reaction region. Such regular nanostructures can be manufactured by applying wet etching, reactive ion etching, and photolithography processes. Through the etching process, only a micro-area electrolyte is exposed, and then electrodes are deposited under and above the electrolyte. TF-SOFCs can be manufactured with nano-thick electrolytes, enabling performance verification at low temperatures [22–35]. Free-standing type TF-SOFC has been actively studied by professor Prinz's research group. A free-standing nanostructure that can increase the reaction area was developed. A YSZ electrolyte with 70 nm thickness was deposited on a patterned Si wafer and tested at 450 °C or lower. The peak power density of the corrugated free-standing SOFC was 861 mW/cm^2, which was the greatest value at the time documented in the literature [25].

Thereafter, a study was reported on increasing the reaction area by applying a pyramid-shaped nanostructure and increasing the catalytic activity by applying the YDC cathodic interlayer. And at 450 °C, these 3D nanostructured SOFCs showed excellent electrochemical performance of 1.3 W/cm^2 [30]. The free-standing SOFC, which shows high performance even at low temperatures, has limitations in terms of thermodynamic stability due to the ultra-thin thickness [36–38] and thus faces difficulties in large-area fabrication and commercialization.

1.3. Metal-supported Solid Oxide Fuel Cells (MS-SOFCs)

A supporting layer that provides mechanical rigidity is required for the anode, the electrolyte, and the cathode. As shown in Figure 6, each functional layer (anode, electrolyte, and cathode) can be made to have an appropriate thickness to act as a support layer and is categorized based on the type of supporting layer. An electrode and a cathode are supported by a thick electrolyte in the electrolyte-support type. If an electrolyte is produced through a high-temperature manufacturing process, a defect-free electrolyte can be produced. By employing a variety of deposition techniques, an anode and a cathode can be easily coated on either side of the prepared electrolyte to create electrolyte-supported SOFCs. However, it is necessary to operate at high temperatures when a thick electrolyte is used to ensure the required ionic conductivity. Therefore, it works at a high temperature of 850 - 1000 °C and faces disadvantages caused by high temperatures. The electrolyte can be manufactured to be thin for the cathode-supported type, but the oxygen mass transport resistance increases due to the cathode layer with a thick structure, resulting

in mass transport loss. Therefore, even in the cathode-supported SOFCs, it is challenging to drastically lower the operating temperature [2,39]. The anode-supported and the metal-supported types have a similar structure in which the substrate supports three functional layers, and by thinning the electrolyte, the operating temperature of the SOFC can be effectively decreased. For this reason, it is the most widely studied structure of SOFC academically and industrially.

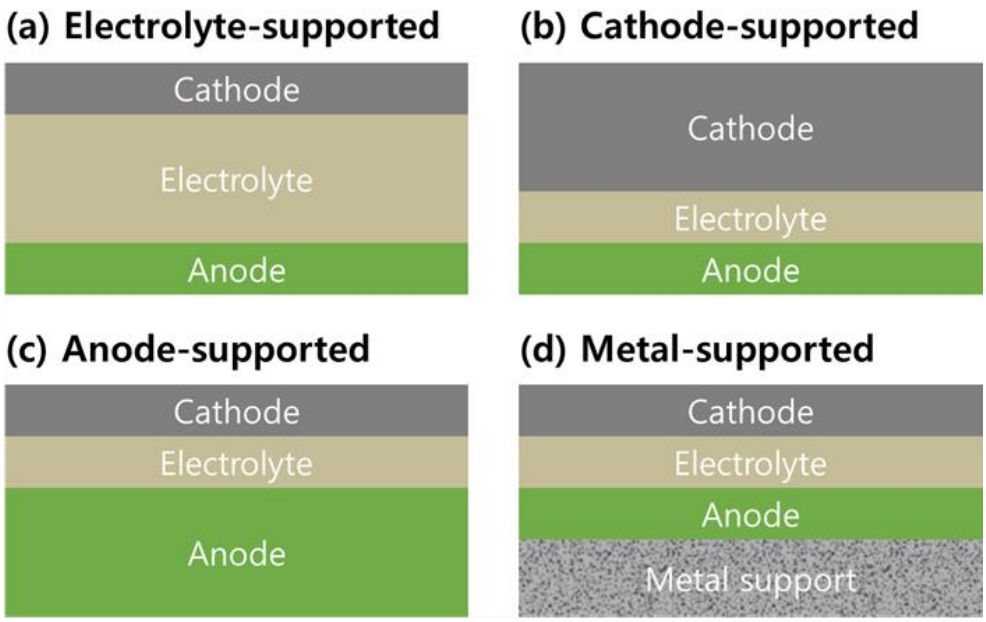

Figure 6. Simple configuration of SOFCs according to the type of support

In addition to the high degradation rate and material selection constraints caused by the high operating temperature of the SOFC, electrolyte-supported, cathode-supported, and anode-supported types of SOFCs consist of brittle ceramics or cermet containing expensive materials (usually doped with rare earth elements) [39,40]. In contrast, the metal support SOFC uses only the functional layers as much as the thickness required for the electrochemical reaction. Functional layers are

sequentially deposited on the mechanical support in Figure 4(d), which is made of cost-efficient, highly permeable metal. Despite the advantages of low manufacturing cost and high productivity, the manufacturing procedure for metal-supported SOFCs requires consideration of many variables and consists of complex steps. The difficulty in the manufacturing process is caused by the sintering temperature difference between the functional layer made of ceramic and the metal substrate. YSZ, which is mainly used as an electrolyte, is manufactured at 1200 °C or higher for densification. Therefore, the metal substrate is easily oxidized and loses mechanical rigidity when exposed to the manufacturing temperature of the anode and electrolyte deposited on it [39–42]. In addition, at high temperatures, counter-diffusion of Fe, Cr (from the metal substrate), and Ni (from the anode) causes deterioration of the performance of each component. Therefore, many solutions for alleviating these problems have been reported. In order to prevent the oxidation of the base materials of substrate in the high-temperature sintering process, studies for sintering a green sheet consisting of a metal, an anode, and an electrolyte in a hydrogen or nitrogen environment have been reported [43–47]. Y. Zhou et al. reported metal-supported SOFC using stainless steel 430L substrate. A porous stainless substrate, Ni-based cermet anode, and YSZ were laminated and sintered together. The oxidation of the base materials of substrate was suppressed by sintering in a reducing environment at 1300 °C. The cathode fabricated by the impregnating method was also heat treated in a reducing environment at 850 °C. The fabricated MS-SOFC showed a power density of 438 mW/cm^2 at 800 °C [47]. Choi's research group has actively researched on MS-SOFCs and reported many results. [48–54]. A novel 3 phase anode was developed and tested on MS SOFC. $La_{0.2}Sr_{0.8}Ti_{0.9}Ni_{0.1}O_{3-d}$-YSZ-Ni composite anode, YSZ, and metal support were co-fired at 1250 °C in reducing environment. The cell showed excellent and stable electrochemical performance. The peak power density was 325 mW/cm^2 at 650 °C and the measured

OCV was stable even after 100 times of thermal cycle [48].

In addition to sintering in a reducing environment at high temperature, numerous investigations have been reported to lower the sintering temperature. R. Hui et al. reported the plasma spray method for anode and electrolyte deposition at 700 °C. Without post sintering process, the button cell showed a high performance of 0.92 W/cm^2 at 700 °C [55]. A case of electrolyte deposition using a physical vapor deposition method was also reported. S. Hui et al. fabricated MS-SOFC using stainless steel 430 substrates and tested at 400 – 600 °C. The anode was deposited by spin coating, and the electrolyte was deposited by PLD. After depositing the electrolyte, the post-sintering process was conducted at 850 °C [42].

The above-mentioned two research directions are to suppress oxidation of the supporting metal using a reduction environment and to slightly lower the manufacturing temperature. However, a temperature close to 1000 °C is still required to densify the electrolyte. It is also necessary to take into account the materials' thermal expansion coefficient in order to employ such a high temperature. One way to reduce the complexity of this manufacturing process is to apply a low-temperature thin film manufacturing process. However, few studies have been reported on fabricating and experimenting with MS-SOFC through a low-temperature manufacturing process. This is because it is difficult to manufacture metal support having a surface to which a thin film process can be applied. Therefore, developing a substrate that can be used in the thin film deposition method is expected to solve the difficulties of the existing manufacturing process significantly.

1.4 This Thesis

In order to apply the porous metal support and thin film process together to SOFCs, it is essential to secure a surface to which the thin film deposition process can be applied. Therefore, by using a facile and inexpensive method, pores of several tens of micro sizes were modified, and appropriate roughness and porosity were obtained. Since then, we have developed a sputtering process for the functional layers to manufacture high-performance TF SOFCs. Detailed research contents on the multiscale metal support fabrication process are in Chapter 2, the fabrication process of the electrolyte and anode of TF SOFCs are in Chapters 3 and 4, and the results are reviewed in Chapter 5. The details of each chapter are as follows.

- Chapter 2 describes the surface control process for multiscale surface structure of metal support. The developed methodology was prepared with minimal steps using Ni and GDC powders, a simple and inexpensive manufacturing method. Through the vacuum filtration process, two types of nickel powders were filled in pores and sintered in a reduced environment at 700 ℃ to obtain mechanical strength and conductive networks of the functional layer. To further lower the pore size, it was sintered after vacuum filtration of GDC powder of several tens of nanometers. The surface roughness, porosity, and surface morphology of the developed metal support were confirmed. A multiscale substrate was prepared, and then a porous NiO-GDC cermet anode and a YSZ electrolyte were sputtered. As a result, it was confirmed that the porous anode and the dense electrolyte were successfully deposited through surface analysis.

- Chapter 3 describes the thin film electrolyte sputtering process for MS SOFC. First, a YSZ electrolyte was prepared through a reactive sputtering method. Changes in grain size and crystallinity according to the deposition temperature of the electrolyte were confirmed. Due to its lower grain boundary density (low ionic conductivity), YSZ that was deposited at a high temperature of 500 °C demonstrated the best electrochemical performance. By applying the same concept, the GDC electrolyte was also deposited at 500 °C to confirm its characteristics. In order to utilize the GDC electrolyte having high conductivity at low temperatures, a SOFC was manufactured by applying a bilayer structure of YSZ/GDC, and its effects and performance were verified.

- Chapter 4 describes the development of a co-sputtering method for the manufacture of NiO-GDC nanocomposite anodes. An anode for SOFCs is typically composed of Ni and GDC (or YSZ). In order to manufacture the composite electrode, a co-sputtering process of metal and ceramic may be used, and in this case, a sputtering rate between the metal and ceramic target is very large, and thus it is difficult to match a ratio of metal and ceramic in the anode. In order to mitigate the sputtering rate difference and manufacture an anode with an appropriate ratio, Ni was deposited in an oxide form through reactive sputtering. The sputtering rate of the Ni target was reduced to make it easy to control the ratio of Ni and ceramic. Cermet anodes with various volume ratios were manufactured and characterized. The developed composite anodes were applied to the metal-supported SOFC to measure its electrochemical performance and confirm the optimal anode composition ratio. A thermal cycle experiment was conducted to verify the thermal durability of the developed metal-supported TF-

SOFCs. As a result, the electrochemical performance was maintained even after 5 cycles of severe thermal stress.

- Chapter 5 covered the data studied in the previous chapter and analyzed. On the basis of operating temperature, earlier research were arranged, and the outstanding result of this study was compared. Through this, the novelty and excellence of this study were explained.

Chapter 2. Novel and Facile Method for Surface Control of Porous Substrates

2.1. Introduction

Table 2 provides a classification and summary of the SOFC technology that has recently emerged in the market based on operating temperature and support type. It can be discovered that the developed electrolyte support type SOFC still requires a high temperature operating temperature of 800 ℃ or higher. An anode support type that could reduce the thickness of electrolytes was developed by various companies and designed to be able to operate in an intermediate temperature range. A typical example of a metal support type SOFC stack is a technology developed by Ceres Power. It works at 600 ℃ and produces a 5 kW output. Overall, the developed SOFC system operates above 600 ℃ and has rarely reported performance at temperatures below 500 ℃.

Company	Ceres Power	Bloom Energy	Kyocera	Mitsubishi Power	Elcogen	Sunfire
Country	UK	USA	Japan	Japan	Estonia	Germany
Type	Metal supported	Electrolyte supported	Anode supported	Anode supported	Anode supported	Electrolyte supported
Working Temperature (℃)	600	< 1000	750	900	650	850
System Size	5 kW	300 kW	0.8 kW	250 kW	1-3 kW	0.35-20 kW

Table 2. Technical data of recently developed SOFCs [56]

For SOFCs operating at high temperatures, each component's thermal expansion coefficient (TEC) must be similar. At high temperatures, the TEC mismatch can have a significant impact and lead to cell structural failure. Therefore, it is important to select a material with a TEC similar to the electrolyte in selecting metals. Representatively, the TEC and price of materials used in metal supports are summarized in Table 3. Many research results have been reported on the metal-supported SOFC developed by Ceres Power [57–61]. They used a ferritic stainless steel substrate with a TEC similar to the electrolyte. They used a laser drilling process on a metal substrate to create a channel through which fuel could penetrate. The hole size was 10-30 μm, and the anode and electrolyte were deposited on the laser-perforated area by the screen printing process. Ceres Power developed a manufacturing process that does not use a high sintering temperature for the deposited ceramic layer[58]. Through this technology, they successfully developed intermediate-temperature SOFCs.

Metal Substrate	TEC (ppm/K)	Cost ($ /kg 2009)
NiCrAlY	15 – 16	63
Hastelloy-X	15.5 – 16	22
Ni	16.5	18
Ni-Fe (1:1)	13.7	9
300-Series stainless steel	18 – 20	2
400-Series stainless steel	10 – 12	2

※ TEC of electrolytes are 10 – 12 ppm/K

Table 3. TEC and cost of various metal supports [39]

The majority of issues with the metal-supported SOFCs mentioned above arise during the post-treatment procedure, which comes after depositing a functional layer on the prepared metal support. The problem caused by the difference in sintering conditions may be partially solved by lowering the sintering temperature or sintering in a reducing environment. However, these methods might not solve the SOFC system's primary issue, which is its high operating temperature. In order to lower the high operating temperature, a thin film electrolyte should be applied, and the metal support has a surface structure in which the thin film electrolyte may not be deposited. When an electrolyte is deposited on a metal support with pores of several tens of microns and a rough surface through a PVD process, a dense structure may not be obtained. Therefore, developing metal support with an appropriate pore size and roughness is essential for producing metal-supported low-temperature SOFCs.

This chapter describes a novel and facile process for pore modification of the metal substrate. The process was developed by focusing on using cheap materials, the low-temperature manufacturing process, and simplifying the manufacturing process. In order to avoid degradation of the supporting metal, the manufacturing temperature was set to 700 ℃ or lower, and nickel and GDC powder, which are materials that are easy to access, were applied. As a result, metal support with the size and roughness of pores to which a thin film could be applied was successfully produced.

2.2. Experimental

A multiscale structured substrate was developed using a commercially available

porous stainless steel (SS) 316 L sheet (Mott Co., US) as the base material. The porous sheet was used after laser cutting at 1 x 1cm^2. Prior to the surface control procedure, the bare substrate was cleaned with acetone, ethanol, and DI water in that order for 10 minutes in a sonication bath. The surface control process was briefly described in Figure 77. The surface control of the porous substrate was performed by sequentially filling particles of different sizes. Two types of nickel (< 50 μm and < 1 μm size) and one type of GDC10 (< 500 nm size) (Sigma-Aldrich Co., US) particle were used, and particles were filled in pores using a homemade vacuum filtration device.

First, 200 mg of large Ni (< 50μm size) particles were dispersed in ethanol and filtered twice. To use only the proper size powder, the large particles were settled for 3 minutes after dispersion and only suspended particles were used. And the excess powder on the substrate was carefully removed. Second, 10mg of small Ni (< 1μm size) particles were well dispersed in ethanol for 10 minutes through a sonication bath and then filtered. In this step, the excessive powder was directly compressed at 10 MPa using a hydraulic press device without removing it. When pressing excess powder on the substrate, it was pressed using a plate surface-treated with 2000 grit sandpaper. As the roughness of the pressing surface in contact with the powder affects the surface roughness of the metal support, the pressing plate (R_q=127 nm) with the lowest roughness as possible was used. And compressed substrate was reduced at 700 °C for 3 h, and the heating rate was 5 °C/m. Third, 5 mg of GDC powder was dispersed and filtered in the same manner as small Ni powder. After filtering the GDC powder, the excess powder was carefully removed after heat treatment under the same conditions as the reduction of the nickel powder.

A field-emission scanning electron microscope (FE-SEM, Zeiss Supra 55VP, Carl Zeiss, Germany) was used to examine the surface morphology of the

manufactured substrate. Additionally, a cross-section polisher (IB-19520CCP, JEOL, Japan) was used to obtain the cross-section images. The 3D surface profile data and roughness were obtained by a 3D surface profiler (μSurf, NanoFocus, Germany). And, using a porosimeter (AutoPore IV 9500, Micromeritics, US) and free image J software, the porosity of the manufactured substrate was determined.

The fabrication of thin film anodes and electrolytes was carried out using a commercial magnetron sputtering device (Daeki Hi Tech Co., South Korea). The anode was deposited with nickel and GDC20 (Gd 20 mol % doped, RND Korea, South Korea) targets. The DC and RF sputter guns were equipped with nickel and GDC20 targets, respectively, and the applied power was set to 50 W. And during reactive co-sputtering, Ar and O_2 gases were supplied at 20 sccm, and 5 sccm, respectively, and the working pressure was fixed at 4.0 Pa (30 mTorr). Y-Zr (16:84 at %) alloy target was mounted on the DC gun, and reactive sputtering was performed to deposit the YSZ electrolyte on the NiO-GDC anode. For reactive sputtering, Ar and O_2 gases were supplied at 20 sccm and 5 sccm, respectively, while the working pressure was kept at 0.67 Pa (5 mTorr).

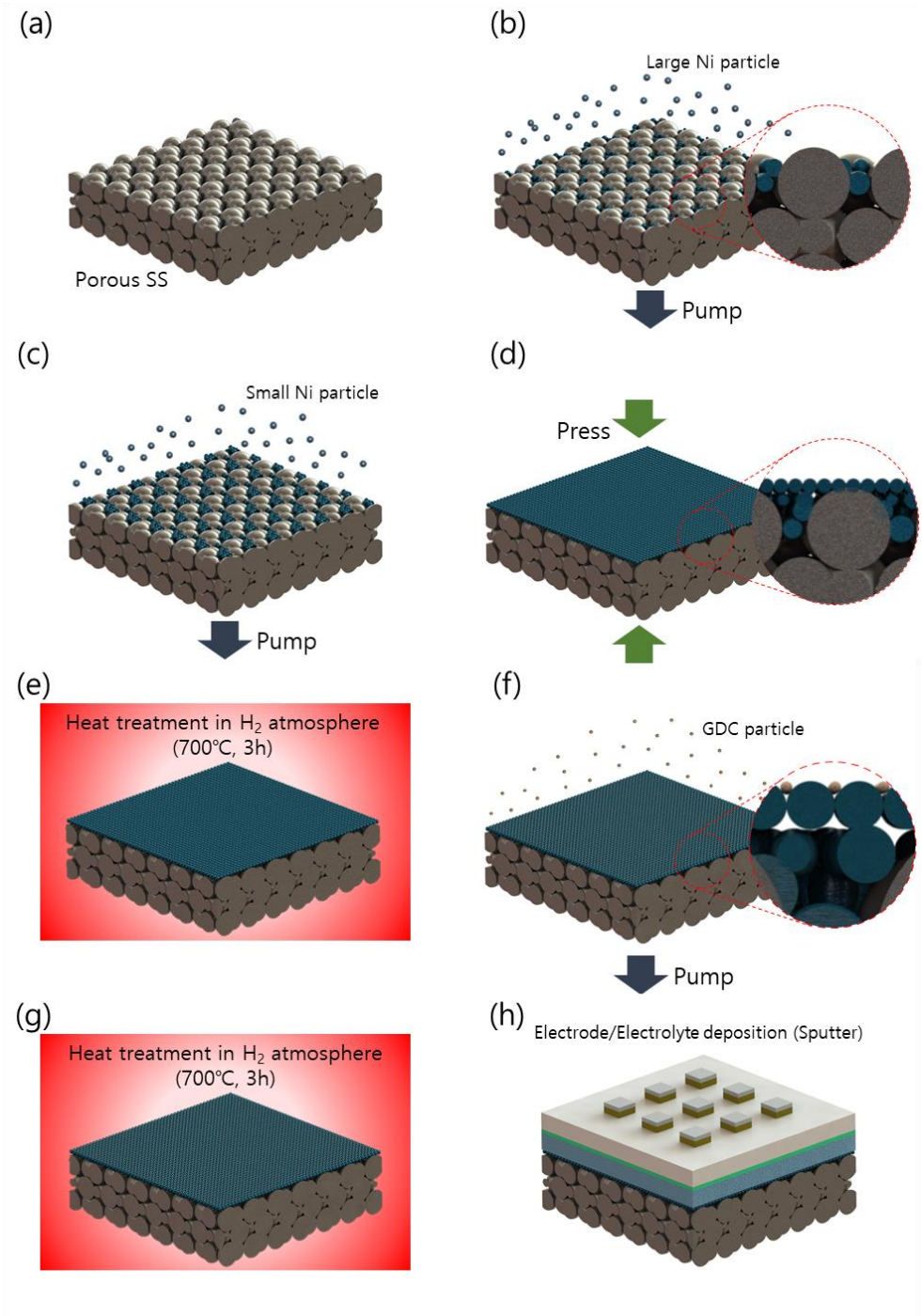

Figure 7. Schematic diagram of surface control process

2.3. Result & Discussion

2.3.1. Analysis of Surface Morphology Changes and Characteristics According to Surface Control Process

As shown in Figure 88(a), bare stainless steel substrate has irregular pores with a size of 20-30 μm. In a substrate with such large pores and a rough surface, a thin film may not be deposited using a physical vapor deposition process. According to Choi et al., in order to fabricate a dense electrolyte using the physical vapor deposition method, the electrolyte's thickness should be two to three times more than the substrate's pore size [53]. From this perspective, the substrate's pore size should be at least 500 nm for a dense electrolyte with a thickness of 1 μm.

As the first step of the pore control process, a vacuum filtration process is performed using a large-sized nickel powder. Nickel powder having a broad particle size distribution of less than 50 μm is used. In the filtration process, nickel particles with a tiny size pass through the substrate, and particles larger than the pore remain on the subtrate’s surface, and only particles with an appropriate size fill the gap between the pores. As a result, only particles with a size of 2-3 μm remain between the pores, as shown in Figure 1010(b). However, the surface pore structure of the substrate did not change even after the first step of the surface control process. From the roughness and 3D surface profile data of Figure 1111(a,b), it may be seen that the large-sized nickel powder filtration may not change the roughness of the substrate. In order to modify the surface morphology of the substrate, vacuum filtration using small-sized powder (small Ni and GDC) was carried out, and the results were analyzed by dividing it into the application of the compression process after vacuum filtration. First, when the compression process is not applied, it can be found that the pore size of the upper surface has decreased from a few tens of micrometers to a few

micrometers, as shown in Figure 88(c). And, the surface roughness was also reduced to 1.45 μm. Additional GDC10 powder vacuum filtration and reduction process reduced pores to nanoscale and roughness to less than 1 μm.

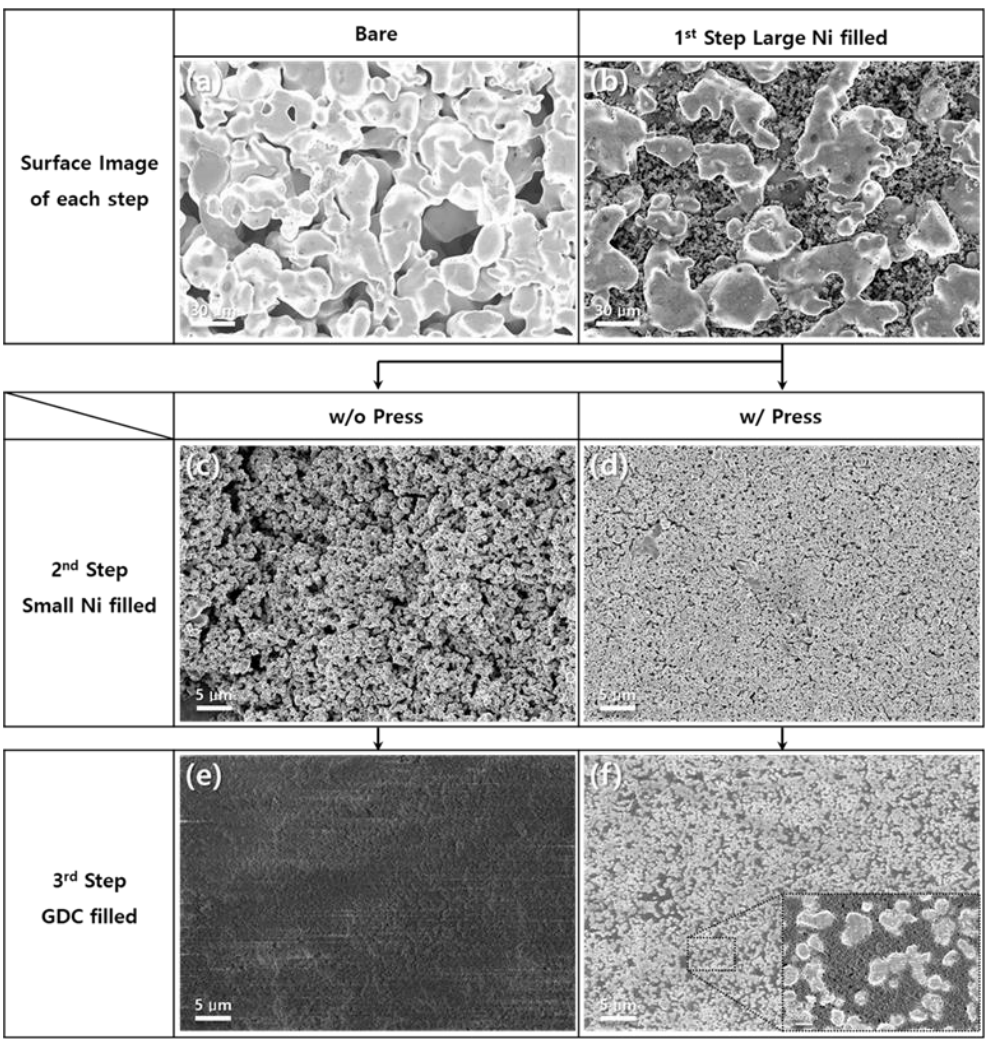

Figure 8. Surface images of the porous substrate at each step of the surface control process

Referring to Figure 88(d), when the compression process is applied, the surface

roughness and the pore size are significantly reduced compared to when the compression is not used. This is because the roughness is adjusted according to the surface profile of the plate in contact with the substrate in the process of compressing the excess nickel powder layer. The surface morphology of the substrate was not only affected by the surface roughness of the touching plate, but also by the pressure. Figure 9 shows a surface of substrate according to pressure, and in the case of 2 MPa to 8 MPa, the pressure is not sufficient, and thus nickel particles are not sufficiently packed. Therefore, many defects on the surface remained. At a pressure of 10 MPa or more, the surface defects were sufficiently reduced. Therefore, a pressure of 10 MPa was selected and used. Referring to Figure 1111(e), the effect of the compression process was confirmed, and the roughness of the surface was reduced to about 1/5. In addition, during the reduction sintering process, nickel powders form a neck by diffusion on surfaces that contact each other to lower surface energy, thereby forming a structural stiffness and electron conduction network. When the compression process is applied, the nickel particles are more densely filled and more particles are connected, thereby increasing structural stability and electronic conductivity after reduction sintering. This is demonstrated in Figure 1010(b), which depicts the formation of a nanoporous nickel layer on a micro-scale porous substrate with a thickness of about 10 μm. Referring to the roughness data in Figure 1111(f), the surface roughness increased when the nano-sized GDC powder was vacuum filtered. However, this result is presumed to have occurred at the limitations of 3D surface analysis. The GDC powder filled between the pores of the porous nickel layer was not sufficiently recognized, and thus the roughness was not affected, and the roughness was increased due to a measurement error.

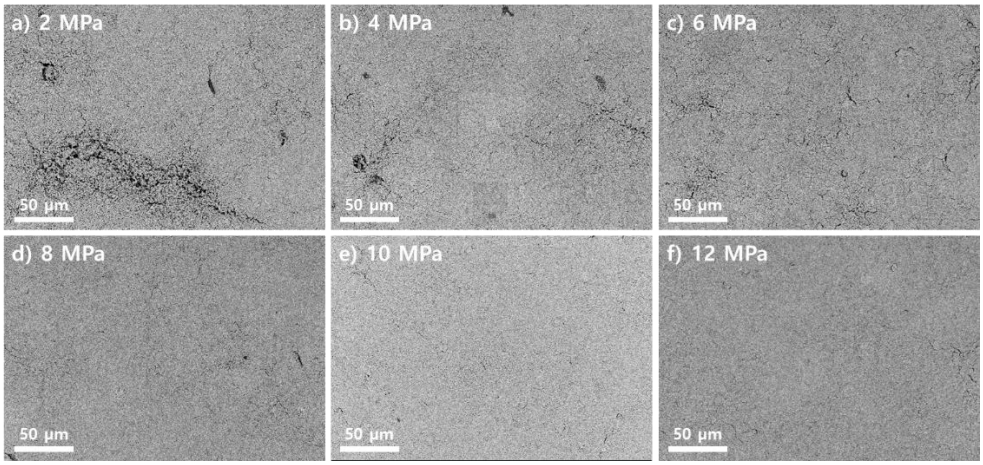

Figure 9. Surface images of pressed substrate according to pressure

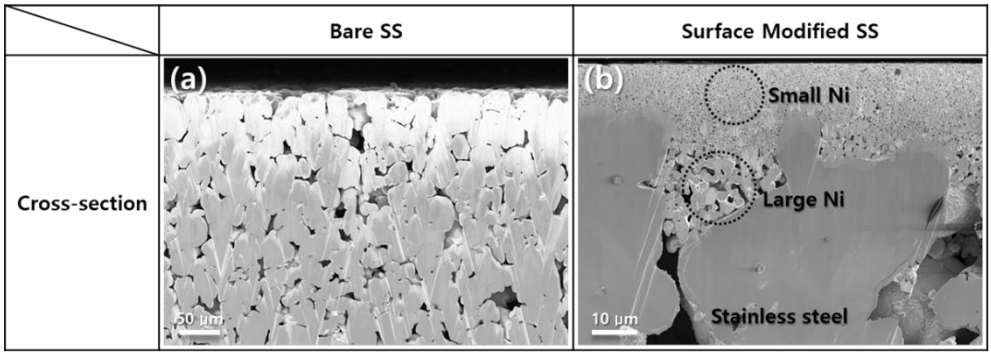

Figure 10. Cross-section images of the bare and pore-modified stainless steel substrate

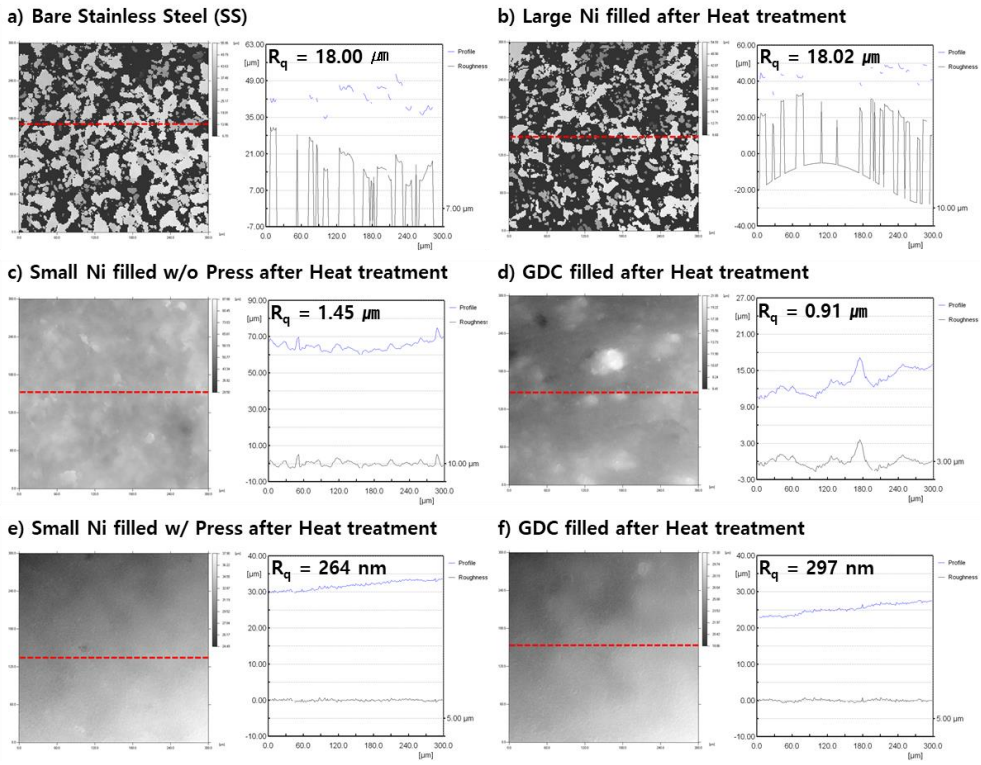

Figure 11. 3D surface profile images and surface roughness data.

As shown in Figure 88(f), when the nano-sized GDC powder is vacuum filtered, particles are sufficiently filled between the pores of the porous nickel layer, and thus it is difficult to identify pores in a low magnification image. Pores that are 50 nm in size, large enough for the hydrogen fuel to pass through, are depicted in the high-magnification inset image of Figure 88(f). In order to examine the substrate's porosity at each step, a method using mercury and an image contrast analysis method were used. The reliability of the porosity measurement method using mercury can be confirmed through bare substrate analysis. In this case, the results were nearly identical to the product's known specifications (approx. 36 %). The developed substrate is manufactured by modifying only one surface of the substrate, so it is expected that it would not have a dominating effect on the overall porosity of the

substrate. However, as a result of the measurement, it was confirmed that the average pore diameter and porosity could be effectively decreased even by the pore modification on one surface. In the case of vacuum filtration of GDC powder, a change could not be verified through the mercury measurement method because it affects a tiny part of the surface. Therefore, the porosity was measured through surface image analysis and confirmed that the porosity was reduced to 10.2 %.

	Bare	**1st step**	**2nd step**	**3rd step**
	Porosimeter			Image J
Average Pore Diameter (μm)	10.5	8.11	2.3	-
Porosity (%)	37.5	38.1	21.0	10.2

Table 4. The porosity measurement results of pore-modified substrates

The surface roughness and porosity of the substrate as well as the electrical conductivity are also important characteristics that the support should have. During the heat treatment process of the substrate, the electrical conductivity of the substrate must be preserved even if it is exposed twice to a reducing atmosphere of 700 °C. Table 5 summarizes the electrical conductivity of the bare substrate and the substrate after thermal treatment. It was found that there was no significant change in the electrical conductivity of the support even after two heat treatments during the pore control process. Therefore, the developed pore control process did not affect the properties of the support.

	Bare	Heat treated 1 time	Heat treated 2 times
Resistivity	0.046 mΩcm	0.050 mΩcm	0.049 mΩcm

Table 5. Electrical conductivity of bare and heat treated SS 316 L substrate

2.3.2. Durability of Multiscale Structured Metal Support and Applicability of Thin Film Process

Metal-supported solid oxide fuel cells are more resistant to mechanical stiffness and thermal shock than other types (anode support, electrolyte support, and cathode support) of solid oxide fuel cells. The structural change of the support in the operational environment was observed to confirm the thermal durability of the developed substrate. After fabricating the substrate, it was exposed for 12 h in a reducing environment of 500 ℃. Figure 1212 shows surface images of a support before and after exposure to an operating environment of a solid oxide fuel cell. The surface morphology of the nickel particles did not change even after 12 h of exposure at 500 ℃. Therefore, it seems that there will be no degradation of the multiscale support even in long-term operation.

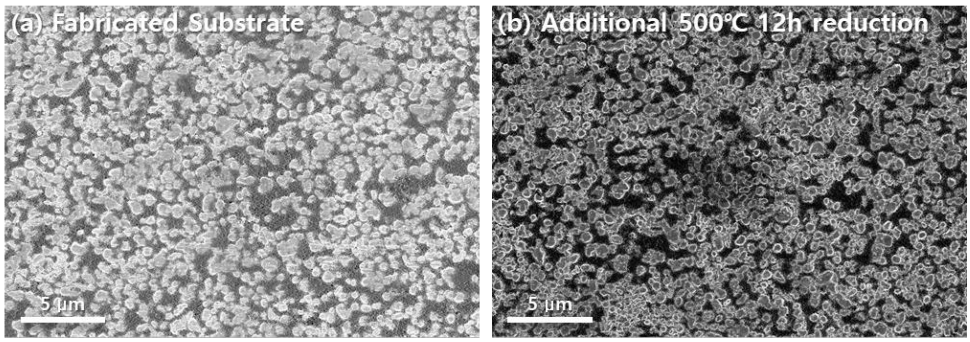

Figure 12. Surface images of the substrate before and after additional 12 hours of reduction at 500℃

Nickel oxide and GDC cermet anode and YSZ electrolyte were sputtered on substrates developed in the previous subchapter using the sputtering process to verify the applicability of the thin film process. The prepared substrate was divided into two types, whether a compression process using a hydraulic press was applied. As may be seen in Figure 1313(a), due to the surface structure of the very rough and irregular support, the sputtered atoms grew irregularly. As a result, the anode could not be deposited in a uniform surface required for dense electrolyte deposition. The surface of an electrolyte deposited on a rough anode is depicted in Figure 1313(b). And irregular particles are reduced, and surface roughness is significantly improved due to the YSZ electrolyte. However, it is evident that many pinholes are formed on the surface due to the insufficient density of the electrolyte. As shown in Figure 1313(c,d), it may be seen that the substrate subjected to the compression process has a very uniform surface of the sputtered electrode and electrolyte. This is because excess Ni particles are packed more densely on the surface during the compression process, and the roughness of the surface is constantly adjusted. Through surface image analysis, it was confirmed that a required film could be deposited on the developed substrate through the sputtering process. Also, a dense electrolyte without

pinholes could be manufactured with only 1 μm thickness deposition. This indicates that a thin film solid oxide fuel cell can utilize the developed substrate.

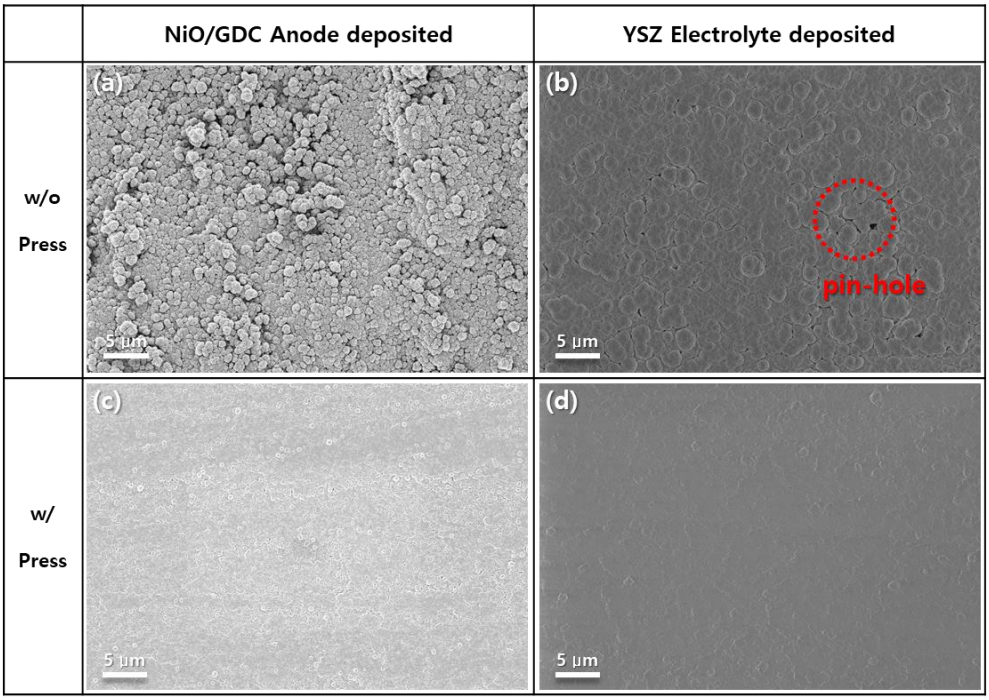

Figure 13. Surface images after anode and electrolyte deposition

2.4. Conclusion

In this study, the multiscale platform was developed through simple and inexpensive ways such as vacuum filtration, powder packing process, and heat treatment in a reducing environment. It was possible to effectively reduce the pore size of a substrate by filling two types of nickel powders into pores through a vacuum

filtration process. Also, the nickel particles filled in pores were intentionally agglomerated through sintering in a 700 ℃ reduction environment higher than the operating temperature, thereby obtaining structural rigidity and a conductive network. The size of the pore was additionally reduced, using GDC powder of several tens of nanometers for the application of the sputtering process. After manufacturing a multiscale substrate, porous NiO-GDC anode and YSZ electrolyte were deposited through a sputtering process. As a result, it was confirmed through surface morphology analysis that the porous anode and the dense electrolyte were successfully deposited.

Chapter 3. Effect of Deposition Temperature of Electrolyte on Performance

3.1. Introduction

In solid oxide fuel cells, various techniques are available for fabricating high-density electrolytes. Methods include spray pyrolysis, spin coating, inkjet printing, tape casting, screen printing, CVD, and PVD [4]. Except for the CVD and PVD methods, all other processes must undergo a sintering process after depositing an electrolyte on the substrate. At this time, the density of the electrolyte, the grain structure, etc., are determined according to the sintering temperature. Usually, high temperature (1200-1400 ℃) conditions are applied to sinter the YSZ electrolyte. Despite the benefit of large-scale fabrication, direct application to metal support is limited in the case of tape casting and screen printing procedures because of a high sintering temperature [62]. Also, in general, electrolytes with a level of 10 μm are deposited, which is unsuitable for application to low-temperature SOFC electrolytes. Therefore, a low-temperature PVD process capable of manufacturing a thin film electrolyte is receiving attention. Among them, the sputtering technique is the potential solution in terms of enabling large-area deposition and being used in various industries.

Through sputter deposition, various nanostructured films can be fabricated. The structure of the deposited film is affected by deposition temperature, chamber pressure, applied output power, and incident angle. Depending on the deposition conditions, a porous to dense film can be produced. Thornton's structure zone model is widely used as a model related to thin film growth and is depicted in Figure 14.

Although the developed model cannot precisely determine the microstructure of the thin film, it provides a basis for analysis. It is a great help in studying and predicting the thin film deposition process.

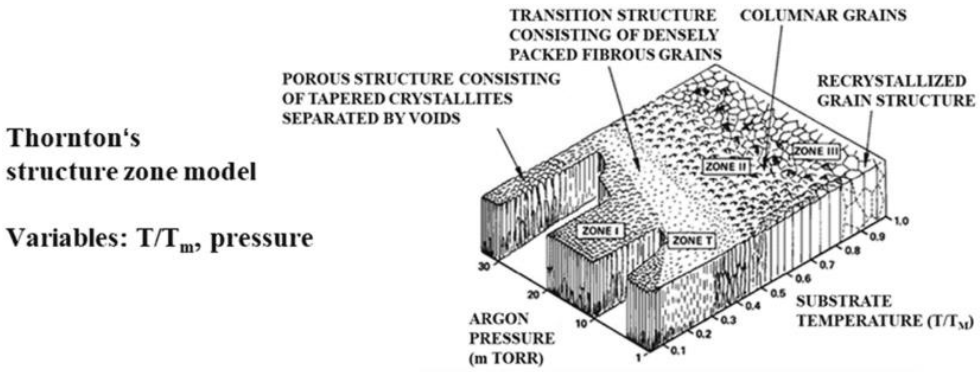

Figure 14. Schematic diagram of Thornton's structure zone model [4,63]

The model shown illustrates how the grain structure of the thin film is formed varies depending on the chamber pressure and substrate temperature. Therefore, it is possible to control the grains and grain boundaries affecting ionic conductivity by adjusting the temperature and pressure variables. As the substrate temperature rises, the energy of the atom increases, and the mobility gradually increases. Therefore, it is easier for atoms to move to the lowest energy location, increasing the thin film's grain size and making high-density growth possible. It is still debatable how grains and grain boundaries affect the ionic conductivity of electrolytes [64–76]. The results of analyzing the ionic conductivity of sintered electrolyte at the grain core and grain boundary were reported. Compared to the grain core conductivity, the conductivity at the grain boundary was about 1-2 orders of magnitude lower. Electrochemical reactions are influenced by grain boundary density in addition to ionic conductivity. Because the grain boundary functions as an active region, increasing the ORR is a

benefit of high grain boundary density [19,77]. Therefore, the grain structure affects the electrolyte's ionic conductivity and reaction kinetics, and it is crucial to design it well. The nanostructure of the deposited electrolyte is particularly significant in the case of the metal support developed in the previous chapter since it differs from the commonly used nanoporous AAO substrate in that it has relatively irregular pores and a rough surface.

In this chapter, we developed a sputtering-based method for producing an electrolyte, which is crucial for solid oxide fuel cells. The electrolyte was developed in preference to electrodes because fuel cells operate effectively only if a dense electrolyte could be deposited on the developed support. The YSZ electrolyte was deposited through reactive sputtering, and the crystallinity and grain structure of the electrolyte were analyzed according to the deposition temperature. The developed electrolyte was applied to the metal support and verified its performance. The GDC electrolyte was examined according to the sputtering temperature in order to apply low-temperature SOFC. Finally, a bilayer electrolyte was applied to the metal support to ensure excellent performance.

3.2. Experimental

A dense NiO-GDC anode was deposited on the developed 1 x 1 cm^2 multiscale substrate by a reactive co-sputtering process. RF and DC guns, respectively, were equipped with Ni and GDC20 targets. The chamber was evacuated at $1x10^{-4}$ Torr before reactive sputtering, and a deposition process was performed in a 4.0 Pa Ar/O2 environment. Ar and O_2 gases were supplied at 20 sccm, and 5 sccm, respectively,

and the power applied to Ni and GDC20 targets was 50 W. YSZ and GDC10 electrolyte was deposited at various deposition temperature (Room temperature, 300 °C, 500 °C). Y-Zr alloy (16:84 at %) and ceramic GDC10 (Gd 10 mol % doped, RND Korea, South Korea) targets were used for electrolyte. The base pressure of the chamber was under 1 x 10^{-4} Torr, and the working pressure was 0.67 Pa (5 mTorr). Reactive sputtering was performed under an Ar/O_2 (20/5 sccm) mixed environment, with DC and RF power being delivered to Y-Zr and GDC10, respectively. Lastly, 300 nm of porous LSCF ($La_{0.6}Sr_{0.4}Co_{0.2}Fe_{0.8}O_{3-\delta}$, Advanced Engineering Materials, China) -GdCe (Gd 20 mol %, Advanced Engineering Materials, China) cathode and 200 nm of Pt current collector were sequentially deposited on the electrolyte. The sputtering power applied to LSCF, GdCe, and Pt were 100 W, 60 W, and 100 W, respectively. In addition, the chamber pressure was kept at 4.0 Pa (30 mTorr) for the cathode and 8.0 Pa (60 mTorr) for the current collector at room temperature.

Focused ion beam (FIB, AURIGA, Carl Zeiss, Germany) and FE-SEM were used to investigate the cross-sectional images and surface morphology of those films that were deposited on Si and multiscale substrates. A high-resolution transmission electron microscope (HR-TEM, JEM-2100F JEOL, Japan) and X-ray diffraction (XRD, PANalytical X'pert Pro, Netherlands) were used to analyze the crystallinity and grain size of those films. As-deposited YSZ and GDC film on Si were prepared for XRD, and the tested cell was used for TEM. The doping ratio of sputtered electrolytes was analyzed by an X-ray photoelectron microscope (XPS, AXIS-HSi, KRATOS, United Kingdom).

To evaluate the electrochemical behavior, the metal-supported TF-SOFCs were mounted on a homemade stainless steel jig, and the metal support and the jig were connected using an Ag paste. Additionally, a ceramic sealant was used to physically divide the anode and cathode sides. After that, the experiment was conducted after a

half-day drying process. The experiment was conducted in a high-temperature furnace at 500 ℃, and 3% humidified hydrogen was supplied to the anode at 100 sccm, and the cathode was exposed to ambient air. The electrochemical behavior was confirmed using a commercial potentiostat (Gamry Reference 600, USA). For further analysis, electrochemical impedance spectroscopy (EIS) analysis was performed in the range of 1 MHz to 2 Hz, and the bias voltages of OCV and 0.6 V were applied.

3.3. Result & Discussion

3.3.1. YSZ Electrolyte: Surface Morphology and Film Crystallinity Analysis according to Various Sputtering Temperature

The density of the electrolyte is essential in the construction of TF-SOFCs with metal supports. When the density of the thin film electrolyte is insufficient, the OCV is lowered, and the electrochemical stability of the cell is reduced due to side reactions caused by the fuel permeation phenomenon as well as structural stability. Before verifying the electrolyte of 1 μm level on the metal support, the YSZ electrolyte and NiO-GDC anode were deposited on the Si wafer to confirm the nanostructure. NiO-GDC anode was prepared under fixed sputtering conditions, and YSZ electrolytes were sputtered at various deposition temperatures (room temperature, 300 ℃, and 500 ℃). The anode and the electrolytes' surface morphology and cross-section are shown in Figure 1515. Dense nickel oxide and GDC20 were co-sputtered to decrease the impact of the anode's surface structure on the electrolyte. And the thickness was set to about 800 nm. The YSZ electrolyte was

deposited to a thickness of 1 μm for each temperature, and it was confirmed that a dense thin film was deposited. And it can be seen that as the deposition temperature increases, the size of the grain observed on the surface increases noticeably. Further work involved doing a thorough study of the electrolyte grains.

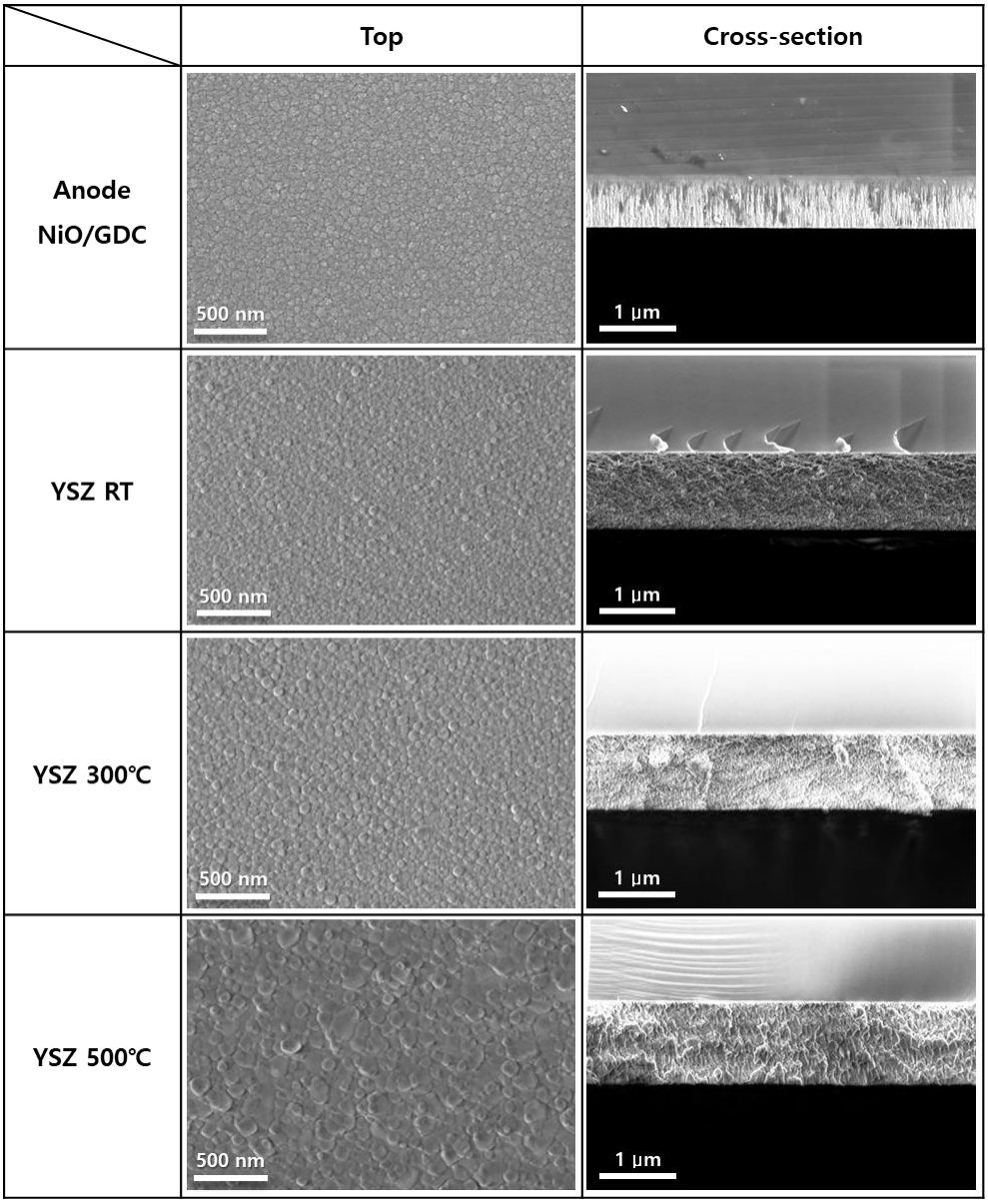

Figure 15. Surface and cross-section images of NiOGDC anode and YSZ

electrolyte on Si as observed by FE-SEM

The crystal structure of the sputtered YSZ electrolyte was verified using X-ray diffraction (XRD) analysis. Figure 1616 exhibits the XRD result of the electrolyte deposited according to various temperatures. The red vertical lines at the bottom of the graph are the powder YSZ peak (PDF#00-030-1468) of the cubic phase, and the exact peak positions are described in Table 66. The cubic phase YSZ electrolyte was effectively deposited by reactive sputtering, as demonstrated by a comparison of the XRD peaks of the electrolytes deposited at three different temperatures with the reference material. The change in grain size according to the deposition temperature is shown in the surface image of Figure 1515 can also be confirmed through the XRD results. As the grain becomes larger, the width of each peak decreases and changes sharply, and as the electrolyte sputtering temperature increases, the shape of the peak changes sharply. The change in grain size was clearly seen in the preferred orientation such as (111) and (200) planes.

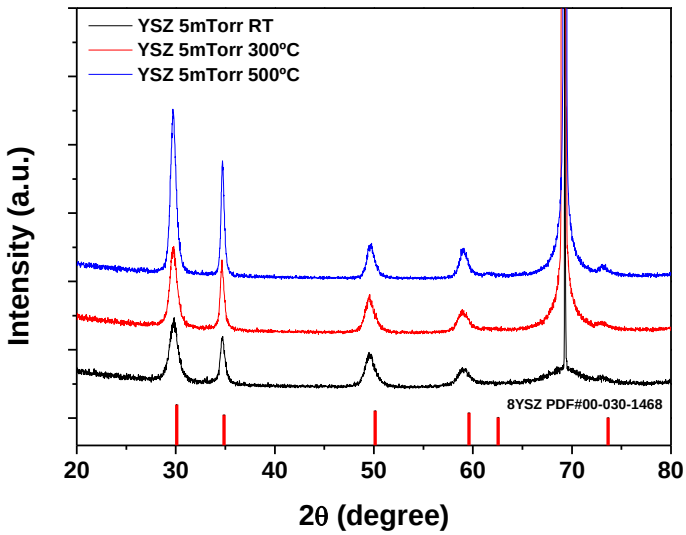

Figure 16. X-ray diffraction results of YSZ electrolyte according to the deposition temperature

In addition, the XRD results indicate the residual stress of the deposited electrolyte. In accordance with the Bragg's law depicted below, the angle of incidence (θ) can be used to calculate the interplanar distance (d) and identify whether compressive or tensile stress is present.

$$\text{Bragg's Law: } n \cdot \lambda = 2 \cdot d \cdot \sin\theta$$

Therefore, if peak shift occurs in a positive direction of the position of the reference bulk material, the d value decreases, which means that the interplanar distance d is reduced due to the presence of compressive stress in the vertical direction of the deposited film. In the case of thin films, the compressive stress perpendicular to the plane causes in-plane tensile stress. The data in Table 66 shows that all crystalline planes of various deposition temperature have been shifted in the negative direction of the reference peak. This means that all deposited electrolytes

are subjected to tensile stress in the vertical direction. Additionally, it shows that the thin film electrolyte is under in-plane compressive stress.

2θ (degree)	(111)	(200)	(220)	(311)
Room Temp.	29.811	34.705	49.525	59.233
300℃	29.746	34.661	49.545	58.926
500℃	29.738	34.717	49.702	59.104
Ref. (Bulk)	30.084	34.868	50.136	59.597

Table 6. Peak position data of each crystalline orientation extracted from the XRD patterns

Grain size was analyzed through quantitative analysis as well as qualitative analysis. The information in the XRD pattern was used, and the Scherrer equation was used for crystallite size calculation. As seen below, the Scherrer equation is expressed.

$$\text{Scherrer equation: } D = \frac{K \cdot \lambda}{\beta \cdot \cos\theta}$$

where D is the average grain size, λ is the wavelength of the incident X-rays, K is the shape factor, β is the Full Width Half Maxima (FWHM), and θ is the Bragg diffraction angle. Table 77 shows the result of the grain size calculated through the XRD pattern. Four crystalline planes with distinct peaks were used, and as a result of the calculation, the grain size increased as the deposition temperature increased. In the case of the (111) plane with the highest intensity, the grain size

increased by about 1.5 times.

Crystallite size (nm)	(111)	(200)	(220)	(311)
Room Temp.	9.35	16.92	8.8	7.77
300℃	11.24	20.43	9.43	8.24
500℃	14.1	24.96	11.24	10.36

Table 7. Crystallite size of YSZ electrolyte according to the deposition temperature

For a more profound analysis of crystallinity and atomic arrangement, deposited YSZ electrolytes were analyzed by the HR-TEM. Figure 17 17 shows an atomic arrangement in (a, c, e) and electron diffraction patterns in (b, d, f). The atomic arrangement and grain of the YSZ electrolyte can be seen in the HR-TEM images, but the grain size is difficult to confirm clearly. The electron diffraction pattern in Figure 1717(b, d, f) confirms that the sputtered electrolytes are polycrystalline material. When analyzing a single crystal material through SAED, well-aligned dots appear. However, in the case of polycrystalline materials, a ring pattern appears because the grains have various orientations in the selected analysis area. Therefore, it can be seen that the sputtered electrolyte is a polycrystalline material. As the deposition temperature increases, the electron diffraction pattern appears to change from a ring pattern to a dot pattern because the grain size increases and the number of grains present in the unit analysis area decreases. The correlation between the deposition temperature and grain size can be determined in this manner.

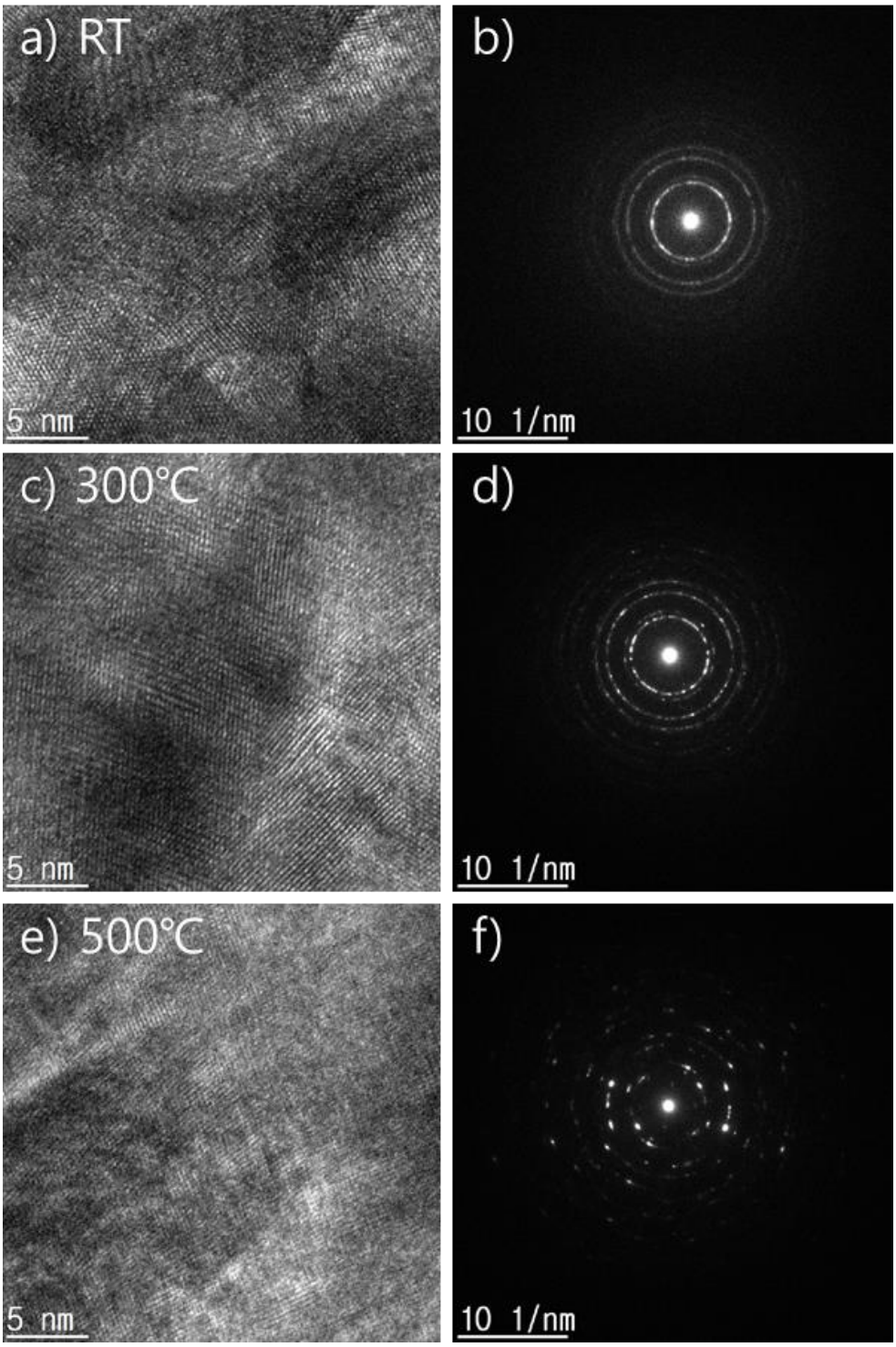

Figure 17. High-resolution transmission electron microscope (a,c,e) and selected area electron diffraction (SAED) patterns (b,d,f) of YSZ electrolyte with various deposition temperature

At the 8 mol% Y_2O_3 doping concentration, the YSZ electrolyte is known to have the maximum ion conductivity. Therefore, an XPS analysis was conducted to check the doping ratio of the reactive sputtered YSZ electrolyte. Table 8 shows the ratio of elements according to the deposition temperature. In all three cases, it was confirmed that the yttria doping concentration was about 8-9 mol %, which had an appropriate ion conductivity.

Temperature	Room Temperature	300℃	500℃
Zr 3d (At %)	28.60	28.96	29.76
Y 3d (At %)	5.23	5.27	5.95
O 1s (At %)	66.16	65.77	64.29
Y_2O_3 mol%	8.38	8.34	9.09

Table 8. The composition ratio of different temperatures deposited YSZ electrolyte by X-ray photoelectron spectroscopy (XPS)

3.3.2. Electrochemical characterization of YSZ electrolyte on metal support

The electrochemical performance was measured by applying the three types of electrolytes analyzed in the previous chapter. The electrolytes were deposited on the

developed multiscale substrate, and the deposition conditions of an anode, cathode, and cathode current collector were set constantly to check only the performance change caused by the difference of the electrolyte. Figure 18 shows the surface morphology and cross-section of the electrolyte deposited on the multiscale substrate. The thickness of the electrolyte deposited on the metal support was less than 1 μm, and the tendency of the surface morphology was the same as the result of the deposition on the Si wafer. The grain grows as the deposition temperature rises, and it is clear that the grain grows significantly at 500 ℃. Additionally, the TEM cross-section of Figure 19 can confirm the nanostructure of the entire cell, and EDS results can be used to determine the individual elemental composition of each component.

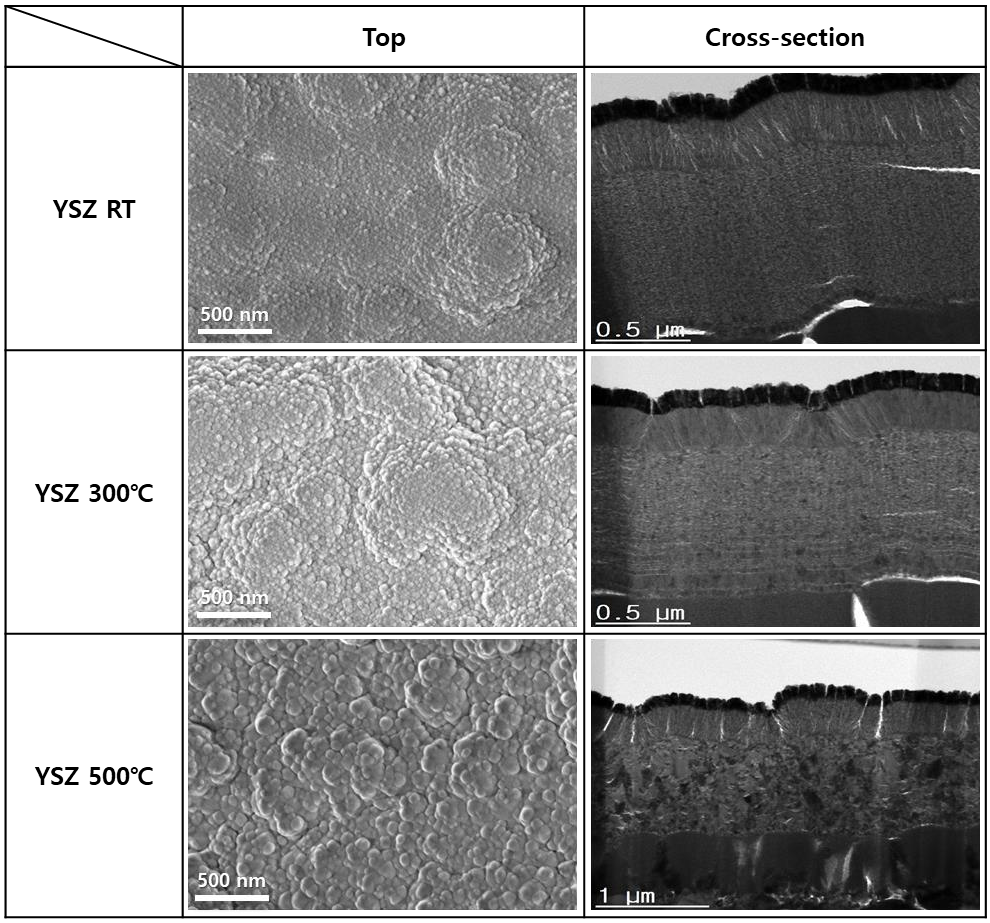

Figure 18. Surface and cross-section images of YSZ electrolyte observed by SEM and TEM

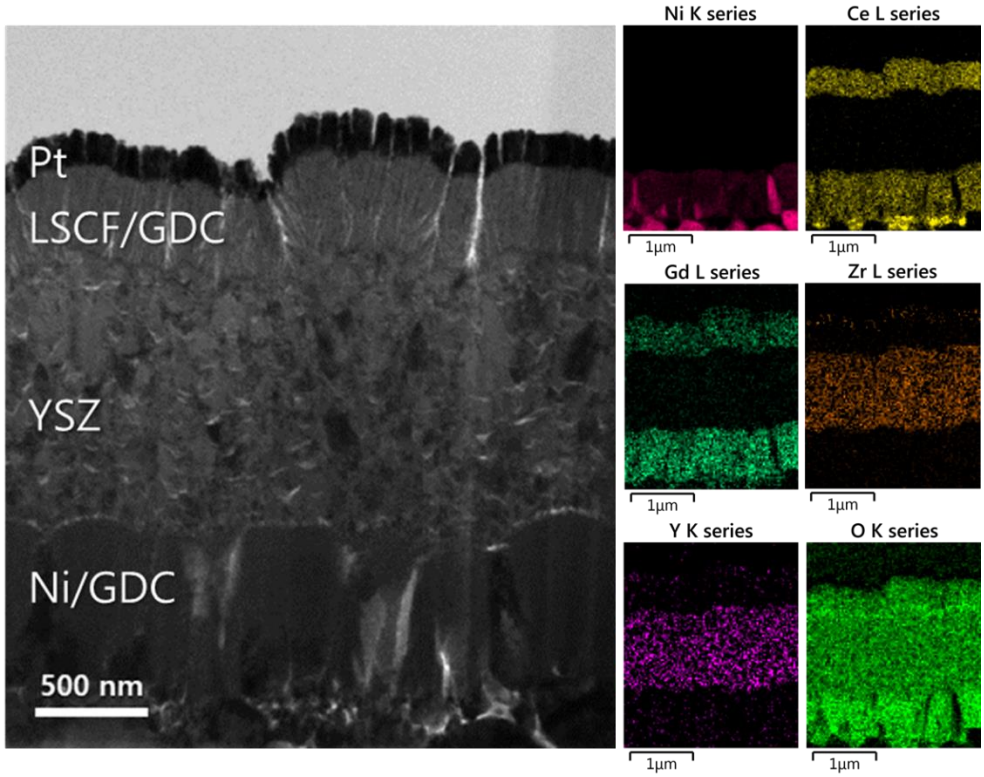

Figure 19. Cross-section and energy dispersive spectroscopy (EDS) images of MS SOFC with YSZ (500 ℃) obtained by TEM

At 500 ℃, the analysis of electrochemical performance was carried out. All three experimental cases showed an open circuit voltage (OCV) of 1 V or higher. OCV values were 1.02 V for room temperature, 1.03 V for 300 ℃, and 1.08 V for 500 ℃, respectively. In the case of 500 ℃, the OCV was similar to the theoretical value estimated by the Nernst equation. The electrolytes that were successfully deposited had an OCV of 1 V or higher because they were suitably thick, but there was a slight variation. An electrolyte sputtered at room temperature had a tiny grain, increasing the possibility of pinholes. As a result, a small amount of gas passes through the electrolyte, and the OCV is slightly reduced. Therefore, when the deposition temperature is high, the grain size increases, reducing the possibility of

pinhole generation and confirming that it is more stable. The peak power densities were 88.89 mW/cm^2 for room temperature, 188.97 mW/cm^2 for 300 °C, and 229.91 mW/cm^2 for 500 °C, respectively. This performance discrepancy was brought on by the different ion conduction characteristics of the electrolyte because all other components except the electrolyte are the same.

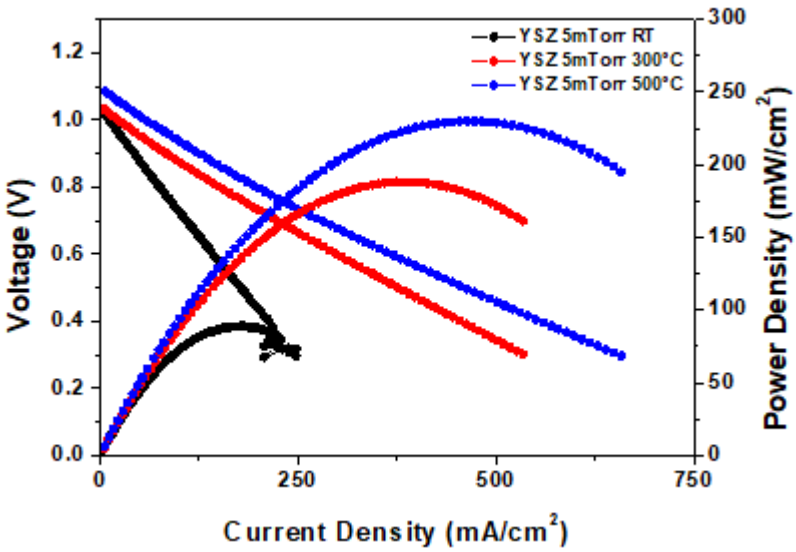

Figure 20. I-V-P curves of YSZ electrolyte with various deposition temperatures on MS SOFC

The difference in electrochemical performance was thoroughly analyzed using electrochemical impedance spectroscopy (EIS), and the bias voltage conditions were set to OCV, and 0.6 V. Figure 21 shows the EIS measurement results. An equivalent circuit of the measured Nyquist plot was constructed to distinguish the factors of performance degradation. As a result, the equivalent circuit was composed of one resistor (R) and three parallel combinations of a resistor and a capacitor (RC). An x-

axis intercept in a high-frequency area is typically thought to be an ohmic resistance produced in an electrolyte's ion conduction, however in the case of a thin film electrolyte, resistance by a grain boundary may also be observed. In this case, the equivalent circuit of electrolyte resistance is represented by the sum of one R component and one RC component. Since the bias voltage does not change Ohmic resistance, it is possible to confirm the suitability of the equivalent circuit because the semi-circle of the high current region of the Nyquist plot measured under two bias voltages does not change. The measured ohmic resistance were 2.43 $\Omega \cdot cm^2$ for RT, 0.99 $\Omega \cdot cm^2$ for 300 °C, and 0.84 $\Omega \cdot cm^2$ for 500 °C, respectively. As the electrolyte's deposition temperature rose, the ohmic resistance dropped. While the effect of the grain boundary on the ion conductivity is controversial, many studies have reported that the ion conductivity of the grain boundary is 1 to 2 orders lower than that of the grain core [69]. According to this interpretation of the experiment results, the grain size increases and the grain boundary density reduces as the electrolyte's deposition temperature rises. The ohmic resistance was noticeably reduced due to the reduction of the grain boundary with relatively low ion conductivity. However, in terms of triple phase boundary (TPB), since the grain boundary serves as a reaction site, the reaction rate increases as the grain boundary increases. Therefore, it is evident that the polarization resistance slightly rises at OCV at 500 °C with a large grain. Although the ohmic resistance and polarization resistance by grain boundary density are in a trade-off relationship, this experiment shows a greater effect of reducing the ohmic resistance of grain boundary, so increasing the grain size through high temperature deposition has a more positive effect on electrochemical performance.

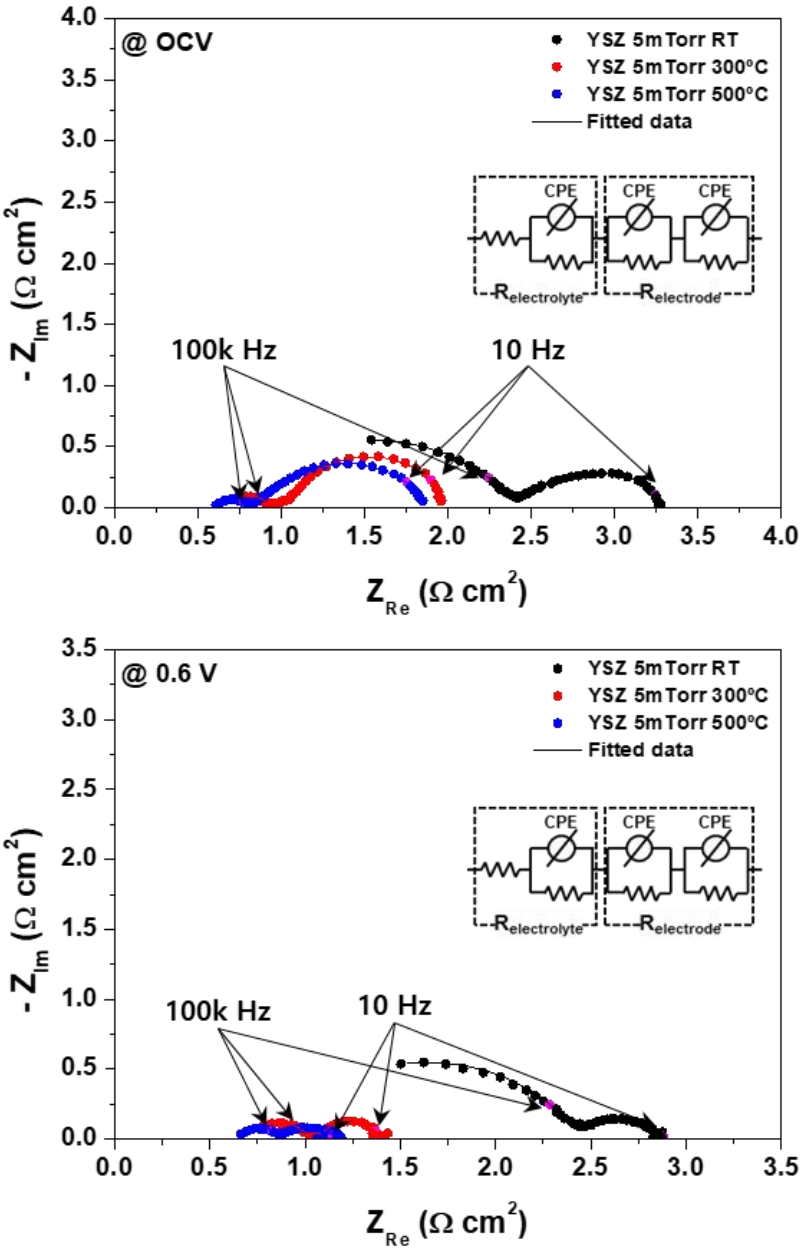

Figure 21. EIS analysis of YSZ electrolyte with various deposition temperatures on MS SOFC

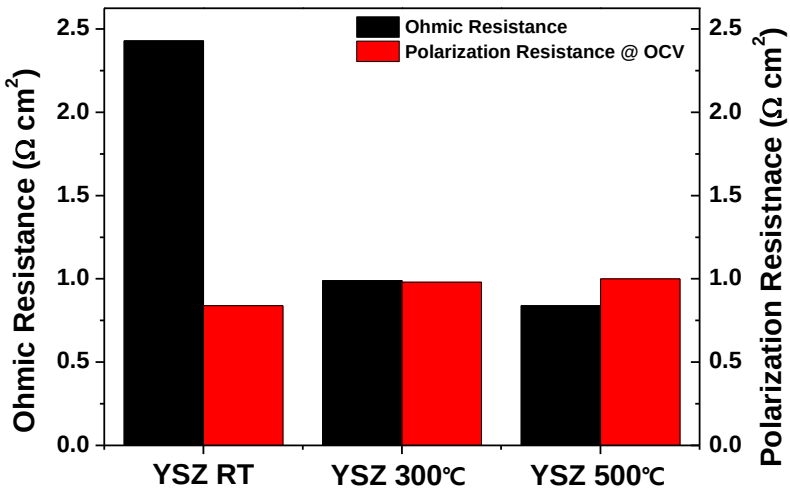

Figure 22. Graph of quantitative data of ohmic and polarization resistance in Nyquist plots (Fig.21)

3.3.3. GDC10 electrolyte: Surface morphology and film crystallinity analysis of RT and 500℃ sputtered electrolyte

To achieve good performance while lowering the operating temperature of a SOFC, a ceria-based electrolyte with high ion conductivity at a low temperature may be utilized. A thin film GDC10 electrolyte was deposited on a Si wafer to investigate its characteristics before being applied to the developed multiscale substrate. Figure 23 shows the surface morphology and cross-section of the GDC sputtered under room temperature and 500 ℃ deposition conditions. The deposition conditions were reduced to two by referring to the previous YSZ electrolyte analysis results. It was confirmed that the grain size was clearly increased through surface analysis of

GDC10 deposited at room temperature and 500 ℃.

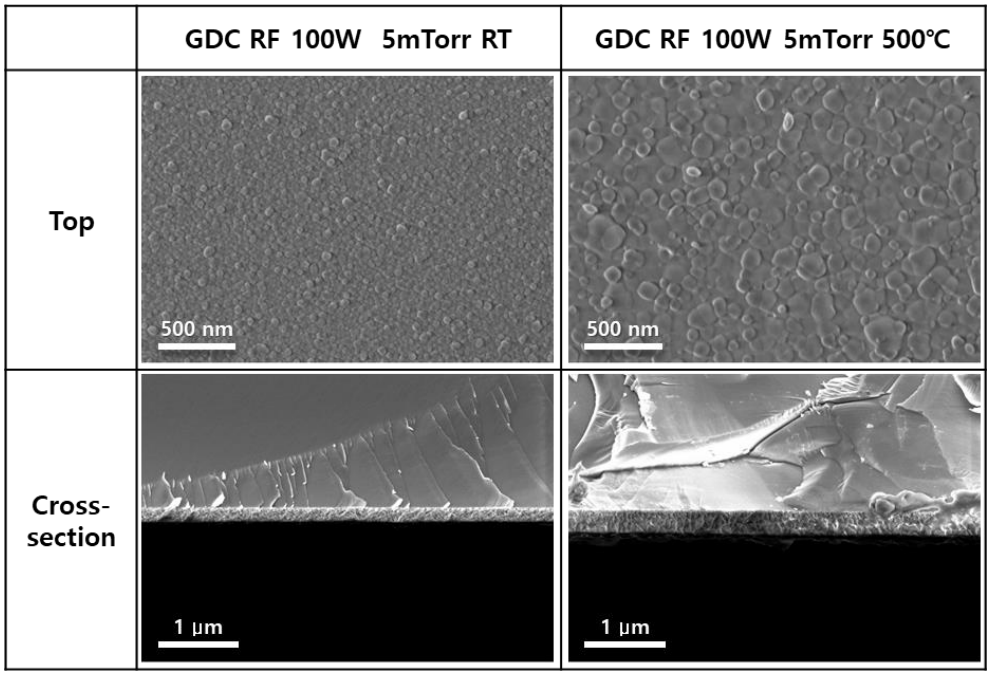

Figure 23. Surface and cross-section images of GDC10 electrolyte on Si wafer

Through the XRD analysis results in Figure 24, it was confirmed that the polycrystalline GDC10 film was deposited. When the deposition temperature is high, the peak of the crystal plane becomes more pronounced and sharp so that the grain size can be compared. The Scherrer equation was used to determine the grain size, and the results are shown in Table 10. The grain size increased significantly on the crystal plane with the highest intensity. In the case of (311) plane, the crystal size was reduced, which seems to be an error caused by the lack of a clear peak in room temperature deposition. The peak positions of each crystal plane are described in Table 9, and it is confirmed that tensile stress exists in a direction perpendicular to the plane through Bragg's law.

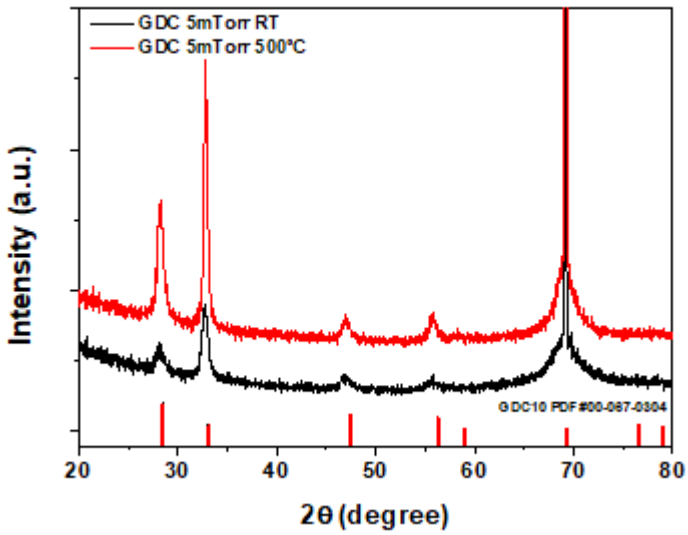

Figure 24. X-ray diffraction (XRD) result of sputtered GDC10 electrolyte with different deposition temperature

2θ (degree)	(111)	(200)	(220)	(311)
Room Temp.	28.119	32.698	46.730	-
500℃	28.257	32.791	47.020	55.785
Ref. (bulk)	28.513	33.041	47.424	56.270

Table 9. Peak position data of each crystalline orientation extracted from the XRD patterns

Crystallite size (nm)	(111)	(200)	(220)	(311)
Room Temp.	11.08	13.49	10.63	13.75
500℃	12.72	23.42	11.75	11.68

Table 10. Crystallite size of GDC10 electrolyte according to the deposition temperature

For further analysis of crystallinity and atomic arrangement, the deposited GDC10 electrolyte was analyzed by HR-TEM. Figure 25 shows the atomic arrangement in (a) and the electron diffraction pattern in (b). The electron diffraction pattern of Figure 25(b) shows that the sputtered electrolyte has a polycrystalline structure. Since there is a crystal plane with various directions in the analysis area, a diffraction pattern in the form of a faint ring may be confirmed.

For the GDC10 electrolyte, it is known that the ion conductivity is the highest at a doping concentration of 10 mol% of Gd_2O_3. In order to confirm the doping ratio of the GDC electrolyte prepared by sputtering, an XPS analysis was carried out. The ratio of elements according to the deposition temperature is shown in Table 11 below. Due to the difference in the sputtering yield of each element, a doping ratio of a sputtering target was not applied to a thin film as it is, but the difference was not significant.

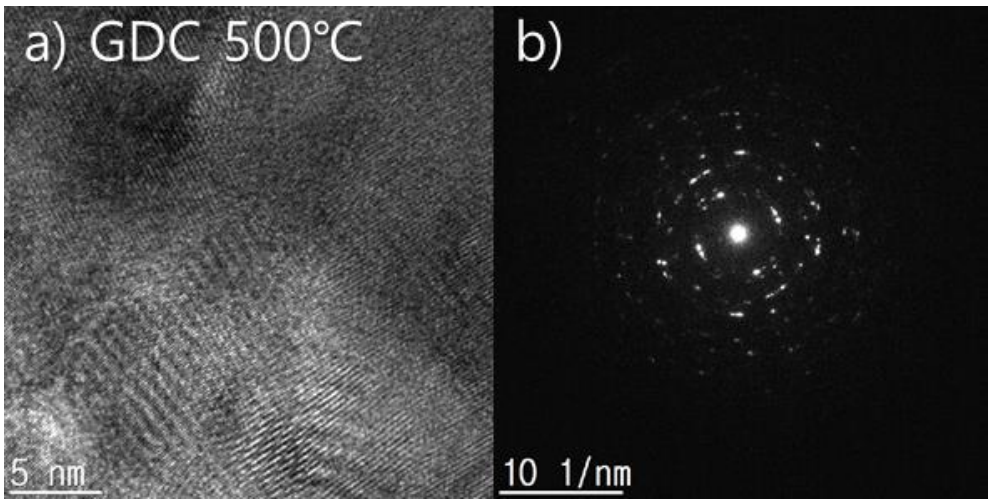

Figure 25. High-resolution transmission electron microscope (a) and selected area electron diffraction (SAED) patterns (b) of GDC10 electrolyte

Temperature	Room Temp.	500℃	Target (ref)
Ce 3d (At %)	31.30	30.07	29.49
Gd 4d (At %)	10.26	10.70	8.32
O 1s (At %)	58.44	59.23	62.19
Gd_2O_3 mol%	14.08	15.10	12.36

Table 11. The composition ratio of different temperature deposited GDC10 electrolyte by XPS

3.3.4. Performance enhancement by applying YSZ/GDC bilayer electrolyte for Metal Supported Low-temperature SOFCs

To compare with the experimental results of the previous chapter, electrochemical performance analysis was performed at 500 °C. The experiment was conducted by setting the electrolyte to a thickness of 1 μm and depositing a GDC monolayer electrolyte and a YSZ/GDC bilayer electrolyte. The monolayer GDC showed an OCV of 0.7 V, as shown in Figure 26. As a result of reducing Ce^{4+} to Ce^{3+} in a reducing atmosphere, the GDC electrolyte has electrical conductivity. Thus, electrons are conducted through the electrolyte, causing an electric short or lowering the OCV. Therefore, many studies applied an electron-blocking layer together when using a ceria-based electrolyte [13,17,78,79]. YSZ/GDC bilayer electrolyte was prepared for the above reasons, and YSZ was used as an electron-blocking layer. In this case, an OCV of 1.07 V, similar to that of the YSZ monolayer electrolyte, was obtained. Therefore, even with a YSZ layer thickness of 200 nm, electron conduction is effectively prevented. And the peak power densities were 697.04 mW/cm^2 GDC monolayer and 699.83 mW/cm^2 for YSZ/GDC bilayer. By applying the YSZ blocking layer, an electrically stable fuel cell with a similar performance to that of using only the GDC electrolyte was fabricated.

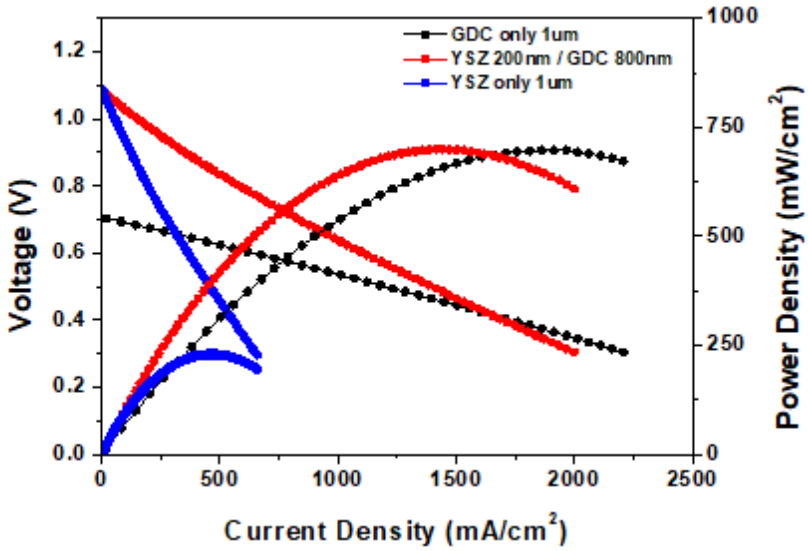

Figure 26. Current-Voltage behavior of MS SOFC with GDC and YSZ monolayer and YSZ/GDC bilayer electrolyte

Figure 27 shows the nanostructure of the developed multiscale metal-supported SOFC to which the developed YSZ and GDC electrolytes are applied. The thickness of the entire cell, including the electrode, electrolyte, and current collector, is less than 2.5 μm, while the electrolyte thickness of the deposited bilayer is close to 1 μm. The structure and location of the YSZ electrolyte through EDS analysis can be clearly identified.

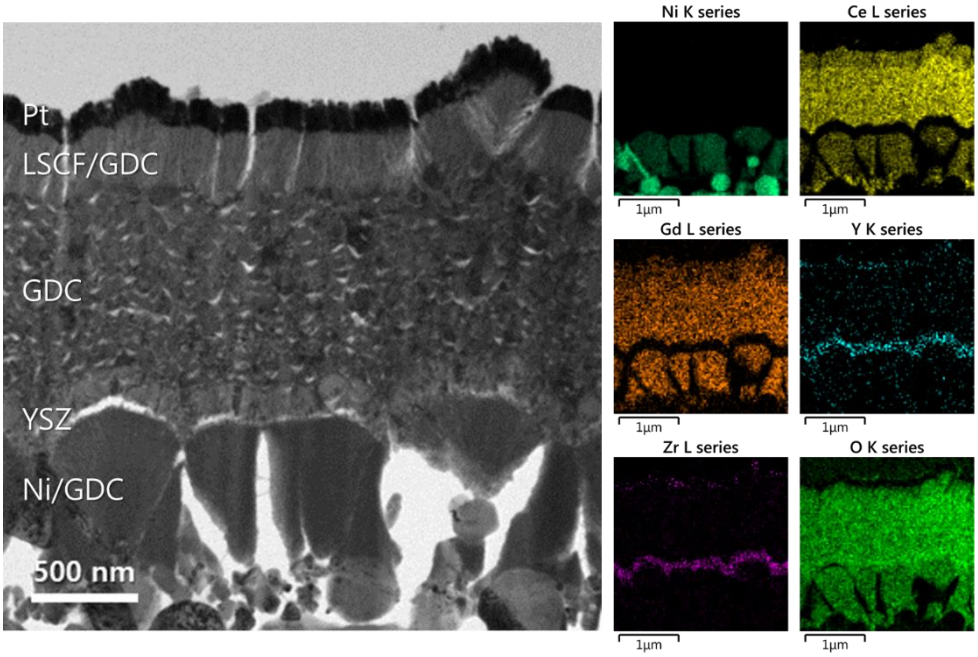

Figure 27. Cross-section and energy dispersive spectroscopy (EDS) images of MS SOFC with YSZ/GDC bilayer electrolyte obtained by TEM

To thoroughly investigate the deterioration factor, electrochemical impedance spectroscopy (EIS) was carried out with the bias voltage conditions set to OCV and 0.6 V. Figure 28 shows the EIS results. An equivalent circuit of the measured Nyquist plot was constructed to distinguish the factors of performance degradation. As a result, the equivalent circuit was composed of one resistor (R) and two parallel combinations of a resistor and a capacitor (RC). Unlike the monolayer YSZ electrolyte, the ohmic resistance from the grain boundary was not shown, so the x-axis intercept was ohmic resistance. The measured ohmic resistance was 0.15 $\Omega \cdot cm^2$ for the GDC monolayer electrolyte and 0.26 $\Omega \cdot cm^2$ for the YSZ/GDC bilayer electrolyte. Despite the low OCV, the GDC monolayer electrolyte showed high performance, which was attributed to its superior ion conductivity at low temperature. Both ohmic and polarization resistance increased compared to monolayer GDC for

bilayer electrolytes because of applying the YSZ electron blocking layer. Although the activation and ohmic loss were slightly increased, the peak power density was similar due to the stable and high OCV.

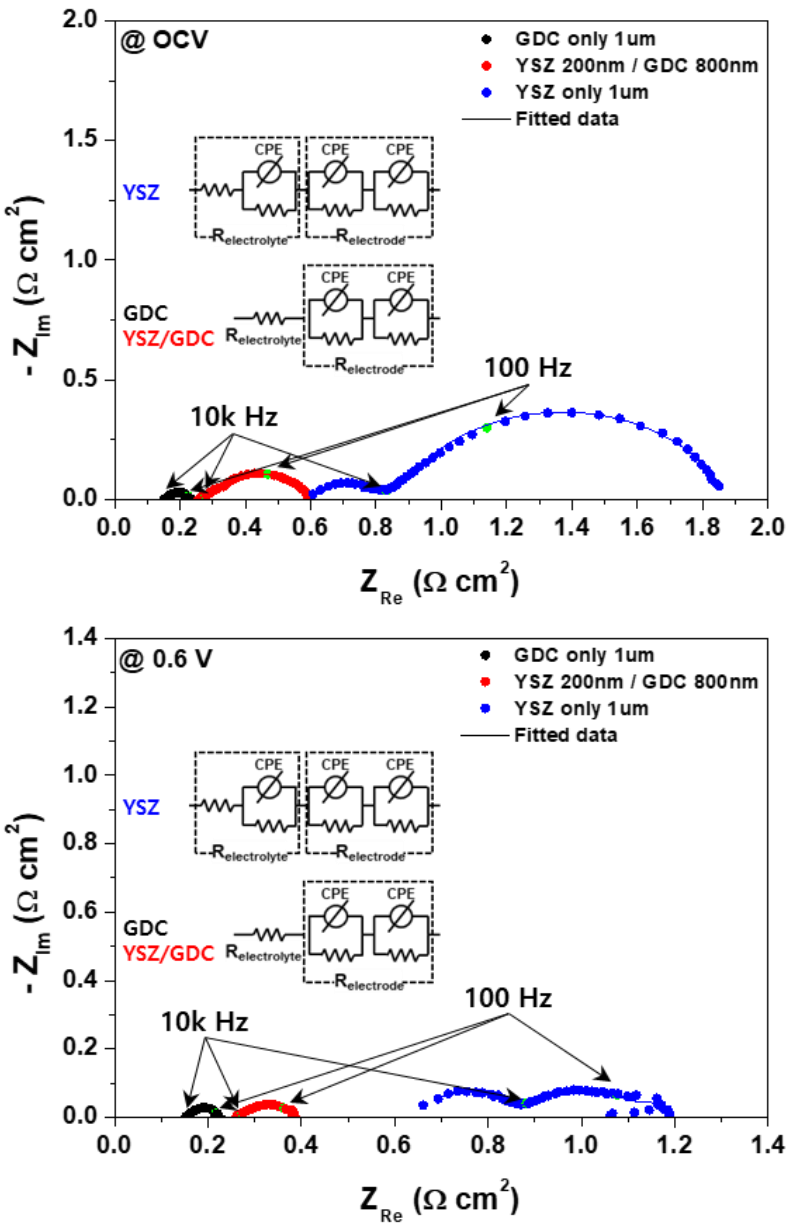

Figure 28. EIS analysis of MS SOFC with GDC and YSZ monolayer and YSZ/GDC bilayer electrolyte

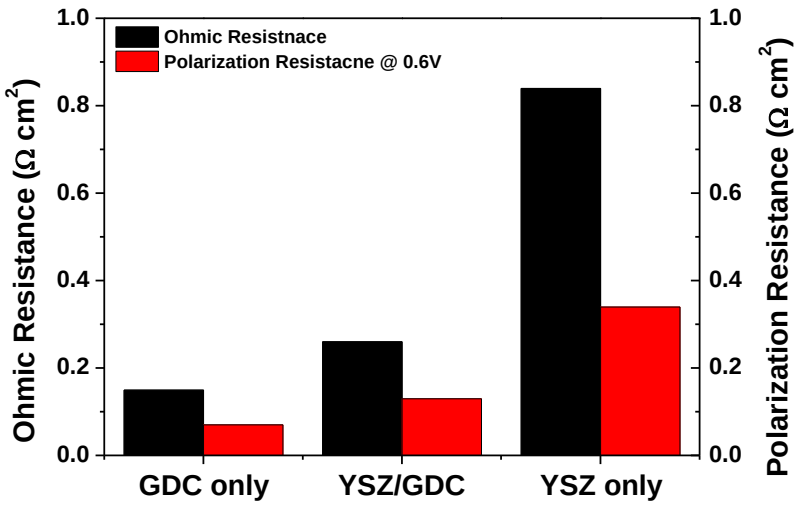

Figure 29. Graph of quantitative data of ohmic and polarization resistance in Nyquist plots (Fig.28)

3.4. Conclusion

In this study, YSZ and GDC electrolyte were sputtered to fabricate dense electrolytes for metal supported TF-SOFC. YSZ electrolytes were deposited under various substrate temperatures and characterized. For GDC electrolytes, sputtering was conducted at 500 ℃, referring to the characteristics of YSZ electrolytes according to the sputtering temperature. The change in the characteristics of the electrolyte grain according to the sputtering temperature and its effect on the ion conductivity was investigated. In addition, it was successfully applied to the metal supported TF-SOFC to obtain a stable open circuit voltage. A YSZ/GDC bilayer electrolyte was manufactured applying a GDC electrolyte to achieve high

performance even in low-temperature operation. As a result, the cell generated 699.83 mW/cm^2 of peak power density, which increased three times compared to the monolayer YSZ electrolyte.

Chapter 4. Nano-Structured NiO-GDC Composite Anode by Reactive Co-Sputtering

4.1. Introduction

Unlike fuel cells operating at a low temperature of less than 200 ℃ (e.g. PEMFC), SOFCs have an advantage that a precious metal Pt catalyst is not required. High electronic conductivity and high catalytic activity are required of the anode employed as the anode in order to effectively oxidize hydrogen and hydrocarbons. Structurally, it should have adequate porosity for fuel diffusion and high mechanical and thermal stability [80]. A cermet electrode, which is a composite of nickel and oxygen ion conductive ceramic, is widely used as a material having these characteristics. Nickel has the disadvantage of being vulnerable to contamination (carbon and sulfur), but it shows excellent performance under hydrogen fuel operation.

In general, a nickel-based cermet electrode is manufactured by mixing powder of a desired weight ratio and sintering at a high temperature. Generally, nickel-based cermet electrodes with a volume ratio of 40-50 % are widely used. In this regard, previous studies on performance change according to the anode composition ratio have been reported [80–85]. However, if the manufacturing method through high-temperature sintering is used, complicated processes from slurry preparation to high-temperature sintering are required several times in order to verify various composition ratios. By varying the power applied to the target, on the other hand, when the co-sputtering method is used, it is simple to change the composition ratio. Control of the composition ratio through the co-sputtering process is affected by the

sputtering rate. The sputtering rate of oxides is much slower than that of metallic materials. This occurs due to the difference in the binding energy of the atoms of the target. Since the binding energy of atoms in the ceramic target is stronger than that of the metal bonding, the sputtering rate is slow [86]. Therefore, there is a limit to matching the composition ratio by co-sputtering of the metal target and the ceramic target. To improve this, a reactive sputtering process of a metal material was used. As can be seen in figure 30, for reactive sputtering, the deposition rate is slowed to a degree similar to that of the ceramic target. Using this point, the ratio of nickel and ceramic can be adjusted as required.

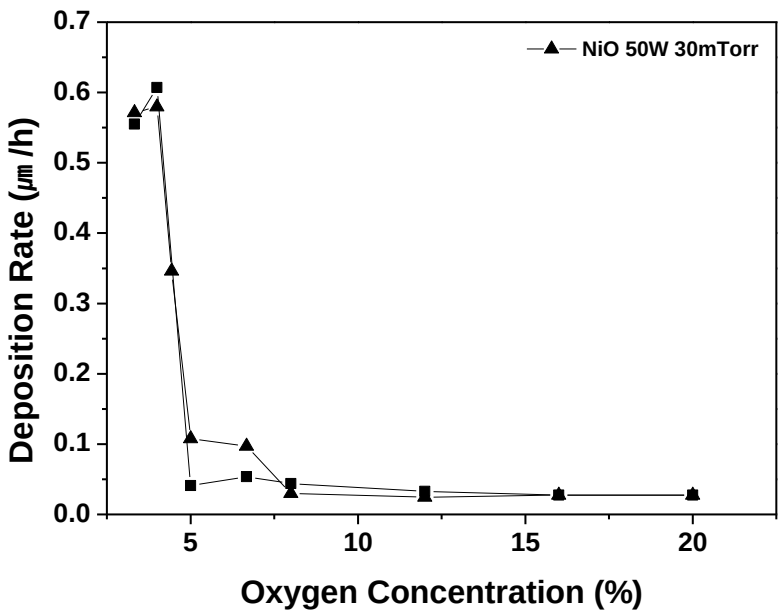

Figure 30. NiO reactive sputtering deposition rate according to oxygen concentration

As the nickel content in the cermet electrode increases, the electrical

conductivity and porosity tend to increase. However, as the nickel content increases, the nickel easily agglomerates at high temperatures, and the TPB decreases, so there is an optimal nickel/ceramic composition ratio. J.R. Wilson et al. reported that the optimum volume fraction of the Ni solid in the active layer of anode-supported SOFC was 0.34 [81]. Through 3D analysis using FIB-SEM, they reported the effect of tortuosity and contiguity on performance as well as TPB change according to the composition ratio of the active layer. Y. Lim et al. reported the optimal volume ratio of the Ni-SDC cermet anode in AAO-based SOFC. After manufacturing cermet anodes with varied composition ratios through the adjustment of the applied power, the anodes were applied to electrolyte-supported SOFC to investigate the optimal conditions. Then, the electrode under the same conditions was applied to the AAO-based SOFC to obtain a performance of 178 mW/cm^2 at 450 ℃ [85]. In the above experiment, the optimized performance was obtained at a nickel ratio of 58.77 vol %, which has a relatively higher nickel content than that of an anode support. This difference seems to be due to the difference in the current collecting direction in the anode and the presence or absence of conductivity of the support. Therefore, since the optimal composition differs depending on the support type, it is necessary to investigate the optimal volume ratio in the metal support.

In this chapter, NiO-GDC electrodes were fabricated through the reactive co-sputtering process of Ni and GDC. The current collecting direction of an anode varies depending on whether the substrate used is conductive, so the optimal Ni and GDC ratio also varies. Therefore, electrodes of various ratios were fabricated using the sputtering process and characterized using analytical methods. The metal support was coated with anodes of varying composition ratios, and an experiment was conducted at 500 ℃ to verify the electrochemical performance and confirm the optimal conditions.

4.2. Experimental

NiO and NiO-GDC composite anode were prepared by co-sputtering process. 2 in sized metal Ni and GDC20 ceramic targets were mounted on DC and RF guns, respectively. The composition ratio was adjusted by altering the applied power in order to optimize the ratio of Ni and GDC. In the case of Ni, the power was set to 50 W – 100 W, and in the case of GDC20, it was set to 50 W and 75W. Four cases of NiO-GDC anodes were manufactured according to the applied power. Anode was deposited on the developed 1 x 1 cm^2 multiscale support through reactive co-sputtering. The chamber was vacuumed for low pressure environment to less than 1 x 10^{-4} Torr. The reactive co-sputtering was conducted in a 4.0 Pa (30 mTorr) Ar/O_2 environment. Ar and O_2 gases were supplied at 20 sccm, and 5 sccm, respectively. The electrolyte was prepared under the best conditions selected in the previous chapter. Y-Zr alloy (16:84 at %) and ceramic GDC10 (Gd 10 mol % doped, RND Korea, South Korea) targets were used, and the stage was set to 500 °C. In addition, the bilayer YSZ/GDC10 electrolyte was sequentially deposited using a recipe in a sputtering system. The working pressure was set to 0.67 Pa (5 mTorr) after evacuating the chamber pressure under 1 x 10^{-4} Torr. Reactive sputtering was carried out using Y-Zr and GDC10 with DC 200 W and RF 100 W, respectively, under an Ar/O_2 (20/5 sccm) mixed atmosphere.

Lastly, after limiting the reaction area to 1 x 1 mm^2 with a homemade physical mask, 300 nm of porous LSCF ($La_{0.6}Sr_{0.4}Co_{0.2}Fe_{0.8}O_{3-\delta}$, Advanced Engineering Materials, China) -GdCe (Gd 20mol %, Advanced Engineering Materials, China) cathode and 200 nm of Pt current collector were sequentially deposited. The sputtering power applied to LSCF, GdCe, and Pt were 100 W, 60 W, and 100 W, respectively. In addition, the working pressure was kept at 4.0 Pa (30 mTorr) for the cathode and 8.0 Pa (60 mTorr) for the current collector at an inert Ar and room

temperature environment.

Four cases of NiO-GDC anode were prepared on Si wafer and the cross-sectional images and surface morphology were observed by FE-SEM. In order to confirm the crystallinity of sputtered NiO-GDC anode in an operating environment, an XRD analysis was conducted by preparing samples before and after reduction at 500 °C for 1 h. After the electrochemical test, the cells were examined by FIB-SEM (FIB, Crossbeam 550, Carl Zeiss, Germany) and HR-TEM (JEM-2100F JEOL, Japan) in order to investigate at the anode's surface and cross-sectional structure. Using an X-ray Fluorescence Spectrometer (XRF, XRF-1700, Shimadzu, Japan), the composition ratio of the NiO-GDC anode was examined. And the volume ratio was calculated through the weight ratio.

The fabricated metal support TF-SOFCs were mounted on a homemade stainless steel jig, and the metal substrate and the jig were connected using an Ag paste. Additionally, a ceramic sealant was used to physically divide the anode and cathode sides. After that, the experiment was conducted after a half-day drying process. The experiment was conducted in a high-temperature furnace at 500°C, and 3% humidified hydrogen was supplied to the anode at 100 sccm, and the cathode was exposed to ambient air. The electrochemical behavior was confirmed using a commercial potentiostat (Gamry Reference 600, USA). For further analysis, electrochemical impedance spectroscopy (EIS) analysis was performed in the range of 1 MHz to 2 Hz, and the bias voltages of OCV and 0.6V were applied.

4.3. Result & Discussion

4.3.1. Investigation of the Morphology and Composition Ratio of Co-sputtered NiO-GDC Film

Compared to the conventional manufacturing process of anode support or electrode with slurry, the co-sputtering process has an advantage in that a metal/ceramic ratio is easily controlled. Therefore, in this study, the ratio of Ni and GDC20 was adjusted through applied sputtering power. The applied sputtering power ratio of the composite anode was set to 0.67, 1, and 1.5. From now on, samples for each Ni/GDC ratio are expressed as NiO50/GDC75, NiO50/GDC50, and NiO75/GDC50, respectively. And NiO100 for pure NiO anode. The cross-section and surface morphology of the sputtered films on the Si wafer are shown in Figure 31. For more structural stability, the Ni catalyst was reactively sputtered in an oxide state rather than a metal state. A thin film with small holes is produced as a result of co-sputtering, as can be observed. The film thickness was fixed to 800 nm, and for NiO50/GDC75, the Ni content was very low, so the columnar structure of the cross part was not clearly illustrated.

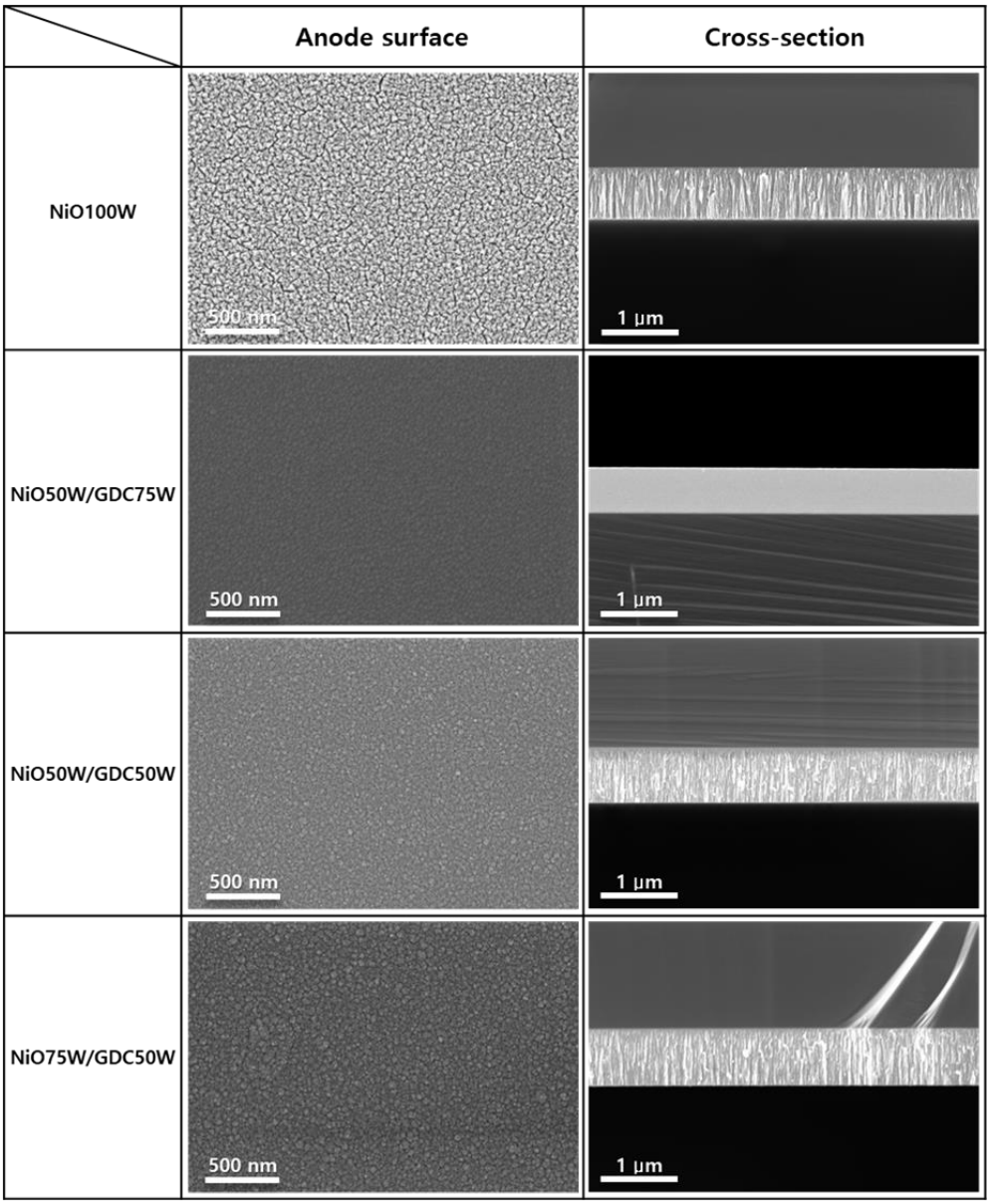

Figure 31. Surface and cross-section images of NiO-GDC20 anodes deposited on Si wafer

Except for the case of NiO50/GDC75, it was difficult to confirm a significant difference in surface morphology and cross-section. Therefore, to confirm the difference by case, the element composition ratio of the thin film was examined using

XRF. Through XRF analysis, the weight percent of each element can be determined. Therefore, the volume ratio was calculated based on the obtained weight percent and shown in Table 12.

Vol%	NiO50/GDC75	NiO50/GDC50	NiO75/GDC50
Ni	24.02	49.5	61.5
GDC20	75.98	50.5	38.5

Table 12. The calculated volume ratio of co-sputtered NiO-GDC20 anode under various conditions obtained by X-ray Fluorescence Spectrometer (XRF)

When the anode of the above conditions is applied to the SOFC, the reduction process must be performed. Only after going through a high-temperature reduction process, the deposited dense NiO anode is reduced to Ni, which acts as a catalyst and changed into a porous structure so that fuel can pass through. In order to validate the anode's material properties at the working temperature, XRD analysis was carried out. H_2 of 100 sccm was supplied at the operating temperature of 500 ℃ for 1 h to investigate the change in crystallinity of the thin film. It could be verified that, even if an anode deposited on Si wafer has an amorphous form without crystallinity, the Ni catalyst and GDC20 electrolyte become crystalline and operate as MIEC electrodes after 1 hour of reduction.

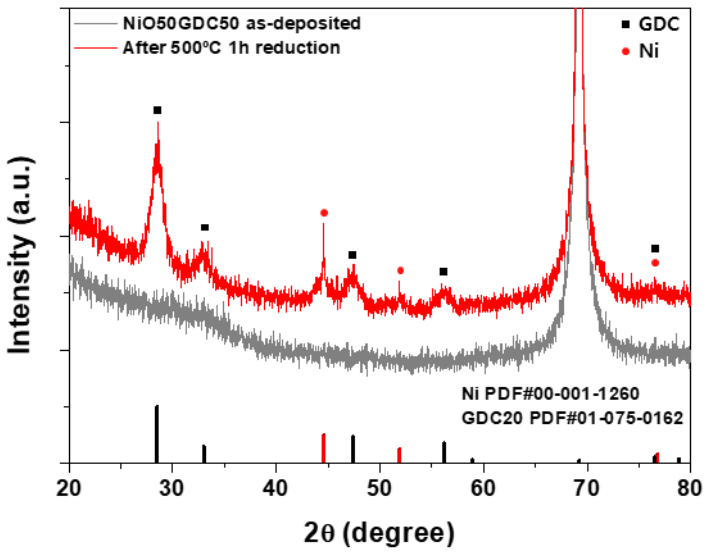

Figure 32. Comparison of crystallinity before and after exposure to the operating environment of the co-sputtered anode by XRD

In order to investigate the nanostructure of NiO-GDC anode, HR-TEM analysis was carried out. As shown in Figure 33(a), the atomic arrangement of grains with various orientations can be identified. This means a polycrystalline structure, which can be confirmed through the electron diffraction pattern of Figure 33(b) appearing in a ring shape. In the polycrystalline structure, crystal planes with high intensity of XRD results were shown as a distinct ring pattern, GDC (111) and (220), and Ni (111) planes were clearly shown in the SAED image.

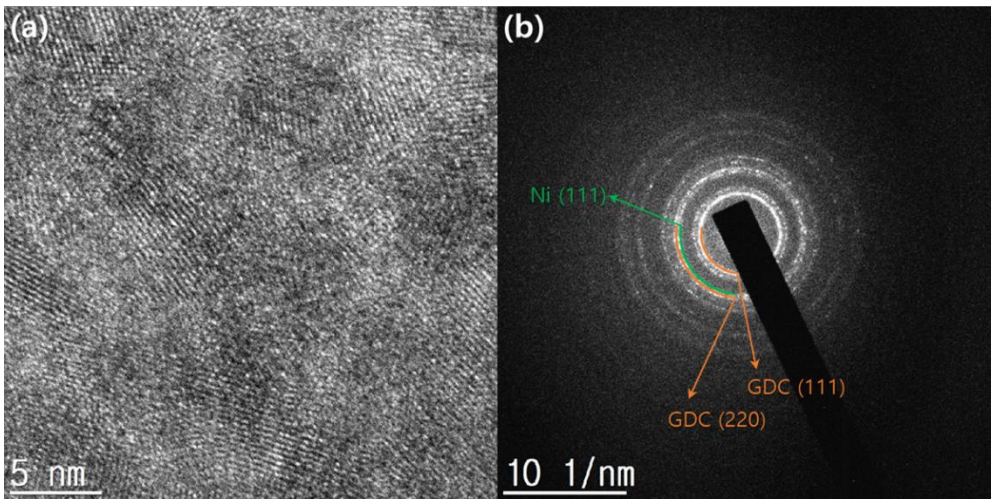

Figure 33. High-resolution TEM image and SAED pattern of NiO50-GDC50 sputtered anode.

4.3.2. Electrochemical Performance of Optimized NiO-GDC Anode Applied MS SOFC

The composite anodes, characterized in the previous chapter, were deposited on multiscale support for electrochemical performance tests. Before the cell test, the surface structure of the deposited anode was investigated through SEM. As shown in Figure 34, the columnar structure with fine pores was confirmed. The microstructure of the sputtered anode is affected by the surface profile, and unlike the structure in the Si substrate (Figure 31), the sputtered film was grown along particles having a size of less than 500 nm on the surface to form a column having a width of about 800 nm. According to a cross-sectional image of a tested cell, it could be verified that pores are generated in an anode through reduction under operating environment conditions. In the case of NiO50GDC75 having a high ceramic volume

ratio, it was found that sufficient pores were not generated even after reduction due to a low Ni content.

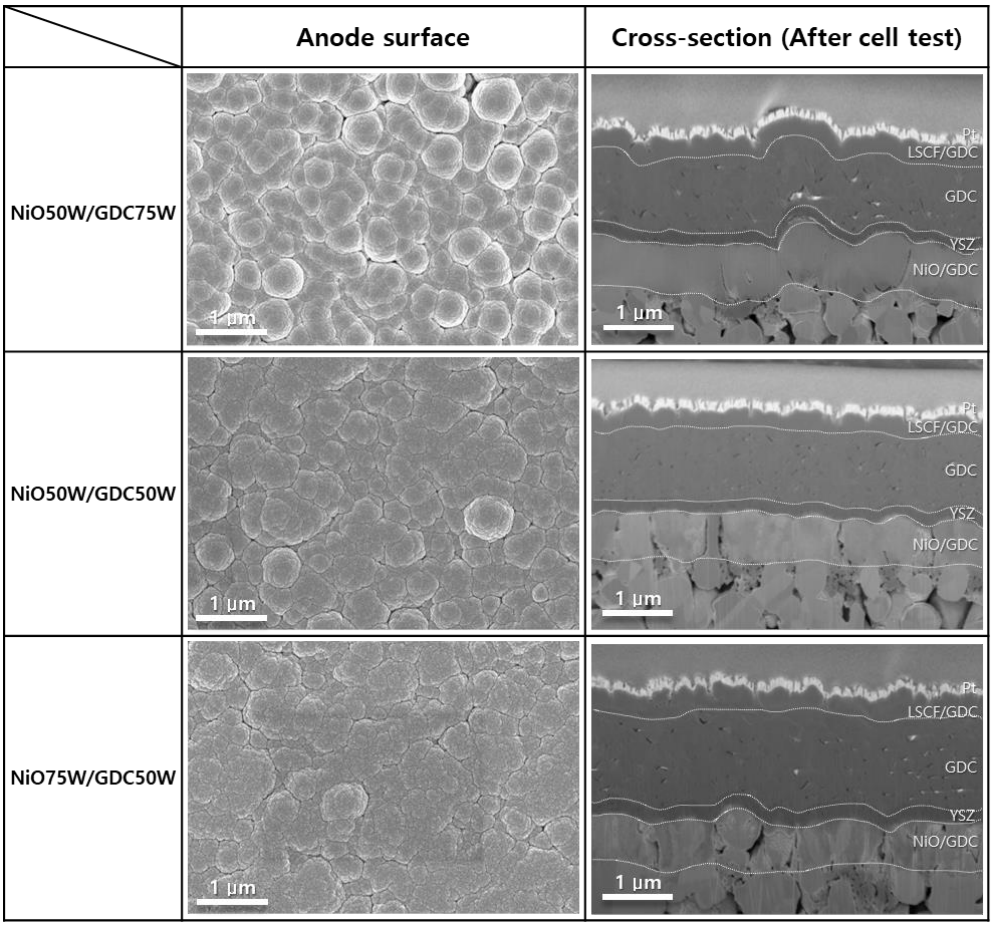

Figure 34. Surface morphology of anode and cross-section images of fabricated metal-supported cells with various Ni/GDC volume ratios

The electrochemical performance test was conducted at 500 ℃. After fabrication of the anode under each condition, the YSZ/GDC bilayer electrolyte and LSCF/GDC, and Pt current collector were simultaneously sputtered on the four samples. Therefore, the anode is responsible for the variation in cell performance.

As a result of the experiment, the OCV was 1.11 V for NiO50/GDC75, 1.07 V for NiO50/GDC50, and 1.12 V for NiO75/GDC50, respectively. The OCVs showed a value close to the theoretical voltage by more than 1 V, and a slight difference is assumed to be an error in the experimental setup. The cross-sectional structure shown in Figure 34 shows that voids occurred in the middle of the GDC10 electrolyte. If fuel is penetrated through voids, which is a defect of the electrolyte, the OCV is lowered, but the experiment result showed that a high OCV of 1V or more could be obtained. Therefore, the visible voids are a closed state that does not affect fuel crossover. The peak power density under each condition was 481.66 mW/cm^2, 699.83 mW/cm^2, and 615.89 mW/cm^2, which showed the highest performance at NiO50/GDC50. Fortunately, the anode manufacturing conditions used in the previous electrolyte optimization study were the optimal ratio. Therefore, in the case of co-sputtered anode, it was found that the optimal performance was shown at a point where the volume ratio of Ni and GDC was close to 1:1. The above result is different from the results of the papers reported on the ratio of sputtered MIEC anodes [85,87]. This difference is due to the type of substrate applied. The direction of current collection at the anode is determined depending on whether the substrate is conductive. Since there is no conductivity in AAO substrates, the current is gathered in the anode's in-plane direction. In this case, the column-to-column contact significantly affects electron conduction; in this case, a higher Ni ratio will positively impact the conductivity.

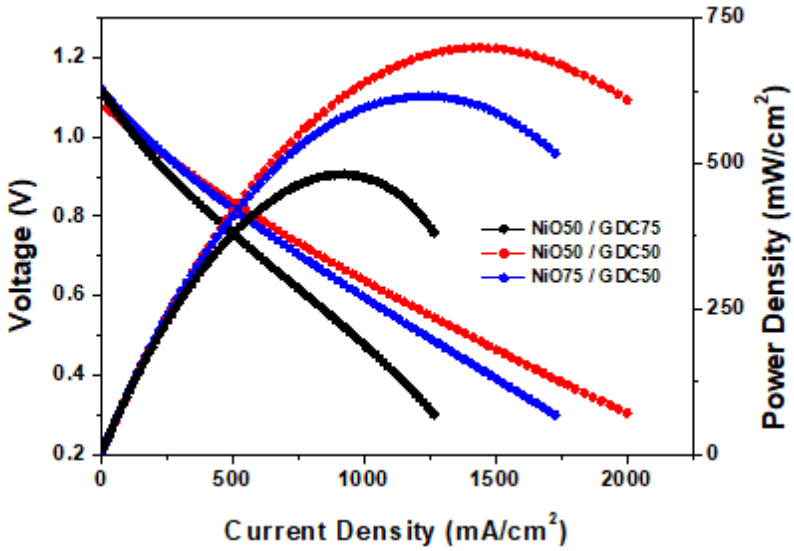

Figure 35. Measured electrochemical performance of MS SOFC with various volume ratios of NiO-GDC anode

Although four anode cases were characterized, Figure 35 shows only three cases of I-V-P behavior. In the case of NiO100, OCV was not measured due to delamination of the electrode and the electrolyte in the test environment. The surface structure of the cell after the experiment is depicted in Figure 36(c). After the experiment, the anode and the electrolyte were delaminated, and most of the substrate was exposed. The dense electrolyte was thoroughly deposited on the anode's surface of the remaining electrolyte, but it appears that the bottom anode's structure collapsed and peeled off at the same time. On the cathode surface, it can be seen that the structure of the anode located below collapsed, and cracks occurred. Figure 36 (a, b) shows the reason why the electrode is peeled off. A NiO100 anode was deposited on a substrate well, as under other conditions, but its structure changed severely in a cell operating environment. As NiO is reduced and oxygen is removed, voids are created, and Ni is separately agglomerated into clusters with a width of

several microns. As a result, the adhesion to the support was lowered and the anode was easily separated from substrate with upper electrolyte.

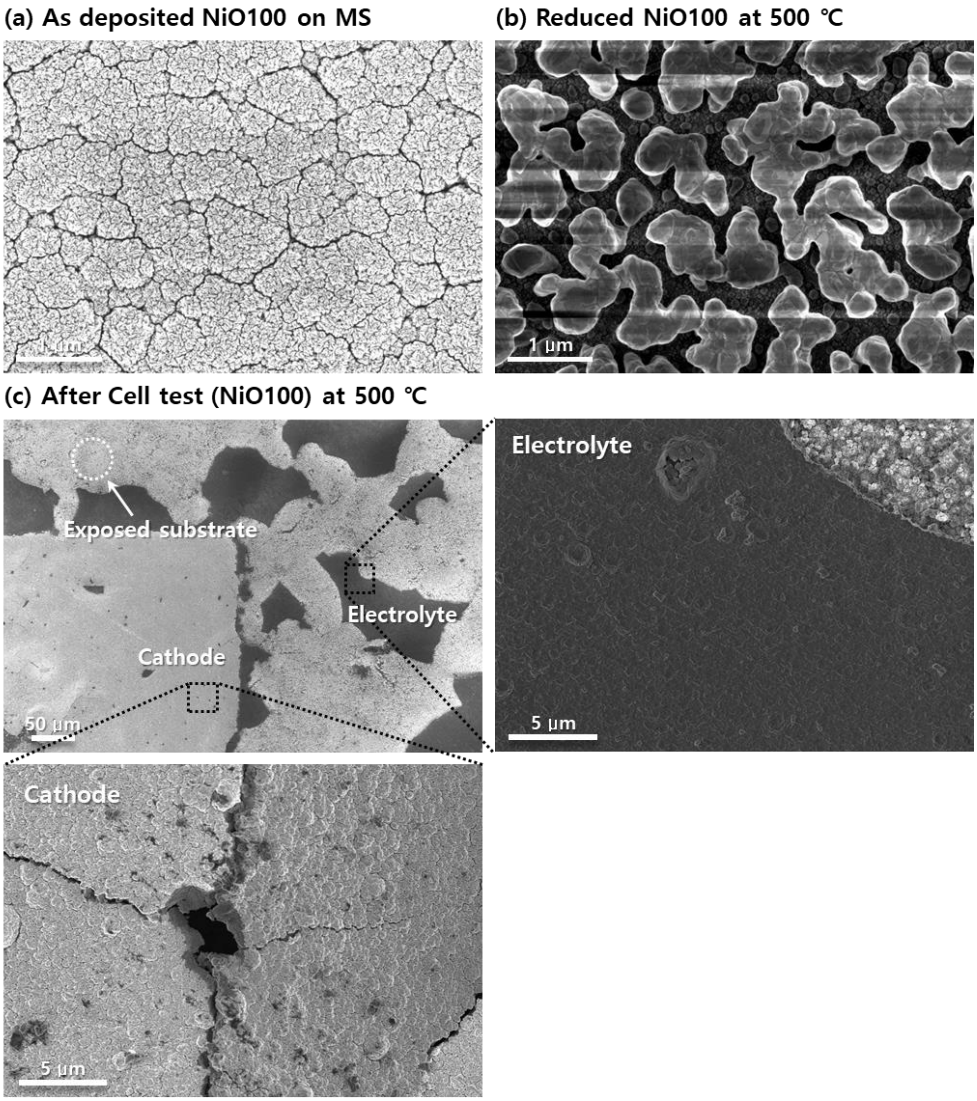

Figure 36. Surface SEM images of NiO100 anode (a), 500 ℃ reduced NiO100 (b), and delaminated surface after cell test (c)

EIS was performed to in-depth analysis of the cause of the difference in

electrochemical performance under each anode condition. In addition, OCV and 0.6 V were applied as bias voltages. Figure 37 shows the Nyquist plot and equivalent circuit of 3 composite anodes. For NiO50/GDC75, NiO50/GDC50, and NiO75/GDC50, respectively, the ohmic resistance, the x-axis intercept in the high frequency region, were 0.268 $\Omega \cdot cm^2$, 0.259 $\Omega \cdot cm^2$, and 0.292 $\Omega \cdot cm^2$. In the two conditions in which the nickel ratio was low, the ohmic resistance was almost the same, and in the condition in which the nickel ratio was high, the ohmic resistance slightly increased. This is because, in the process of reducing the anode, the more the nickel content, the more pores are created, which reduces the electron conduction path through the contact between the anode columns. Since a part of the surface of the multi-scale support is filled with GDC powder, the electrode created on it seems to be caused by the limitation in not being able to conduct electrons directly through the support. Therefore, when the Ni/GDC anode has a volume ratio of 1:1, it may be concluded that it has the proper porosity and conductivity. Under all measurement conditions, the polarization resistance rises in the order of NiO50/GDC50, NiO75/GDC50, and NiO50/GDC75. Since the difference between each sample is only the composition of the MIEC anode, it can be seen that the difference in TPB density according to the volume ratio of Ni/GDC causes the difference in faradaic loss. In terms of polarization resistance, it was confirmed that the TPB density was the highest when the Ni volume ratio was 49.5 %. Therefore, it was confirmed that the high performance of NiO50/GDC50 was due to the low ohmic resistance and polarization resistance.

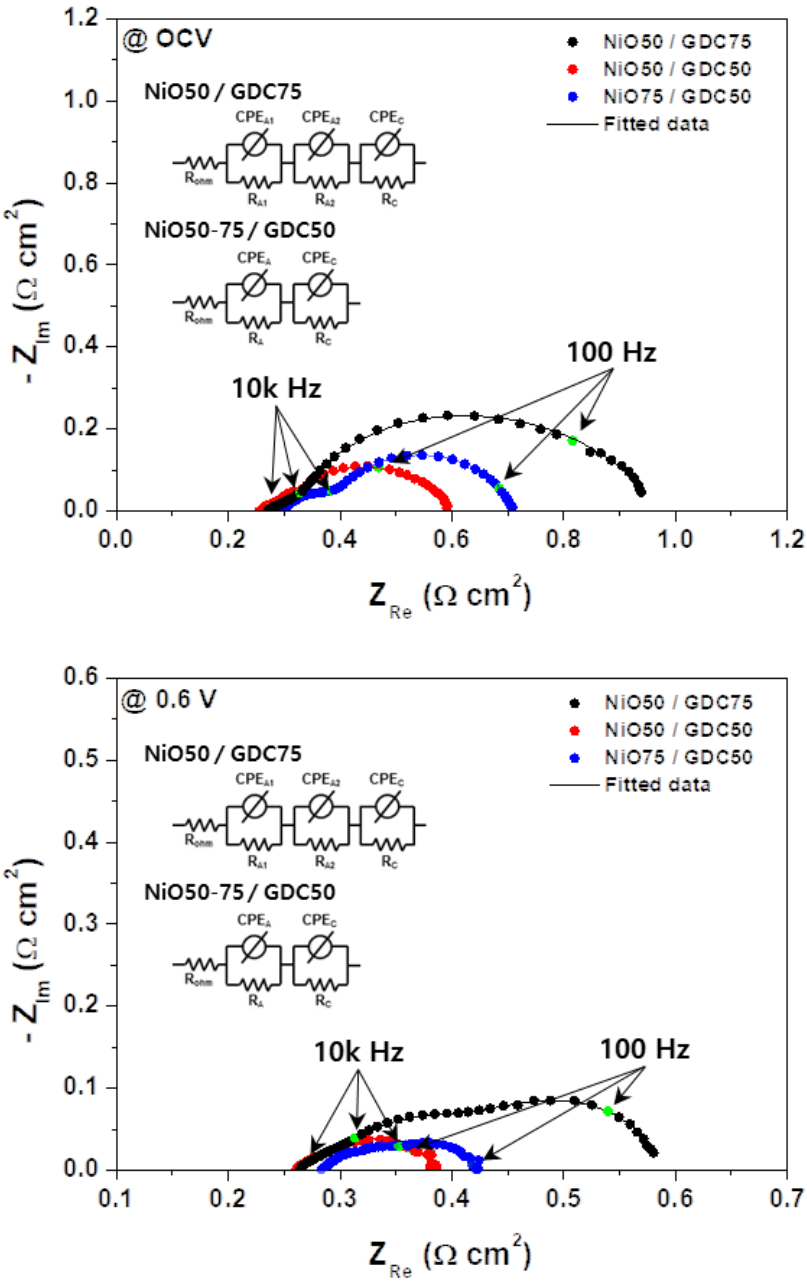

Figure 37. EIS spectra of MS SOFC with various volume ratio of NiO-GDC anode

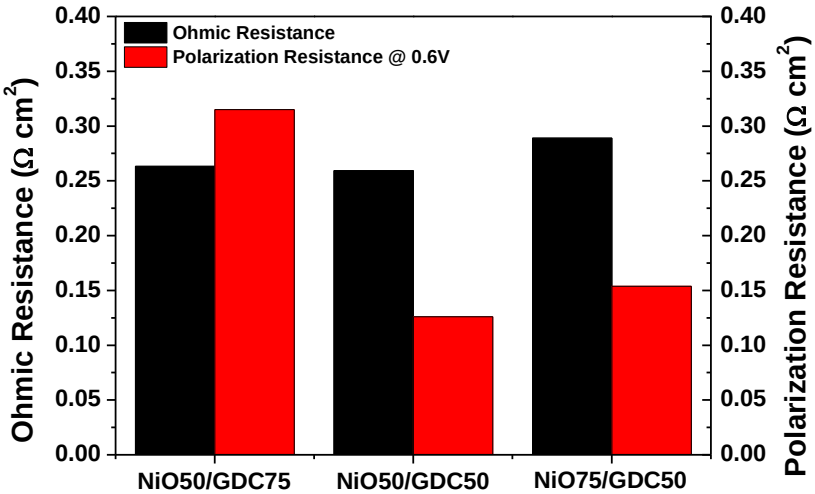

Figure 38. Graph of quantitative data of ohmic and polarization resistance in Nyquist plots (Fig.37)

4.3.3. Thermal Stability of Metal-Supported Thin-Film Solid Oxide Fuel Cells

Compared to anode-supported SOFCs, where the whole cell is composed of brittle ceramic, metal-supported SOFCs have an advantage in thermal stress resistance [39,44]. 5 times thermal cyclings were carried out to verify the thermal tolerance of developed metal-supported TF SOFC, and the results are presented in Figure 39. Unlike the initial test (10 °C/m of heating rate), the heating rate was set to 1 °C/m to reduce the thermal shock applied during the reduction of anodes. The peak power density measured for each thermal cycle showed a slight increase or decrease as the cycle progressed.

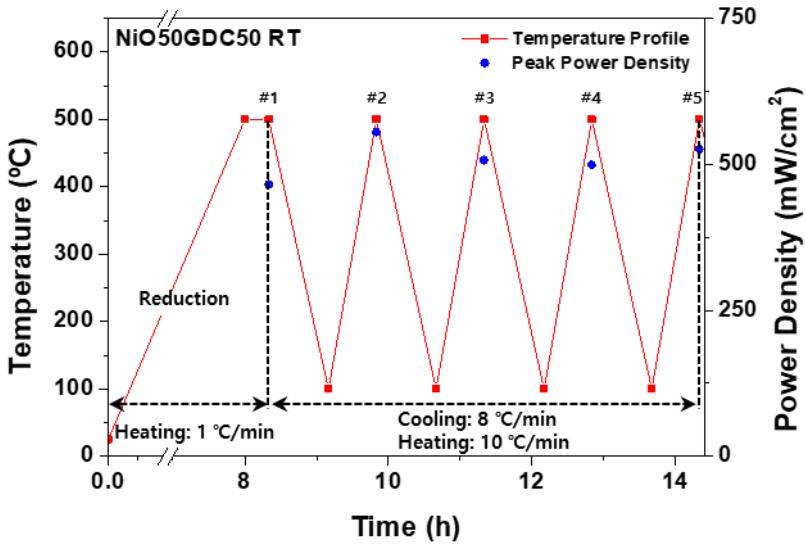

Figure 39. The temperature profile of the thermal cycle test and peak power density measurement

The peak power density was measured every cycle, and the measured performance in the range of about 500 to 550 mW/cm^2 was summarized in Table 13. In the first measurement after heating for 8 hours, a maximum power density of 466 mW/cm^2 was observed. There is a difference of about 33% from the maximum power density in the initial performance test (data of Figure 35.), which is presumed to be due to the highest TPB density because the nanostructure of the electrode is almost unchanged when measured after the rapid temperature increase. Other causes of electrochemical performance differences are further analyzed through EIS.

	Cycle 1	Cycle 2	Cycle 3	Cycle 4	Cycle 5
Peak Power Density (mW/cm^2)	466.0	554.8	506.8	499.0	525.9

Table 13. Results of peak power density measurements in each cycle

Figure 40 shows the EIS results measured at 0.6 V bias. Cycle 1's poor performance is caused by increased ohmic and polarization resistance compared to the results of other measurements. Generally, in the cell electrochemical performance experiment, the experiment is designed to minimize the effect of changes in external factors. However, the ceramic sealant and current collecting tip used in this experiment are not suitable elements for long-term or thermal cycling experiments. The tip has shown rapid degradation at an operating temperature of 500 °C. The ohmic resistance is lowered in the measurement results of the next cycle because the heating rate is fast, and the tip is exposed to high temperatures for less time, resulting in less degradation. Therefore, the high ohmic resistance in cycle 1 is due to deterioration of the tip in the reduction process for 8 hours. In the experiments excluding cycle1, the ohmic resistance and polarization resistance were almost similar. However, in terms of peak power density, there was a slight difference from the initial performance test results, and the results of the thermal cycle experiment fluctuated slightly. This is thought to be due to the limitations of the external factors constituting the experimental setup mentioned above. A ceramic sealant is used to seal a gas supplied to an anode and a cathode, and it seems that the sealing ability is decreased as the cycling experiment is conducted, so OCV is decreased, and thus the performance of the fuel cell is affected. Therefore, there does not appear to be any noticeable deterioration in the structure of the cell even after 5 thermal cycle experiments.

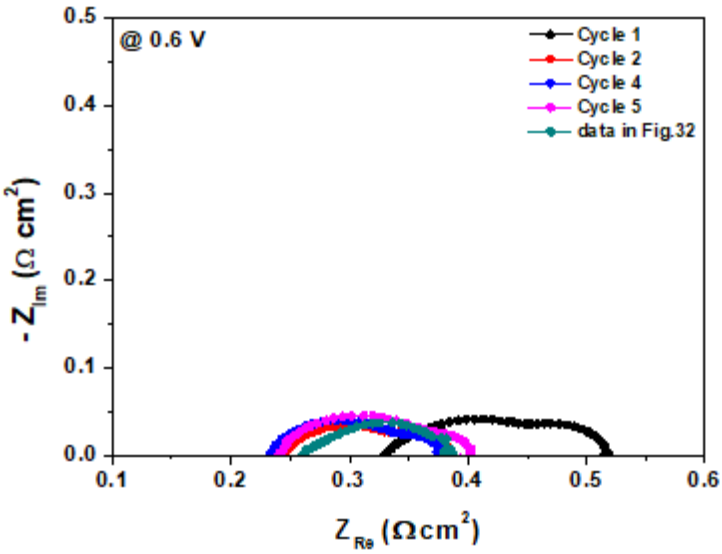

Figure 40. Nyquist plot of MS TF-SOFC obtained from each cycle at 0.6 V bias voltage

4.4. Conclusion

In this chapter, the performance change according to the composition ratio of the MIEC anode was confirmed. To verify crystallinity, composition ratio, and nanostructure, an 800 nm thick NiO/GDC electrode was fabricated on a Si wafer. The characterized anodes were deposited on a multiscale metal support to conduct an electrochemical performance test of TF-SOFC. There was a difference in the performance due to the electrode structure change in the operating environment and the TPB density. As a result, the NiO50/GDC50 electrode with a Ni volume ratio of 49.5% had the highest electrical conductivity and an increased reaction area, and

thereby showed the best performance (699.83 mW/cm^2). A thermal cycle experiment was conducted to confirm the thermal durability of the developed metal-supported TF-SOFC. Considering the deterioration of external factors of setup, it is judged that there is no noticeable degradation in cell performance even after 5 times of thermal cycle experiments.

Chapter 5. Achievements and Future Work

The ultimate goal of this research is to develop a technology that will enable SOFCs become more widely used. In order to secure high productivity and price competitiveness, we developed a low-temperature manufacturing method that can utilize metal support for SOFCs. Low-temperature fabrication methods include surface control processes that enable thin-film processes to be applied. By filling the pores of the metal support using nickel powder, the pore size was reduced, and nickel was intentionally aggregated to manufacture an electron-conductive network layer with mechanical rigidity. Additionally, the nano-sized GDC powder was vacuum filtered to have 50 nano-level pores. The process developed in this study was conducted below 700 ℃, which is lower than the recommended temperature of the metal support, and oxidation of the support could be suppressed. To the best of the author's knowledge, this is the first study to fabricate a metal-supported SOFC through a low-temperature process below 700 ℃.

A sputtering process scalable and widely used in industry was used to fabricate electrodes and electrolytes. Only one deposition process was used after surface treatment of the support to reduce the complexity of the process. This process simplification can effectively reduce the cost of fabricating the SOFC stack [88]. Electrolytes and electrodes with the required characteristics were manufactured through process variable control and optimized. Figure 41 shows the peak power density data of metal-supported SOFCs reported at operating temperatures between 400 ℃ and 600 ℃. The results of this study were superior to the results of many experiments reported operated at 600 ℃, and it is the highest value among the reported data operated at 500°C.

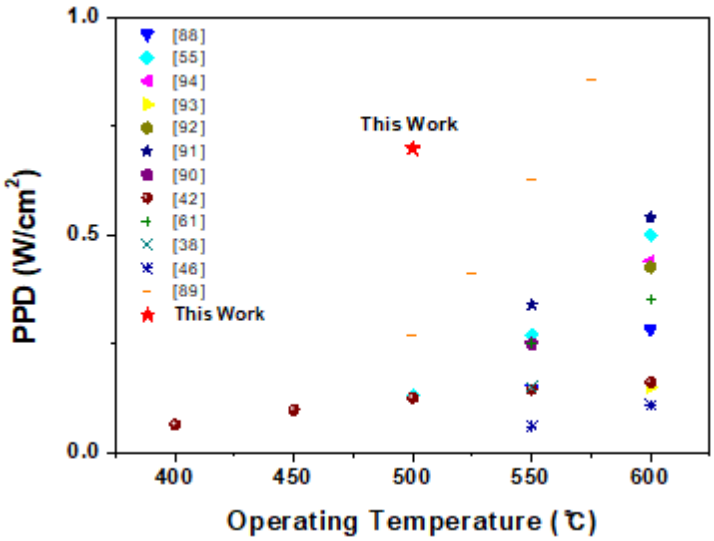

Figure 41. Peak power density data of metal-supported SOFCs reported in the operating temperature range of 400 to 650 °C [38,42,46,55,61,89–95]

Through this study, we have successfully developed a metal-supported thin film SOFC capable of low-temperature operation, but the durability of the cell has not yet been clearly verified. It is necessary to secure the reliability of high cell performance through thermal cycle experiments and long-term performance tests. In addition, there is a need to improve the roughness of the surface of the metal support. Although it has sufficient roughness to deposit a thin film, it is considered that additional improvement is needed to reduce the possibility of defects in the deposited electrode and electrolyte.

Bibliography

[1] A.M. Oliveira, R.R. Beswick, Y. Yan, A green hydrogen economy for a renewable energy society, Curr. Opin. Chem. Eng. 33 (2021) 100701. https://doi.org/10.1016/j.coche.2021.100701.

[2] R. O'Hayre, S.-W. Cha, W. Colella, F.B. Prinz, Fuel Cell Fundamentals, John Wiley & Sons, Inc, Hoboken, NJ, USA, 2016. https://doi.org/10.1002/9781119191766.

[3] Y. Zhang, J. Jiang, Y. An, L. Wu, H. Dou, J. Zhang, Y. Zhang, S. Wu, M. Dong, X. Zhang, Z. Guo, Sodium-ion capacitors: Materials, Mechanism, and Challenges, ChemSusChem. 13 (2020) 2522–2539. https://doi.org/10.1002/cssc.201903440.

[4] Y. Yang, Y. Zhang, M. Yan, A review on the preparation of thin-film YSZ electrolyte of SOFCs by magnetron sputtering technology, Sep. Purif. Technol. 298 (2022) 121627. https://doi.org/10.1016/j.seppur.2022.121627.

[5] A. Maheshwari, H.D. Wiemhöfer, Sr2+-Gd3+ co-doped CeO2: A cost-effective variant for IT-SOFC electrolytes, Ceram. Int. 41 (2015) 9122–9130. https://doi.org/10.1016/j.ceramint.2015.03.317.

[6] M. Sillassen, P. Eklund, M. Sridharan, N. Pryds, N. Bonanos, J. Bøttiger, Ionic conductivity and thermal stability of magnetron-sputtered nanocrystalline yttria-stabilized zirconia, J. Appl. Phys. 105 (2009). https://doi.org/10.1063/1.3130404.

[7] J.H. Shim, C.C. Chao, H. Huango, F.B. Prinz, Atomic layer deposition of yttria-stabilized zirconia for solid oxide fuel cells, Chem. Mater. 19 (2007) 3850–3854.

[8] D. Chiappini, A.L. Facci, L. Tribioli, S. Ubertini, SOFC management in distributed energy systems, J. Fuel Cell Sci. Technol. 8 (2011). https://doi.org/10.1115/1.4002907.

[9] M. Dewa, W. Yu, N. Dale, A.M. Hussain, M.G. Norton, S. Ha, Recent progress in integration of reforming catalyst on metal-supported SOFC for hydrocarbon and logistic fuels, Int. J. Hydrogen Energy. 46 (2021) 33523–33540. https://doi.org/10.1016/j.ijhydene.2021.07.177.

[10] C. Kwon, J. Son, J. Lee, H. Kim, H. Lee, K. Kim, High-Performance Micro-Solid Oxide Fuel Cells Fabricated on Nanoporous Anodic Aluminum Oxide Templates, Adv. Funct. Mater. (2011) 1154–1159. https://doi.org/10.1002/adfm.201002137.

[11] G.Y. Cho, W. Yu, Y.H. Lee, Y. Lee, W.H. Tanveer, Y. Kim, S. Lee, S.W. Cha, Effects of Nanoscale PEALD YSZ Interlayer for AAO Based Thin Film Solid Oxide Fuel Cells, Int. J. Precis. Eng. Manuf. - Green Technol. 7 (2020) 423–430. https://doi.org/10.1007/s40684-019-00082-9.

[12] I. Chang, S. Ji, J. Park, M.H. Lee, S.W. Cha, Ultrathin YSZ coating on Pt cathode for high thermal stability and enhanced oxygen reduction reaction activity, Adv. Energy Mater. 5 (2015) 1–7. https://doi.org/10.1002/aenm.201402251.

[13] W. Yu, Y. Lim, S. Lee, A. Pandiyan, G.Y. Cho, S.W. Cha, Low-temperature, high-performance thin-film solid oxide fuel cells with tailored

nano-column structures of a sputtered Ni anode, J. Mater. Chem. A. 8 (2020) 21668–21679. https://doi.org/10.1039/d0ta06255c.
[14] J.W. Shin, S. Oh, S. Lee, J. Yu, J. Park, D. Go, B.C. Yang, H.J. Kim, J. An, Ultrathin Atomic Layer-Deposited CeO 2 Overlayer for High- Performance Fuel Cell Electrodes, (2019). https://doi.org/10.1021/acsami.9b10572.
[15] S. Ji, G.Y. Cho, W. Yu, P.C. Su, M.H. Lee, S.W. Cha, Plasma-enhanced atomic layer deposition of nanoscale yttria-stabilized zirconia electrolyte for solid oxide fuel cells with porous substrate, ACS Appl. Mater. Interfaces. 7 (2015) 2998–3002. https://doi.org/10.1021/am508710s.
[16] S. Lee, G.Y. Cho, T. Park, Y.H. Lee, W. Yu, Y. Lee, I. Chang, S.W. Cha, A nanoporous substrate-based low temperature solid oxide fuel cell using a thin film Ni anode, Thin Solid Films. 666 (2018) 177–181. https://doi.org/10.1016/j.tsf.2018.09.039.
[17] Y.H. Lee, H. Ren, E.A. Wu, E.E. Fullerton, Y.S. Meng, N.Q. Minh, All-Sputtered, Superior Power Density Thin-Film Solid Oxide Fuel Cells with a Novel Nanofibrous Ceramic Cathode, Nano Lett. 20 (2020) 2943–2949. https://doi.org/10.1021/acs.nanolett.9b02344.
[18] S. Hong, J. Bae, B. Koo, Y.B. Kim, High-performance ultra-thin film solid oxide fuel cell using anodized-aluminum-oxide supporting structure, Electrochem. Commun. 47 (2014) 1–4. https://doi.org/10.1016/j.elecom.2014.07.008.
[19] Y. Lim, S. Hong, J. Bae, H. Yang, Y.B. Kim, Influence of deposition temperature on the microstructure of thin-film electrolyte for SOFCs with a nanoporous AAO support structure, Int. J. Hydrogen Energy. 42 (2017) 10199–10207. https://doi.org/10.1016/j.ijhydene.2017.03.148.
[20] G.Y. Cho, Y.H. Lee, W. Yu, J. An, S.W. Cha, Optimization of Y2O3 dopant concentration of yttria stabilized zirconia thin film electrolyte prepared by plasma enhanced atomic layer deposition for high performance thin film solid oxide fuel cells, Energy. 173 (2019) 436–442. https://doi.org/10.1016/j.energy.2019.01.124.
[21] I.W. Choi, W. Yu, M.S. Lee, S. Ryu, Y.H. Lee, S.W. Cha, G.Y. Cho, Tailoring 3D structured nanofibrous nickel/gadolinium-doped ceria anodes for high-performance thin-film solid oxide fuel cells, J. Power Sources. 531 (2022) 231320. https://doi.org/10.1016/j.jpowsour.2022.231320.
[22] Z. Fan, J. An, A. Iancu, F.B. Prinz, Thickness effects of yttria-doped ceria interlayers on solid oxide fuel cells, J. Power Sources. 218 (2012) 187–191. https://doi.org/10.1016/j.jpowsour.2012.06.103.
[23] H. Huang, M. Nakamura, P. Su, R. Fasching, Y. Saito, F.B. Prinz, High-Performance Ultrathin Solid Oxide Fuel Cells for Low-Temperature Operation, J. Electrochem. Soc. 154 (2007) B20. https://doi.org/10.1149/1.2372592.
[24] Y.B. Kim, T.M. Gür, S. Kang, H.J. Jung, R. Sinclair, F.B. Prinz, Crater patterned 3-D proton conducting ceramic fuel cell architecture with ultra thin Y:BaZrO3 electrolyte, Electrochem. Commun. 13 (2011) 403–406. https://doi.org/10.1016/j.elecom.2011.02.004.
[25] P. Su, C. Chao, J.H. Shim, R. Fasching, F.B. Prinz, Solid Oxide Fuel Cell with Corrugated Thin Film Electrolyte 2008, Nano Lett. 8 (2008) 2289–2292.
[26] K. Kerman, B.K. Lai, S. Ramanathan, Free standing oxide alloy electrolytes

for low temperature thin film solid oxide fuel cells, J. Power Sources. 202 (2012) 120–125. https://doi.org/10.1016/j.jpowsour.2011.11.062.
[27] J.D. Baek, K.Y. Liu, P.C. Su, A functional micro-solid oxide fuel cell with a 10 nm-thick freestanding electrolyte, J. Mater. Chem. A. 5 (2017) 18414–18419. https://doi.org/10.1039/c7ta05245f.
[28] Y. Takagi, K. Kerman, C. Ko, S. Ramanathan, Operational characteristics of thin film solid oxide fuel cells with ruthenium anode in natural gas, J. Power Sources. 243 (2013) 1–9. https://doi.org/10.1016/j.jpowsour.2013.06.002.
[29] Y. Li, S. Wang, P.C. Su, Proton-conducting Micro-solid Oxide Fuel Cells with Improved Cathode Reactions by a Nanoscale Thin Film Gadolinium-doped Ceria Interlayer, Sci. Rep. 6 (2016) 1–9. https://doi.org/10.1038/srep22369.
[30] J. An, Y.B. Kim, J. Park, T.M. Gür, F.B. Prinz, Three-dimensional nanostructured bilayer solid oxide fuel cell with 1.3 W/cm2 at 450 C, Nano Lett. 13 (2013) 4551–4555. https://doi.org/10.1021/nl402661p.
[31] P.C. Su, F.B. Prinz, Nanoscale membrane electrolyte array for solid oxide fuel cells, Electrochem. Commun. 16 (2012) 77–79. https://doi.org/10.1016/j.elecom.2011.12.002.
[32] J.D. Baek, C.C. Yu, P.C. Su, A Silicon-Based Nanothin Film Solid Oxide Fuel Cell Array with Edge Reinforced Support for Enhanced Thermal Mechanical Stability, Nano Lett. 16 (2016) 2413–2417. https://doi.org/10.1021/acs.nanolett.5b05221.
[33] C.C. Chao, C.M. Hsu, Y. Cui, F.B. Prinz, Improved solid oxide fuel cell performance with nanostructured electrolytes, ACS Nano. 5 (2011) 5692–5696. https://doi.org/10.1021/nn201354p.
[34] J.H. Shim, C.C. Chao, H. Huango, F.B. Prinz, Atomic layer deposition of yttria-stabilized zirconia for solid oxide fuel cells, Chem. Mater. 19 (2007) 3850–3854. https://doi.org/10.1021/cm070913t.
[35] C. Ko, K. Kerman, S. Ramanathan, Ultra-thin film solid oxide fuel cells utilizing un-doped nanostructured zirconia electrolytes, J. Power Sources. 213 (2012) 343–349. https://doi.org/10.1016/j.jpowsour.2012.04.034.
[36] Y. Lim, S. Hong, J. Bae, H. Yang, Y.B. Kim, Influence of deposition temperature on the microstructure of thin-film electrolyte for SOFCs with a nanoporous AAO support structure, Int. J. Hydrogen Energy. 42 (2017) 10199–10207. https://doi.org/10.1016/j.ijhydene.2017.03.148.
[37] N. Yamamoto, D.J. Quinn, N. Wicks, J.L. Hertz, J. Cui, H.L. Tuller, B.L. Wardle, Nonlinear thermomechanical design of microfabricated thin plate devices in the post-buckling regime, J. Micromechanics Microengineering. 20 (2010). https://doi.org/10.1088/0960-1317/20/3/035027.
[38] A. Bieberle-Hütter, D. Beckel, A. Infortuna, U.P. Muecke, J.L.M. Rupp, L.J. Gauckler, S. Rey-Mermet, P. Muralt, N.R. Bieri, N. Hotz, M.J. Stutz, D. Poulikakos, P. Heeb, P. Müller, A. Bernard, R. Gmür, T. Hocker, A micro-solid oxide fuel cell system as battery replacement, J. Power Sources. 177 (2008) 123–130. https://doi.org/10.1016/j.jpowsour.2007.10.092.
[39] M.C. Tucker, Progress in metal-supported solid oxide fuel cells: A review, J. Power Sources. 195 (2010) 4570–4582. https://doi.org/10.1016/j.jpowsour.2010.02.035.
[40] V.V. Krishnan, Recent developments in metal-supported solid oxide fuel

cells, Wiley Interdiscip. Rev. Energy Environ. 6 (2017). https://doi.org/10.1002/wene.246.
[41] Y. Zhou, X. Ye, J. Li, Z. Zhan, S. Wang, Metal-Supported Solid Oxide Fuel Cells with a Simple Structure, J. Electrochem. Soc. 161 (2014) F332–F336. https://doi.org/10.1149/2.085403jes.
[42] S. (Rob) Hui, D. Yang, Z. Wang, S. Yick, C. Decès-Petit, W. Qu, A. Tuck, R. Maric, D. Ghosh, Metal-supported solid oxide fuel cell operated at 400-600 °C, J. Power Sources. 167 (2007) 336–339. https://doi.org/10.1016/j.jpowsour.2007.02.070.
[43] P. Satardekar, D. Montinaro, M.Z. Naik, V.M. Sglavo, Production of metal-supported solid oxide fuel cells by co-sintering route, Mater. Today Proc. 63 (2022) 76–84. https://doi.org/10.1016/j.matpr.2022.02.327.
[44] E. Dogdibegovic, Y. Cheng, F. Shen, R. Wang, B. Hu, M.C. Tucker, Scaleup and manufacturability of symmetric-structured metal-supported solid oxide fuel cells, J. Power Sources. 489 (2021) 229439. https://doi.org/10.1016/j.jpowsour.2020.229439.
[45] D. Udomsilp, J. Rechberger, R. Neubauer, C. Bischof, F. Thaler, W. Schafbauer, N.H. Menzler, L.G.J. de Haart, A. Nenning, A.K. Opitz, O. Guillon, M. Bram, Metal-Supported Solid Oxide Fuel Cells with Exceptionally High Power Density for Range Extender Systems, Cell Reports Phys. Sci. 1 (2020). https://doi.org/10.1016/j.xcrp.2020.100072.
[46] A.M. Dayaghi, K.J. Kim, S. Kim, J. Park, S.J. Kim, B.H. Park, G.M. Choi, Stainless steel-supported solid oxide fuel cell with La0.2Sr0.8Ti0.9Ni0.1O3−Δ/yttria-stabilized zirconia composite anode, J. Power Sources. 324 (2016) 288–293. https://doi.org/10.1016/j.jpowsour.2016.05.076.
[47] Y. Zhou, X. Meng, X. Ye, J. Li, S. Wang, Z. Zhan, Metal-supported solid oxide fuel cells with impregnated SrFe 0.75Mo0.25O3 cathodes, J. Power Sources. 247 (2014) 556–561. https://doi.org/10.1016/j.jpowsour.2013.08.134.
[48] A.M. Dayaghi, K.J. Kim, S.J. Kim, S. Kim, H. Bae, G.M. Choi, Thermal cycling and electrochemical characteristics of solid oxide fuel cell supported on stainless steel with a new 3-phase composite anode, J. Power Sources. 354 (2017) 74–84. https://doi.org/10.1016/j.jpowsour.2017.04.022.
[49] H.J. Cho, K.J. Kim, Y.M. Park, G.M. Choi, Flexible solid oxide fuel cells supported on thin and porous metal, Int. J. Hydrogen Energy. 41 (2016) 9577–9584. https://doi.org/10.1016/j.ijhydene.2016.04.040.
[50] K.J. Kim, B.H. Park, S.J. Kim, Y. Lee, H. Bae, G.M. Choi, Micro solid oxide fuel cell fabricated on porous stainless steel: A new strategy for enhanced thermal cycling ability, Sci. Rep. 6 (2016) 1–8. https://doi.org/10.1038/srep22443.
[51] H.J. Cho, Y.M. Park, G.M. Choi, Enhanced power density of metal-supported solid oxide fuel cell with a two-step firing process, Solid State Ionics. 192 (2011) 519–522. https://doi.org/10.1016/j.ssi.2010.03.023.
[52] N. Hosseini, M.H. Abbasi, F. Karimzadeh, G.M. Choi, Development of Cu1.3Mn1.7O4 spinel coating on ferritic stainless steel for solid oxide fuel cell interconnects, J. Power Sources. 273 (2015) 1073–1083. https://doi.org/10.1016/j.jpowsour.2014.10.017.
[53] Y. Lee, Y.M. Park, G.M. Choi, Micro-solid oxide fuel cell supported on a

porous metallic Ni/stainless-steel bi-layer, J. Power Sources. 249 (2014) 79–83. https://doi.org/10.1016/j.jpowsour.2013.10.082.
[54] K.J. Kim, S.J. Kim, G.M. Choi, Y0.08Sr0.88TiO3-CeO2 composite as a diffusion barrier layer for stainless-steel supported solid oxide fuel cell, J. Power Sources. 307 (2016) 385–390. https://doi.org/10.1016/j.jpowsour.2015.12.130.
[55] R. Hui, J.O. Berghaus, C. Decès-Petit, W. Qu, S. Yick, J.G. Legoux, C. Moreau, High performance metal-supported solid oxide fuel cells fabricated by thermal spray, J. Power Sources. 191 (2009) 371–376. https://doi.org/10.1016/j.jpowsour.2009.02.067.
[56] C. Mendonça, A. Ferreira, D.M.F. Santos, Towards the Commercialization of Solid Oxide Fuel Cells: Recent Advances in Materials and Integration Strategies, Fuels. 2 (2021) 393–419. https://doi.org/10.3390/fuels2040023.
[57] R.T. Leah, A. Bone, A. Selcuk, D. Corcoran, M. Lankin, Z. Dehaney-Steven, P. Whalen, Development of Highly Robust, Volume-Manufacturable Metal-Supported SOFCs for Operation below 600°, ECS Meet. Abstr. MA2011-01 (2011) 749–749. https://doi.org/10.1149/ma2011-01/12/749.
[58] R.T. Leah, A. Bone, M. Lankin, A. Selcuk, M. Rahman, A. Clare, L. Rees, S. Phillip, S. Mukerjee, M. Selby, Ceres Power Steel Cell Technology: Rapid Progress Towards a Truly Commercially Viable SOFC, ECS Meet. Abstr. MA2015-03 (2015) 7–7. https://doi.org/10.1149/ma2015-03/1/7.
[59] P. Bance, N.P. Brandon, B. Girvan, P. Holbeche, S.O. Dea, B.C.H. Steele, Spinning-out a fuel cell company from a UK University — 2 years of progress at Ceres Power, 131 (2004) 86–90. https://doi.org/10.1016/j.jpowsour.2003.11.077.
[60] E.C.S. Transactions, Commercialization of the Ceres Power SteelCell ® Technology : Latest Update, (2021).
[61] R.T. Leah, N.P. Brandon, P. Aguiar, Modelling of cells, stacks and systems based around metal-supported planar IT-SOFC cells with CGO electrolytes operating at 500-600°C, J. Power Sources. 145 (2005) 336–352. https://doi.org/10.1016/j.jpowsour.2004.12.067.
[62] Z. Zakaria, Z. Awang Mat, S.H. Abu Hassan, Y. Boon Kar, A review of solid oxide fuel cell component fabrication methods toward lowering temperature, Int. J. Energy Res. 44 (2020) 594–611. https://doi.org/10.1002/er.4907.
[63] J.A. Thornton, Influence of substrate temperature and deposition rate on structure of thick sputtered Cu coatings, J. Vac. Sci. Technol. 12 (1975) 830.
[64] M. Han, X. Tang, H. Yin, S. Peng, Fabrication, microstructure and properties of a YSZ electrolyte for SOFCs, J. Power Sources. 165 (2007) 757–763. https://doi.org/10.1016/j.jpowsour.2006.11.054.
[65] D.R. Ou, T. Mori, F. Ye, M. Takahashi, J. Zou, J. Drennan, Microstructures and electrolytic properties of yttrium-doped ceria electrolytes: Dopant concentration and grain size dependences, Acta Mater. 54 (2006) 3737–3746. https://doi.org/10.1016/j.actamat.2006.04.003.
[66] S. (Rob) Hui, J. Roller, S. Yick, X. Zhang, C. Decès-Petit, Y. Xie, R. Maric, D. Ghosh, A brief review of the ionic conductivity enhancement for selected oxide electrolytes, J. Power Sources. 172 (2007) 493–502.

https://doi.org/10.1016/j.jpowsour.2007.07.071.
[67] C. Peters, A. Weber, B. Butz, D. Gerthsen, E. Ivers-Tiffée, Grain-size effects in YSZ thin-film electrolytes, J. Am. Ceram. Soc. 92 (2009) 2017–2024. https://doi.org/10.1111/j.1551-2916.2009.03157.x.
[68] N.J. Kidner, N.H. Perry, T.O. Mason, E.J. Garboczi, The brick layer model revisited: Introducing the nano-grain composite model, J. Am. Ceram. Soc. 91 (2008) 1733–1746. https://doi.org/10.1111/j.1551-2916.2008.02445.x.
[69] Y. Endo, A. Dempoh, T. Terai, A. Suzuki, Grain Size Effect on Conductivity of LSGM Thin Film Electrolyte for Solid Oxide Fuel Cell, ECS Meet. Abstr. MA2015-03 (2015) 329–329. https://doi.org/10.1149/ma2015-03/1/329.
[70] X.D. Zhou, W. Huebner, I. Kosacki, H.U. Anderson, Microstructure and grain-boundary effect on electrical properties of gadolinium-doped ceria, J. Am. Ceram. Soc. 85 (2002) 1757–1762. https://doi.org/10.1111/j.1151-2916.2002.tb00349.x.
[71] X. Guo, Z. Zhang, Grain size dependent grain boundary defect structure: Case of doped zirconia, Acta Mater. 51 (2003) 2539–2547. https://doi.org/10.1016/S1359-6454(03)00052-1.
[72] Y.B. Kim, J.S. Park, T.M. Gür, F.B. Prinz, Oxygen activation over engineered surface grains on YDC/YSZ interlayered composite electrolyte for LT-SOFC, J. Power Sources. 196 (2011) 10550–10555. https://doi.org/10.1016/j.jpowsour.2011.08.075.
[73] X. Guo, R. Waser, Electrical properties of the grain boundaries of oxygen ion conductors: Acceptor-doped zirconia and ceria, Prog. Mater. Sci. 51 (2006) 151–210. https://doi.org/10.1016/j.pmatsci.2005.07.001.
[74] J.S. Park, Y.B. Kim, J. An, F.B. Prinz, Oxygen diffusion across the grain boundary in bicrystal yttria stabilized zirconia, Solid State Commun. 152 (2012) 2169–2171. https://doi.org/10.1016/j.ssc.2012.09.019.
[75] F. Han, R. Mücke, T. Van Gestel, A. Leonide, N.H. Menzler, H.P. Buchkremer, D. Stöver, Novel high-performance solid oxide fuel cells with bulk ionic conductance dominated thin-film electrolytes, J. Power Sources. 218 (2012) 157–162. https://doi.org/10.1016/j.jpowsour.2012.06.087.
[76] J. Zhang, C. Lenser, N.H. Menzler, O. Guillon, Comparison of solid oxide fuel cell (SOFC) electrolyte materials for operation at 500 °C, Solid State Ionics. 344 (2020) 115138. https://doi.org/10.1016/j.ssi.2019.115138.
[77] W. Lee, H.J. Jung, M.H. Lee, Y.B. Kim, J.S. Park, R. Sinclair, F.B. Prinz, Oxygen surface exchange at grain boundaries of oxide ion conductors, Adv. Funct. Mater. 22 (2012) 965–971. https://doi.org/10.1002/adfm.201101996.
[78] W. Jeong, W. Yu, M.S. Lee, S.J. Bai, G.Y. Cho, S.W. Cha, Ultrathin sputtered platinum–gadolinium doped ceria cathodic interlayer for enhanced performance of low temperature solid oxide fuel cells, Int. J. Hydrogen Energy. 45 (2020) 32442–32448. https://doi.org/10.1016/j.ijhydene.2020.08.239.
[79] S.S. Shin, J.H. Kim, K.T. Bae, K.-T. Lee, S.M. Kim, J.-W. Son, M. Choi, H. Kim, Multiscale structured low-temperature solid oxide fuel cells with 13 W power at 500 °C, Energy Environ. Sci. 13 (2020) 3459–3468. https://doi.org/10.1039/d0ee00870b.
[80] Y. Liu, Z. Shao, T. Mori, S.P. Jiang, Development of nickel based cermet anode materials in solid oxide fuel cells – Now and future, Mater. Reports

Energy. 1 (2021) 100003. https://doi.org/10.1016/j.matre.2020.11.002.
[81] J.R. Wilson, S.A. Barnett, Solid oxide fuel cell Ni-YSZ anodes: Effect of composition on microstructure and performance, Electrochem. Solid-State Lett. 11 (2008) 11–16. https://doi.org/10.1149/1.2960528.
[82] F. Zhao, A. V. Virkar, Dependence of polarization in anode-supported solid oxide fuel cells on various cell parameters, J. Power Sources. 141 (2005) 79–95. https://doi.org/10.1016/j.jpowsour.2004.08.057.
[83] J. Kim, A. V. Virkar, K. Fung, K. Mehta, S.C. Singhal, Polarization Effects in Intermediate Temperature, Anode-Supported Solid Oxide Fuel Cells, J. Electrochem. Soc. 146 (1999) 69–78. https://doi.org/10.1149/1.1391566.
[84] W. Huebner, Solid Oxide Fuel Cell Performance Studie[1] W. Huebner, Solid Oxide Fuel Cell Performance Studies: Anode Development, ECS Proc. Vol. 1999–19 (1999) 503–512. https://doi.org/10.1149/199919.0503pv.s: Anode Development, ECS Proc. Vol. 1999–19 (1999) 503–512. https://doi.org/10.1149/199919.0503pv.
[85] Y. Lim, H. Lee, S. Hong, Y.B. Kim, Co-sputtered nanocomposite nickel cermet anode for high-performance low-temperature solid oxide fuel cells, J. Power Sources. 412 (2019) 160–169. https://doi.org/10.1016/j.jpowsour.2018.11.025.
[86] M. SAYER, K. SREENIVAS, Ceramic Thin Films: Fabrication and Applications, Science (80-.). 247 (1990) 1056–1060.
[87] T. Kim, H.J. Kim, D. Go, J.W. Shin, B.C. Yang, G.Y. Cho, T.M. Gür, J. An, Reactive sputtered Ni-SDC cermet alloy anode for low-temperature solid oxide fuel cell, J. Alloys Compd. 924 (2022) 166332. https://doi.org/10.1016/j.jallcom.2022.166332.
[88] L.A. Chick, G.A. Whyatt, M.R. Weimer, D.W. Gotthold, Cost Study for Manufacturing of Solid Oxide Fuel Cell Power Systems MR Weimar LA Chick DW Gotthold GA Whyatt, (2013) 50. https://www.pnnl.gov/main/publications/external/technical_reports/PNNL-22732.pdf.
[89] K. Lee, J. Kang, J. Lee, S. Lee, J. Bae, Evaluation of metal-supported solid oxide fuel cells (MS-SOFCs) fabricated at low temperature (～1,000 °C) using wet chemical coating processes and a catalyst wet impregnation method, Int. J. Hydrogen Energy. 43 (2018) 3786–3796. https://doi.org/10.1016/j.ijhydene.2018.01.027.
[90] M.C. Tucker, Development of High Power Density Metal-Supported Solid Oxide Fuel Cells, Energy Technol. 5 (2017) 2175–2181. https://doi.org/10.1002/ente.201700242.
[91] Y. peng Wang, J. tao Gao, W. Chen, C. xin Li, S. lin Zhang, G. jun Yang, C. jiu Li, Development of ScSZ Electrolyte by Very Low Pressure Plasma Spraying for High-Performance Metal-Supported SOFCs, J. Therm. Spray Technol. 29 (2020) 223–231. https://doi.org/10.1007/s11666-019-00970-1.
[92] Y. Zhou, H. Wu, T. Luo, J. Wang, Y. Shi, C. Xia, S. Wang, Z. Zhan, A nanostructured architecture for reduced-temperature solid oxide fuel cells, Adv. Energy Mater. 5 (2015). https://doi.org/10.1002/aenm.201500375.
[93] N.P. Brandon, A. Blake, D. Corcoran, D. Cumming, A. Duckett, K. El-Koury, D. Haigh, C. Kidd, R. Leah, G. Lewis, C. Matthews, N. Maynard, N. Oishi, T. McColm, R. Trezona, A. Selcuk, M. Schmidt, L. Verdugo, Development of metal supported solid oxide fuel cells for operation at 500-

600 °C, J. Fuel Cell Sci. Technol. 1 (2004) 61–65. https://doi.org/10.1115/1.1794709.

[94] H.J. Choi, T.W. Kim, Y.H. Na, D.W. Seo, S.K. Woo, J.Y. Huh, S.D. Kim, Enhanced electrochemical performance of metal-supported solid oxide fuel cells via an inner coating of Gd0.1Ce0.9O2-Δ nanosol in the porous NiFe-metal support, J. Power Sources. 406 (2018) 81–87. https://doi.org/10.1016/j.jpowsour.2018.10.044.

[95] C.S. Hwang, C.H. Tsai, T.J. Hwang, C.L. Chang, S.F. Yang, J.K. Lin, Novel Metal Substrates for High Power Metal-supported Solid Oxide Fuel Cells, Fuel Cells. 16 (2016) 244–251. https://doi.org/10.1002/fuce.201500216.

국문 초록

지구온난화 방지를 위한 수십년간의 전 세계적인 노력에도 불구하고 지구 평균온도는 계속해서 상승하고 있다. 지속적으로 증가하는 이산화탄소 배출량을 제한하기 위해서는 이를 대체할 수 있는 청정 에너지의 개발이 필수적이며 이를 대체할 수 있는 연료전지에 대한 관심이 증가하고 있다. 그 중에서도 고체산화물 연료전지는 높은 효율로 인하여 화석연료를 대체할 수 있는 가장 유력한 후보로 각광받고 있다. 고체산화물 연료전지는 높은 작동온도 (800-1000℃)로 인해 높은 효율뿐만 아니라 다양한 종류의 연료가 사용 가능하며, 귀금속 촉매를 사용하지 않아도 되는 장점을 가진다. 하지만 높은 온도로 인해 시스템이 쉽게 열화 되고 사용할 수 있는 물질이 제한된다. 이러한 문제들로 인해 상용화에 어려움을 겪고 있다. 따라서 고체산화물 연료전지의 기술 수준을 높이기 위해서는 저온 영역에서도 높은 전기화학 성능을 갖는 셀의 개발이 필요하다. 저온 작동 조건에서는 고온 작동대비 오믹 손실과 분극 저항이 모두 증가한다. 이러한 손실을 줄여야만 요구되는 성능을 얻을 수 있다. 오믹 손실을 줄이기 위한 방법으로 박막 전해질을 사용하는 방법이 있다. 수십 마이크로미터 수준의 두께로 제작되는 고온 소결 공정과는 달리 물리기상증착법과 화학기상증착법을 통해 박막의 전극과 전해질을 제작할 수 있으며 이를 통해 오믹 저항을 상당히 줄일 수 있다. 하지만 박막 공정을 적용하기 위해서는 지지체의 기공 크기가 수 마이크로 미만이어야 하고 표면 또한 균일하여야 한다. 이러한 제한 때문에 상용화에 유리한 금속지지체에는 박막 공정을 적용할 수 없었다. 따라서 본 연구에서는 금속지지체의 표면을 제어하여 박막 공정을 적용 가능하도록 하며 고체산화물 연료전지 제작 과정 중 금속지지체의 산화를 최소화하기 위한 저온 제작 공정을 개발하였다.

쉽고 간단한 공정을 활용하여 금속 지지체의 표면을 조절하였다. 진공여과 공정을 사용하여 금속 지지체의 기공을 줄였다. 크기가 다른 니켈 파우더를

순차적으로 금속지지체의 기공안에 채워넣었고 최종적으로 세라믹 GDC 파우더를 사용하여 표면 기공과 거칠기를 줄였다. 진공여과 공정 후 700도씨의 수소환경에서 소결함으로써 금속지지체의 열화 없이 단단한 니켈 네트워크를 형성하였다. 이를 통해 수십나노미터 수준 크기의 기공을 갖는 표면을 제작하였으며 박막공정의 적용이 가능함을 검증하였다. 내구성 검증을 위해 500도씨에서 12시간의 작동후에도 표면 구조에 변함이 없는 것이 확인되었다.

개발된 금속지지체가 갖는 기공의 크기는 충분히 작지만 랜덤하게 분포하여있기 때문에 치밀한 전해질 제작을 통한 OCV 확보가 중요하다. 스퍼터링을 통해 전해질을 제작할 경우 공정의 특성에서 발생하는 핀홀이 전해질의 결함으로 작용할 수 있다. 따라서 이러한 결함을 줄이고 전해질의 이온 전도성을 높일 수 있는 공정을 개발하였다. 전해질의 증착 온도를 조절하여 전해질 그레인의 크기를 조절하였고 그에 따른 특성 변화를 관찰하였다. 전해질의 그레인바운더리는 그레인 중심부보다 이온전도도가 1-2 오더 낮은 특징이 있는데 그레인 크기를 키움으로써 그레인바운더리 밀도를 낮추었다. YSZ와 GDC 전해질 제작에 고온 증착공정을 적용하여 오믹 저항을 감소시켰다. 최종적으로 YSZ/GDC 이중층 전해질을 적용하여 500도씨에서 699 mW/cm^2의 성능을 확보하였다.

개발된 금속지지체기반 박막 고체산화물 연료전지 추가적인 요소 분석을 위해 연료극의 조성비를 다양하게 제작하고 분석하였다. 공정의 일관성을 위해 모든 요소를 스퍼터링 공정을 적용하여 제작하였고 연료극의 경우 공동스퍼터링을 통해 NiO-GDC 전극을 제작하였다. 인가하는 파워를 조절하여 다양한 부피비의 전극을 제작하였으며 그에따른 성능을 비교하였다. 최종적으로 약 1:1비율의 부피비의 연료극이 가장 높은 성능을 나타내는 것을 확인하였고 개발된 박막 연료전지의 열 내구성 검증을 위해 열 사이클 실험을 진행하였다. 그 결과 5회의 열사이클에도 성능이 유지되는 것을 확인할 수 있었다.

감사의 글

하나의 목표만을 위해 끝없이 노력했던 5년 반 동안의 박사학위 과정이 드디어 끝을 맺습니다. 혼자서는 이렇게 무사히 학위 과정을 마칠 수 없었기에 저를 응원해 주시고 함께해 주신 모든 분들께 감사의 마음을 전하고자 짧은 글을 쓰고자 합니다.

우선 늦은 나이에 학위과정을 시작하는 저를 제자로 받아주신 차석원 교수님께 무한한 감사를 드립니다. 교수님께서 지도해 주시고 지원해 주신 덕분에 최고의 연구실에서 하고자 하는 연구를 마음껏 할 수 있었습니다. 다양한 연구 경험뿐만 아니라 교수님께서 해주시는 조언을 통해 인생을 살아가는 데 있어 필요한 많은 인사이트를 얻을 수 있었습니다. 다시 한번 감사드립니다.

저는 연구실 생활을 통해 정말 소중한 인연을 많이 만났습니다. 연구실 구성원들 모두에게 배울 점이 있었고 덕분에 저의 가치관이 많이 바뀌었습니다. 대학원 생활을 같이하지는 못했지만 연구실 생활의 방향을 잡아주신 선배님들께 감사드립니다. 연구에 대한 많은 조언과 행동력을 보여주신 장익황 교수님, 학위과정 시작부터 저에게 연구란 무엇인가를 알려주신 박태현 교수님, 장기간의 학위과정에도 나태해 지지 않도록 격려, 지원해 주신 조구영 교수님, 저의 연구와 진로에 관해 많은 조언을 해주신 이윤호 교수님, 목표를 위해 행동하는 법을 알려주신 이희윤 교수님, 모두 감사드립니다.

팀은 다르지만 연구실을 위해 함께했던 하이브리드 팀 인원들에게도 감사를 전합니다. 연구실 생활에 잘 적응할 수 있도록 항상 웃으며 대해주신 종대 형, 기영이 형, 대학원 생활을 즐겁게 할 수 있도록 뭐든지 함께 했던 동네 주민 창범이 형, 본현이 형 감사드립니다. 항상 큰 그림을 그리며 티키타카가 잘 맞는 대학 동기 창희, 언제나 끝까지 함께해 주는 멋진 선배 동환이, 뭐든지 함께하면 든든한 선배 경현이 감사합니다. 뭐든지 척척 해결해 내는 능력자

현준이, 인간미를 보여는 클라이머 광언이, 많이 신경 써주지 못해 항상 미안한 승민이, 감사합니다. 함께해서 행복했습니다.

연구실과 실험실에서 가장 많은 시간을 함께 보냈던 연료전지 팀 팀원들에게도 감사의 말을 전합니다. 연구자로써 멋진 모습을 보여준 첫 방장이자 친구 원종이, 뭐든지 알고 있는 똑똑한 유성이, 연구도 일상도 가장 많은 시간을 함께 보낸 친구 같은 선배 상훈이 상봉이, 감사합니다. 착하고 이제는 든든한 동기 인원이, 항상 선배를 존중해 주는 예의 바른 명석이, 나이 차이는 많이 나지만 연구도 취미도 함께해 준 재원이, 뭐든지 함께해 주는 사회생활 만렙 양재, 변하는 모습을 보여준 유재 감사합니다. 졸업 준비로 많이 챙겨주지 못했지만 궂은일을 싫은 소리 없이 해준 다니엘, 인영, 수혁, 상용, 재원 모두 감사합니다. 뭐든지 함께 공부하고 실험하는 모습을 보면 앞으로의 연구실 모습이 많이 기대됩니다.

마지막으로 저를 항상 지지해 주는 가족들에게도 감사의 말씀을 드립니다. 퇴사와 늦은 나이에 대학원 진학이라는 저의 결정을 믿고 지지해 주신 부모님, 언제나 저를 응원해 주시고 지원해 주신 막내 고모, 어쩌면 저보다 힘든 시기에도 저를 응원해 준 누나 모두 정말 사랑하고 감사드립니다. 그리고 불확실하고 안정되지 않은 저를 항상 같은 자리에서 기다리며 희생해 준 사랑하는 아내 다혜에게 정말 무한한 감사의 말을 남깁니다. 기쁨과 슬픔을 함께해 주고 연구가 잘 안될 때면 잘 하고 있다고 스스로를 믿을 수 있도록 용기를 준 덕분에 학위과정을 무사히 마칠 수 있었습니다. 이제는 새로운 시작을 함께하는 다혜에게 앞으로도 믿음직한 남편이 될 수 있도록 노력하겠습니다. 감사하고 사랑합니다.

서울대학교 재생에너지 변환연구실에서 생활할 수 있었던 건 저에게는 정말 크나큰 행운이었고 저의 인생에 가장 큰 터닝포인트가 될 것입니다. 대학원에 오게 되어 새롭게 알게 된 인연부터 그들과 함께 하며 얻은 경험과 지식은 앞으로 저의 인생을 살아가는데 가장 큰 자양분이 될 것입니다. 비록 많은 것을 남기고 졸업하지는 못하지만 사회에 먼저 나가 연구실 선 후배들에게 도움을

줄 수 있는 사람이 되도록 노력하겠습니다. 앞으로도 좋은 인연이 계속되기를 기대합니다.

정원엽 드림